Towards a Wireless Fluorescence Microscope on A Chip

Rozhan Rabbani
Mekhail Anwar, Ed.
Vladimir Stojanovic, Ed.
Rikky Muller, Ed.
Ali Niknejad, Ed.

Electrical Engineering and Computer Sciences
University of California, Berkeley

Technical Report No. UCB/EECS-2025-31
http://www2.eecs.berkeley.edu/Pubs/TechRpts/2025/EECS-2025-31.html

May 1, 2025

Acknowledgement

H. Najafiaghdam, B. Zhao, M. Ghanbari and E. Papageorgiou contributed to the first sensor. M. Roschelle and I contributed equally to design and test of the second sensor. S. Gweon, R. Kumar and A. Vercruysse were involved in the design and test of the second sensor. M. Roschelle, N. W. Cho and M. Spitzer designed ex vivo experiments. Prof. M. Anwar is the principal investigator of the presented work and Profs V. Stojanovic, R. Muller and A. Niknejad guided the research presented in this thesis.

Towards a Wireless Fluorescence Microscope on A Chip

by

Rozhan Rabbani

A dissertation submitted in partial satisfaction of the

requirements for the degree of

Doctor of Philosophy

in

Engineering - Electrical Engineering and Computer Sciences

in the

Graduate Division

of the

University of California, Berkeley

Committee in charge:

Professor Vladimir Stojanovic, Chair
Professor Mekhail Anwar
Professor Rikky Muller
Professor Ali Niknejad

Spring 2024

Towards a Wireless Fluorescence Microscope on A Chip

Abstract

Towards a Wireless Fluorescence Microscope on A Chip

by

Rozhan Rabbani

Doctor of Philosophy in Engineering - Electrical Engineering and Computer Sciences

University of California, Berkeley

Professor Vladimir Stojanovic, Chair

Real-time access to multicellular information from dynamic biological processes in the body is crucial for understanding disease progression and treatment response. An impactful application is cancer immunotherapy, an effective therapeutic that unleashes the immune system to better identify and attack cancer. While immunotherapy has shown high survival rates in responders, low response rates (<50%) among patients necessitate a deeper understanding of complex resistance mechanisms early in the treatment to improve outcomes. However, current clinical imaging techniques such as MRI, CT and PET lack the molecular contrast, resolution, and chronic usability to enable early recognition of non-responders and adaption to more personalized therapeutic regimens. Moreover, invasive tissue collection methods such as biopsies are impractical on a repeated basis limiting detection to snap-shots of the tumor microenvironment.

Fluorescence microscopy (via injection of fluorescently tagged cell-specific probes) circumvents low sensitivity and long delays of the existing modalities, but is yet to be deployed on a platform compatible with long-term implantation. This thesis presents a miniaturized lensless fluorescence microscope-on-a-chip capable of 1) chip-scale imaging of multiple cell types with an image sensor and an optical frontend for multicolor imaging, 2) in-situ illumination through device-level integration of light sources, and 3) wireless power transfer and communication via ultrasound (US) for chronic implantation at depth.

The first-generation sensor serves as a proof-of-concept for single-color wireless fluorescence imaging incorporating a CMOS chip, a micro laser diode (μLD), a mm-sized piezoceramic and off-chip storage capacitors. The chip consists of a 36×40 array of capacitive trans-impedance amplifier-based pixels, wireless power management and communication via US and a laser driver all controlled by a Finite State Machine. The piezoceramic harvests energy from the acoustic waves at a depth of 2 cm to power up the chip and transfer 11.52 kbits/frame via backscattering. During *Charge-Up*, the off-chip capacitor operates with 905 mW/cm^2 of US power density and stores charge to later supply the instantaneous power of the μLD during *Imaging*. Proof of concept of the imaging front end is shown by imaging distributions of

CD8+ T-cells, an indicator of the immune response to cancer, *ex vivo*, in the lymph nodes of a functional immune system (BL6 mice) against colorectal cancer consistent with the results of a fluorescence microscope. The overall system performance is verified by detecting 140 μm features on a resolution target wirelessly transmitted via US backscattering.

Next, we expand the work to a fully wireless image sensor specifically designed for multicolor fluorescence imaging deep in tissue. The new sensor operates deeper at 5 cm depth in oil, harvesting energy with 221 mW/cm^2 (4x lower than the first sensor) incident US power density (31% of FDA limits) and backscattering data at 13 kbps with a bit error rate $<10^{-6}$. In-situ fluorescence excitation is controlled with a wirelessly programmable on-chip driver. An optical frontend combining a multi-bandpass interference filter and a fiber optic plate provides >60 dB attenuation of the excitation background and enables three-color fluorescence imaging for multi-cell-type detection. The resolution is <125 μm. The system's performance is validated through wireless, dual-color fluorescence imaging of effector and suppressor immune cells in *ex vivo* mouse tumor samples with and without immunotherapy. These results show promise for rapid identification of the underlying control mechanisms in therapeutic response, guiding more effective therapies.

Finally, we apply deep learning models to images obtained with our customized contact image sensors to enable 3D reconstruction and depth estimation from 2D images beyond conventional linear optimization techniques.

To my beautiful sister, Baran.

Contents

List of Figures

List of Tables

Acknowledgments

I would like to thank my advisors Prof. Mekhail Anwar and Prof. Vladimir Stojanovic for their guidance, support and invaluable advice throughout the past six years. I am deeply appreciative of Prof. Mekhail Anwar for the opportunity to work on a project with significant potential for real impact on healthcare. His belief in my abilities to take on this challenge and his support to overcome the obstacles have been instrumental in realizing my dream of contributing to biomedical research while pursuing a career as an engineer. I am thankful for his support during challenging times encouraging me to keep believing in our goal and move forward.

Prof. Vladimir Stojanovic has been a great co-advisor who has generously provided me his technical expertise and career support during these years. I greatly appreciate his very kind encouragements in acknowledging my achievements along the journey.

Prof. Rikky Muller has been a wonderful collaborator generously opening the doors of her research lab and providing invaluable assistance and expertise, which have been instrumental in developing the project and bringing it to its current form. Special thanks to Prof. Ali Niknejad for his mentorship and support as a member of my quals and thesis committee. I have always admired his technical knowledge and kind personality, which have been a source of inspiration throughout my PhD.

In the EECS department, I want like to thank Shirley Salanio for her unconditional assistance during these years. She has gone above and beyond her role as a graduate advisor always sending positive thoughts my way and brightening my day! I also want to thank Candy Corpus-Steudeman for her exceptional administration at BWRC which has turned it into more than just a workplace for us.

I want to give a big shout-out to my amazing project partner and friend, Micah Roschelle, for being such a great source of support during the past four years. Our collaboration has been truly incredible, and I have enjoyed the opportunity to continuously learn from him. I am grateful for having such a trustworthy project partner who has made this journey very enjoyable despite all the challenges we have faced.

To my other dear friends at Anwar lab - Rahul Lall, Averal Kandala, Masoumeh Sabzi, Surin Gweon, Alec Vercruysse, Sevda Mohammadi and Abijeet Mehta - who have been more than just lab mates. Both academically and personally, they have been a constant source of support, friendship and positive energy and I am grateful for all the great memories we have made together.

To my amazing mentors, Efthymios Papageorgiou, Hossein Najafiaghdam, Mohammad Meraj Ghanbari and Kyoungtae Lee who have been my role models. Their willingness to share their knowledge and experiences have been instrumental in shaping my academic journey.

To my beloved family, I am forever thankful to my dear parents Nasrin and Abdollah for their unconditional love and sacrifices making me the person I am today. My wonderful sister, Baran, has been a constant source of inspiration reminding me always to do my best. Being away from them has been one of the greatest challenges and I miss them more than words can say.

To my amazing partner, Behrooz Ghorbani for staying with me during the toughest times and always giving me his support even without me asking for it. I am truly grateful for your presence in my life.

This journey would not have been possible without my incredible friends - Mahsa Sadeghi, Biqi Rebekah Zhao, Alisha Menon, Soogand Alavi, Zohreh Azizi, Sorour Tarighi, Mahsa Amanabi, Ekin Karasan, Shreya Ramachandran, and Amin Torabi. I have always looked up to them in every aspect of my life. I feel truly blessed to have friends like them. We have shared so many wonderful memories and I am looking forward to creating many more in the future.

Chapter 1

Introduction

Continuous access to *in vivo* information through implantable biomedical sensors can provide insights for diagnosis and personalized treatment guidance based on real-time feedback from the patient's own tissue. Wireless, miniaturized, implantable sensors can monitor intricate biological processes unfolding in the body in real-time [1, 2, 3, 4, 5]. Typically accessible only through highly invasive techniques, this data is crucial for advancing personalized medicine, tailoring treatments to individual patient responses to address the wide heterogeneity in therapeutic outcomes.

1.1 Real-time Monitoring in Cancer Immunotherapy

Monitoring tumor response is an impactful application in cancer immunotherapy, a treatment that unlocks the patient's own immune system to fight cancer. For instance, immune checkpoint inhibitors (ICIs), a type of immunotherapy, have been shown to nearly double patient survival rates in melanoma [6] and metastatic lung cancer [7] with a lower incidence of adverse effects compared to conventional treatments like chemotherapy [8]. ICIs are now used across cancer types and are estimated to be available to more than 40% of US cancer patients [9]. However, immunotherapy faces a significant challenge: across most cancer types, less than 30% of patients respond to therapy [10, 11]. For the majority of patients who do not respond, time spent on ineffective therapies not only reduces the likelihood of an eventual cure, but also exposes them to unnecessary toxicity with high-grade adverse events rates often exceeding 10% [10] and financial burdens of more than $150,000 per year [12, 13]. Rapid assessments of therapeutic response that also provide insight into the underlying mechanisms of resistance can help clinicians quickly identify non-responders and pivot to more effective second-line therapies. Therefore, an imaging system for cancer immunotherapy must be capable of imaging tumor state changes at time intervals frequent enough to capture cell cluster motion ($\sim$minutes to hours), over long periods (days to months). However, such an assessment must capture the complex and dynamic interplay between various effector and suppressor immune cells and cancer that determines response [10]. However, current clinical

imaging falls short of this goal. Currently, these factors are only visible when looking at the tissue under a microscope, obtained via a biopsy. However, repeated biopsies, often of sites deep within the patient, are impractical due to morbidity, cost, and logistics.

1.2 Clinical Imaging vs. Optical Imaging

In clinical practice, the state of the art for monitoring immunotherapy response is to use the following imaging technologies: computed tomography (CT), magnetic resonance imaging (MRI), positron emission tomography (PET), and multimodal techniques (CT/PET, PET/MRI, etc.) [14, 15]. Anatomical imaging modalities such as CT and MRI capture changes in tumor size, which take months to manifest and do not reliably correlate with response [16]. These limitations are apparent in standard response criteria. For example, iRECIST defines a partial response as at least a 30% reduction in tumor dimensions with a minimum size of 1 cm and recommends confirmation of disease progression at long 4-8 week intervals [17, 18]. Given a cell is $\sim$10 μm, a 30% change equates to a minimum change of 300 million cells, taking months to manifest. Alternatively, PET can image the underlying biology with molecular contrast [19] but is fundamentally limited to imaging a single cell type or biomarker [20] at millimeter-scale resolution [21]. As the immune response depends on interactions between a variety of immune cells, it cannot be reliably predicted by a single biomarker [22, 23]. Moreover, this millimeter-scale resolution averages out the spatial distributions of different cell populations within the tumor shown to be increasingly important in understanding therapeutic resistance [24, 25]. Additionally, the need to utilize hospital-based imagers preclude serial imaging due to the logistics and cost associated with repeated imaging spaced only by hours or days. Without continuous monitoring, conventional techniques are restricted to snap-shots unable to capture the dynamics of the key biological phenomena. Therefore, an additional method in conjunction with clinical imaging of the tumor response is needed.

Optical microscopy, on the other hand, enables high-resolution imaging providing key information regarding disease progression and treatment efficacy [26]. Fluorescence microscopy is an optical imaging method that provides multicell-level resolution across multiple biomarkers, essential to visualizing a more complete picture of the immune response. In fluorescence microscopy, targeted cells are labeled with fluorescent dyes, or fluorophores, which absorb light near a specific wavelength and emit light at slightly longer wavelengths [27]. Multiple cell types can be imaged simultaneously by labeling each with a different color fluorophore. However, *in vivo* optical imaging is constrained by scattering in tissue which fundamentally limits the penetration depth of light in the body to a few millimeters, even at NIR wavelengths where tissue absorption is minimal and scattering is reduced [28]. For example, intravital microscopy (IVM) is an optical imaging modality that can leverage fluorescence to visualize *in vivo* processes using a surgically implanted window [29, 30]. Despite the high resolution of IVM, visualization is restricted to depths less than a few millimeters [31, 32]. This imaging approach is limited to tumors or organs at the tissue surface, unable to be maintained over

long periods of time, and is fundamentally incompatible with patient imaging. Therefore, implantable fluorescence imagers with integrated light sources providing in-tissue illumination are needed for chronic imaging at depth.

1.3 Prior Art Chip-Scale Image Sensors

Fluorescence imagers can be miniaturized to the scale of a single chip by eliminating bulky lenses through contact imaging [33, 34, 35, 36, 37, 38, 39]. To this end, prior work has demonstrated on-chip or in-package integration of focusing optics [33, 40] as well as fluorescence filters [34, 35, 36, 37, 41] and light sources [34, 37]. However, all of these systems are wired, precluding long-term implantation without risk of infection. Both wireless power transfer and communication are necessary for chronic use of these devices.

A list of the state-of-the-art chip-scale image sensors is included in Fig. 1.1. The fluoresce image sensor presented in [34] integrates in-package light sources for *in vivo* neural recording and optogenetic stimulation. However, its single color imaging capability limits detection to a single cell type which is not sufficient for monitoring the complex and multiplexed immune system. Despite its flexible design, the wired configuration is not suitable for untethered applications.

The FDA-approved capsule in [35] is designed for *in vivo* bio-molecular sensing. The system incorporates a CMOS fluorescence sensor with an integrated filter, an ultraviolet LED and an optical waveguide. The sensor utilizes wireless radio-frequency (RF) bi-directional communication and offloads computations to an external base station. However, the system's power supply relies on a centimeter-scale battery, which is inadequate for implantable applications. Additionally, without wireless charging capability, long-term implantation is not feasible.

The fluorescence sensor developed in [36] integrates multi-color filters in the CMOS chip for bio-molecular sensing of two fluorescent proteins to distinguish two biochemical signals. Although it captures the dynamics of E. coli bacterial cell growth, its resolution is inadequate for tissue imaging, and it has yet to be deployed in a wireless embodiment for deep tissue monitoring.

The needle-type image sensor in [37] stacks composite multilayer filters for high-spatial-resolution fluorescence imaging and incorporates a fiber-coupled laser for fluorescence excitation. Although imaging of the green fluorescent proteins (GFP) expressed in mouse brain slices is demonstrated, this imager lacks wireless interface and in-package light sources for untethered monitoring in the body.

A wireless thermoacoustic imager has been introduced in [42]. Imaging is performed with a capacitive micromachined ultrasound transducer (CMUT) array. The sensor uses two piezoceramic transducers for wireless power and data transfer via ultrasound (US). However, thermoacoustic imaging does not provide the sensitivity and specificity needed to track the immune response. Fiber optic probes have shown *in vivo* imaging but their utility for continuous monitoring is limited by the invasiveness of the process [43].

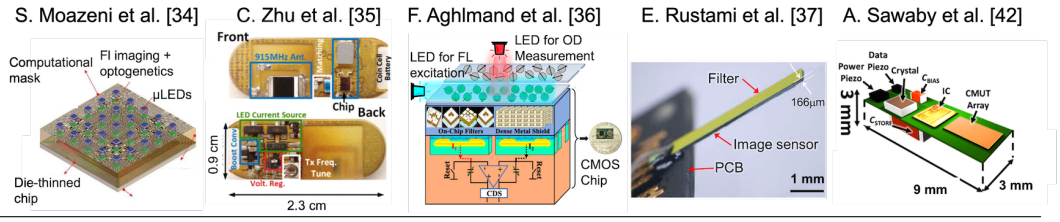

Application	*In vivo* neural imaging/ stimulation	*In vivo* bio-molecular sensing	Bio-molecular sensing	*In vivo* neural imaging	US imaging
Imaging Method	Fluorescence	Fluorescence	Fluorescence	Fluorescence	Thermoacoustic
Power Delivery	Wired	Battery	Wired	Wired	Wireless (US)
Communication	Wired	Wireless (RF)	Wired	Wired	Wireless (US)

Figure 1.1: Prior art chip-scale image sensors adapted from [34, 35, 36, 37, 42].

1.4 Proposed Solution

To address the challenge of the absence of a wireless implantable image sensor with multicolor detection capabilities for monitoring the multiplexed biological processes such as the immune response to cancer immunotherapy, we propose the systems depicted in Fig. 1.2. To realize this envisioned system, the thesis demonstrates a two-step process by presenting the design and implementation of two sensors, ultimately achieving the following key capabilities:

1. **Wireless power and data transfer via US** to supply the sensor and transmit data using a single US transceiver.

2. **Chip-scale fluorescence imaging** to detect state changes in cell foci of 100s of cells enabling the capture of multiple cell types involved in the immune response to cancer.

3. **Supply of high instantaneous power to micro laser diodes (μLDs)** with limited available power harvested from US to provide in-situ illumination for the image sensor.

Among wireless power transfer modalities such as near-field inductive coupling, RF, and optical, US offers low attenuation in tissue (0.5-1 dB/MHz/cm [44]), a high Food and Drug Administration (FDA) regulatory limit for power density (720 mW/cm^2), and a short wavelength (∼3-4 mm in the PZT material at 1 MHz) enabling power transfer to millimeter-scale implants at centimeter-scale depths [45, 46].

In this thesis, first, we present a single color fluorescence image sensor. A single piezoceramic is controlled by the sensor for wireless power transfer and data communication up to a depth of 2 cm. To eliminate bulky optical lenses, a microfabricated angle-selective collimator is utilized to restrict the angle of incident light resulting in sharper images with higher resolution building on our previous work [33, 47]. The device powers up using wireless energy from the US link, and following commands encoded in the US transmissions proceeds to illumination using a μLD while simultaneously capturing an image from fluorescently

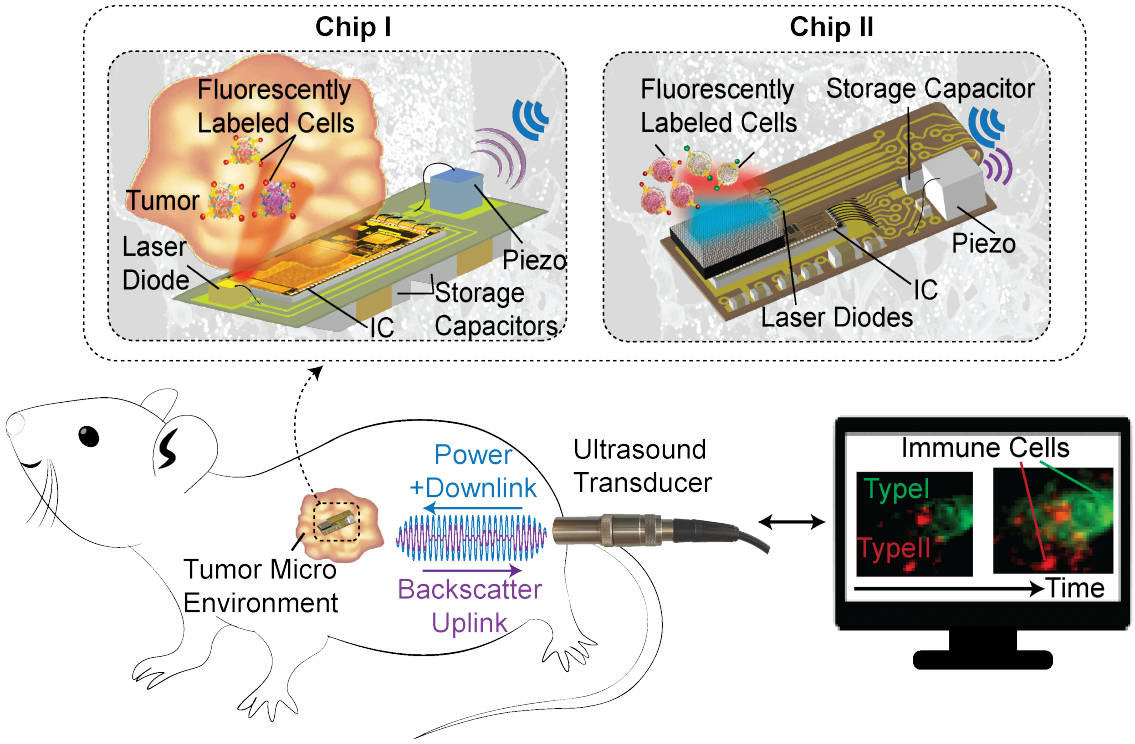

Figure 1.2: Concept of a fully wireless, implantable imager for real-time monitoring of immune response.

labeled targets. Next, it serially converts each pixel to a digital value and transmits data back to an external transducer via US backscattering.

While the first sensor shows significant progress toward a wireless fluorescence imaging system [48, 49, 50], this system has several limitations. It incorporates a large ∼1 mF off-chip capacitor for energy storage. It only operates at 2 cm depth, constraining its application to superficial tumors while exceeding FDA US safety limits by 26% due to high acoustic power requirements. Moreover, the sensor only images a single fluorescent channel, lacking both a wirelessly programmable laser driver to take images with multiple excitation lasers as well as a multi-bandpass optical filter necessary for multicolor fluorescence imaging. Additionally, due to in-pixel leakage during readout, the sensitivity of the imager when operating wirelessly is limited to high concentrations of fluorophores, rendering it insufficient for imaging biologically relevant samples.

Theses limitations motivated the design of the second generation of the sensor, a fully wireless, miniaturized fluorescence image sensor capable of three-color fluorescence imaging of fluorescent beads, enabling real-time, chronic monitoring of cellular interactions at depth. Wired connections and batteries are eliminated by power harvesting and bi-directional communication through ultrasound (US). The new system achieves significant improvements

in performance, size, and programmability, specifically designed for multicolor imaging. The differences between the two sensors are discussed in detail. The new system shows fully wireless operation at 5 cm depth in oil, requiring 221 mW/cm^2 US power flux density (31% of FDA limits) for power harvesting and transmitting data with a bit error rate (BER) less than 10^{-6} through US backscatter. It powers three different-wavelength laser diodes programmed through US downlink and incorporates a multi-bandpass optical frontend building on the design in [50] to enable three-color fluorescence imaging to detect multiple cell types.

1.5 Thesis Orientation

This thesis is organized into eight chapters. Chapter 2 outlines the design specifications of a wireless chip-scale fluorescence image sensor and introduces the essential components needed to develop the device. Chapter 3 discusses the design of the first generation of the sensor, "A single color wireless fluorescence image sensor", and chapter 4 presents the performance expanding on the work in [50]. Following the challenges of the first generation of the sensor described in chapter 4, in chapter 5, we introduce the second generation, "A multi color wireless fluorescence image sensor" and showcase the performance in chapter 6 expanding on the work in [51]. Chapter 7 introduces an deep learning based image processing technique to obtain more information from the images acquired with the sensor in the previous chapters. The conclusion and future directions are provided in chapter 8.

1.6 Contributions

The work presented in this thesis is adapted from the following articles:

1. **R. Rabbani***, M. Roschelle*, S. Gweon, R. Kumar, A. Vercruysse, N. W. Cho, M. H. Spitzer, A. M. Niknejad, V. M. Stojanovic, M. Anwar, "17.3 A Fully Wireless, Miniaturized, Multicolor Fluorescence Image Sensor Implant for Real-Time Monitoring in Cancer Therapy," *2024 IEEE International Solid-State Circuits Conference (ISSCC)*, San Francisco, CA, USA, 2024, pp. 318-320. (* Equally credited authors)

2. **R. Rabbani**, H. Najafiaghdam, M. Roschelle, E. P. Papageorgiou, B. R. Zhao, M. M. Ghanbari, R. Muller, V. Stojanovic, M. Anwar, "Towards A Wireless Image Sensor for Real-Time Fluorescence Microscopy in Cancer Therapy," in *IEEE Transactions on Biomedical Circuits and Systems (2024)*.

3. H. Najafiaghdam, **R. Rabbani**, A. Gharia, E. P. Papageorgiou, M. Anwar, "3D Reconstruction of cellular images from microfabricated imagers using fully-adaptive deep neural networks". *Scientific Reports* 12, 7229 (2022).

4. **R. Rabbani**, H. Najafiaghdam, B. R. Zhao, M. Zeng, V. M. Stojanovic, R. Muller, M. Anwar "A 36×40 Wireless Fluorescence Image Sensor for Real-Time Microscopy in

Cancer Therapy," *2022 IEEE Custom Integrated Circuits Conference (CICC)*, Newport Beach, CA, USA, 2022, pp.

5. **R. Rabbani**, H. Najafiaghdam, M. M. Ghanbari, E. P. Papageorgiou, B. R. Zhao, M. Roschelle, V. M. Stojanovic, R. Muller, M. Anwar, "Towards an Implantable Fluorescence Image Sensor for Real-Time Monitoring of Immune Response in Cancer Therapy," *2021 43rd Annual International Conference of the IEEE Engineering in Medicine & Biology Society (EMBC)*, Mexico, 2021, pp. 7399-7403.

Personal Contribution: I have been involved in developing and brainstorming the projects, design, measurements and debug of the both sensors in chapters 2-6. I have contributed to the synthesis of the dataset and design and test of the ResNet+CNN model in chapter 7.

Acknowledgments: H. Najafiaghdam, B. R. Zhao, M. M. Ghanbari and E. P. Papageorgiou contributed to the design and testing of the first generation of the sensor. M. Roschelle contributed to testing the first generation. M. Roschelle and I have contributed equally to the design, measurement and figure generation of the second generation. S. Gweon, R. Kumar and A. Vercruysse have been involved in the design and testing process of the second generation. M. Roschelle contributed to the *ex vivo* experiments conducted in collaboration with N. W. Cho, Prof. M. H. Spitzer. I truly appreciate technical expertise, support and guidance of Prof. M. Anwar, Prof. V. Stojanovic, Prof. R. Muller and Prof. A. Niknejad for all the research presented in this thesis.

Chapter 2

Sensor for Wireless Fluorescence Imaging

To design a wireless system for fluorescence imaging, as illustrated in Fig. 1.2, system-level integration of the IC and the optical source (as light cannot penetrate from an external source deep into the tissue) is essential. Fig. 2.1 shows a diagram and mechanical assembly of the full system on a flex PCB with all external components. The miniaturized wireless system consists of 1) μLDs for in-situ illumination, 2) an optical frontend comprising of angle selective structures, on-chip (angle selective gratings) or off-chip (fiber optic plate), as resolving optics and a filter for lensless fluorescence imaging, 3) a 1.5×1.5×1.5 mm^3 piezoceramic (Lead Zirconate Titanate, PZT) as the US transceiver; 4) off-chip capacitors for energy storage; and 5) an ASIC to integrate the imaging, wireless power and data transfer and optical source control functionality.

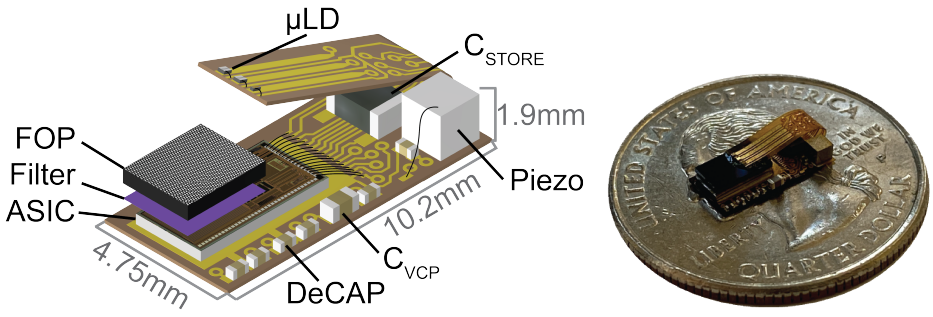

Figure 2.1: (a) To-scale diagram of the full system. (b) Mechanical assembly.

Quantifying the fluorescence signal from cell foci in immunotherapy is the key to determining the specifications of the device, the size of the storage capacitor and the requisite optical power from the light source. This section describes the approach to quantify the fluorescence

signal from a cluster of cells, outlines the requirements for the external components of the system and derives design specifications for the ASIC.

2.1 Fluorescence Imaging

Fig. 2.2 illustrates the principle of fluorescence imaging. The fluorophores are first conjugated to a probe (Fig. 2.2(a)), such as an antibody, targeted toward a cell type of interest [27]. For *in vivo* imaging, the conjugated probe can be administered systemically through intravenous injection, binding only to targeted cells. The fluorophore determines the wavelength for imaging, and the antibody specificity ensures labeling the target cell type. Numerous organic fluorophores have shown low toxicity at doses relevant for imaging [52] and a number of fluorescent probes are FDA-approved or in clinical trials, including some using Fluorescein (FAM) and Cyanine5 (Cy5) and Cy5.5, [53], the fluorophores in our *ex vivo* studies. The conjugated probes have a half-life of days-weeks before the injections need to be repeated [54]. A list of probes for fluorescence imaging that are either FDA-approved for use in humans or are undergoing clinical translation is included in [53]. After labeling the cells, the fluorophores are excited near their absorption peak (λ_{EX}) and emit light at a slightly longer wavelength with a peak at λ_{EM} (Fig. 2.2(b-c)). For organic fluorophores typically used in *in vivo* studies, the difference between the absorption and emission peaks, or Stokes shift, is 10-30 nm (18 nm for Cy5 and 26 nm for FAM). Moreover, due to the small absorption cross-section of the fluorophores relative to the illuminated field of view (FoV), the excitation light is often 4 to 6 orders of magnitude stronger than the emission light.

Thus, in order to detect the weak fluorescence signal, an optical filter with an optical density (OD) ≥ 6 is required to attenuate out-of-band excitation light that would otherwise saturate the sensor. Avoiding a filter altogether through time-gated imaging [34, 55, 56]–where excitation and imaging are separated in the time domain–leads to inadequate excitation rejection and low signal intensities with typical organic fluorophores, which have fluorescence lifetimes less than 10 ns [57]. Moreover, background subtraction in the electrical domain [36] adds additional noise to the image and is challenging *in vivo* as the excitation background is dependent on tissue scattering.

For multicolor imaging, a variety of organic fluorophores are available with absorption and emission wavelengths spanning the visible and NIR spectrum [58]. Their narrow absorption and emission spectra allow for multiplexed imaging using a monochrome sensor, by taking a separate image at each excitation wavelength. Therefore, multicolor fluorescence imaging requires multiple excitation sources, and a multi-bandpass filter to block all excitation wavelengths while passing fluorescence emissions.

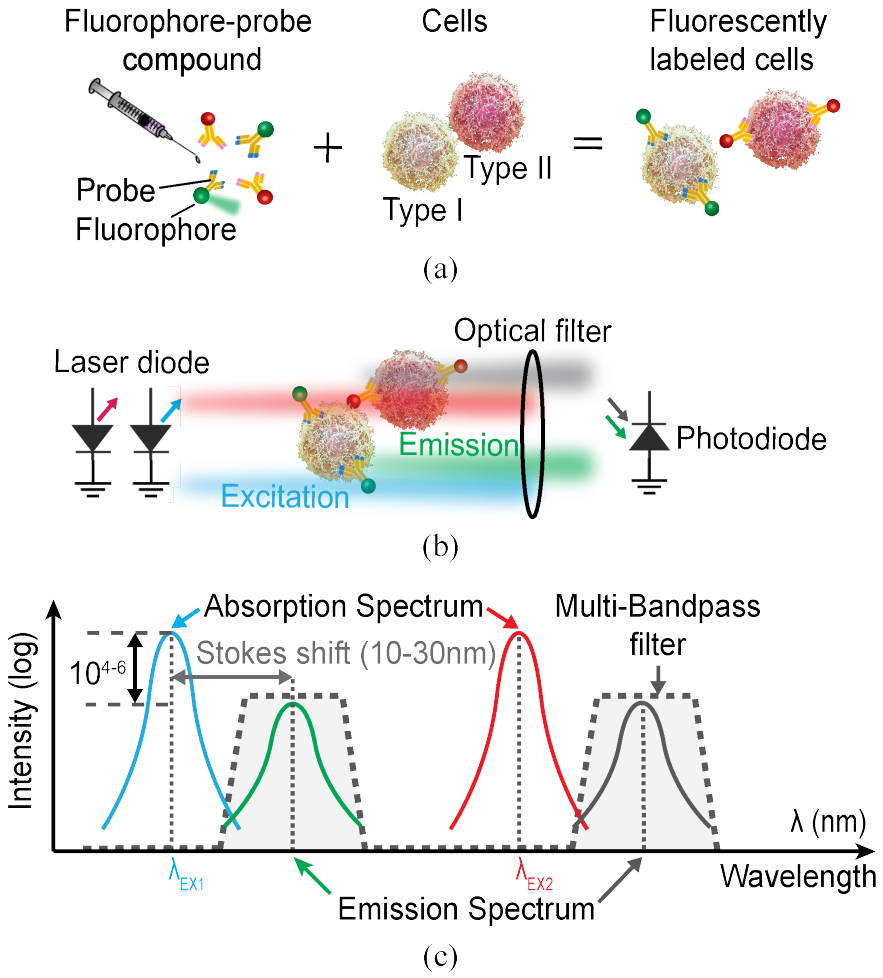

Figure 2.2: Fluorescence imaging. (a) Each cell type is labeled with a different color fluorescent probe. (b-c) Fluorophores are excited near the absorption peak and emit light at a slightly long wavelength. For multicolor imaging, a multi-bandpass filter passes emissions while blocking excitation.

2.2 Light Sources

In addition to the emitted photons, the scattered excitation light from the background contributes to the photodiode signal. Given the high intensity of excitation compared to emission, even small tail emissions of the LED at higher wavelengths will obscure the signal. This can be addressed by covering the LED with an excitation filter or use of a laser diode. For simplicity, we chose a laser diode.

In order to achieve deeper penetration of the excitation and lower tissue autofluorescence [59, 60], for the first generation of the sensor, a μLD with a peak wavelength of 635 nm is chosen over lower wavelengths. The measured power-current-voltage (PIV) characterization

of the edge-emitting μLD (250x300x100 μm^3, CHIP-635-P5, Roithner LaserTechnik GmbH) using a power meter (PM100D, Thorlabs) is shown in Fig. 2.3. The nominal forward voltage and current of 2.1 V and 37 mA, respectively, result in a total measured optical power of 3.4 mW and an electrical to optical efficiency of 4.4%, necessitating significant power delivery to the sensor for fluorescence imaging. Details of supplying the μLD while imaging the samples are included later in the chapter.

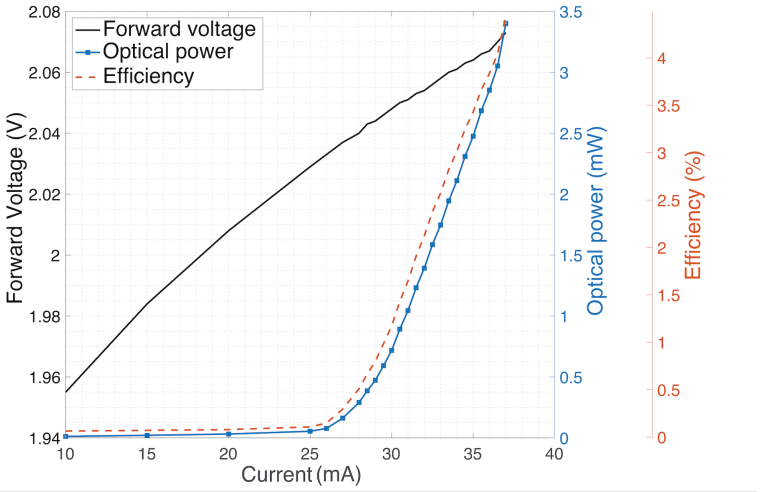

Figure 2.3: PIV characteristic of the 635nm μLD used in the first generation of the sensor.

For the second generation of the ASIC, we use μLDs with wavelengths of 650 nm (250×300×100 μm^3, CHIP-650-P5, Roithner LaserTechnik GmbH) and 455 nm (120×300×90 μm^3, LS0512HBE1, Light Avenue). A third 785 nm laser diode (L785P5, ThorLabs) in a TO-can package is used for proof-of-principle three-color fluorescence imaging and will be replaced by μLDs in the future. Laser diodes are chosen instead of LEDs because LEDs have broader spectral bandwidths, which can overlap with fluorescence emissions. These out-of-band emissions necessitate additional excitation filters on the LEDs that complicate sensor design and waste optical power output [61]. Fig. 2.4(a) shows measured PIV curves for all three lasers with their calculated wall plug efficiencies ($P_{Optical}/P_{Electrical}$) in Fig. 2.4(b). The lasers have different forward voltages: ~2 V for the 650 nm and 785 nm lasers and ~4.5 V for the 455 nm laser. Because of their several ~mA threshold currents, the lasers operate most efficiently near their maximum current ratings. These characteristics motivate the design of a laser driver with programmable current that is tolerant of a wide range of forward voltages.

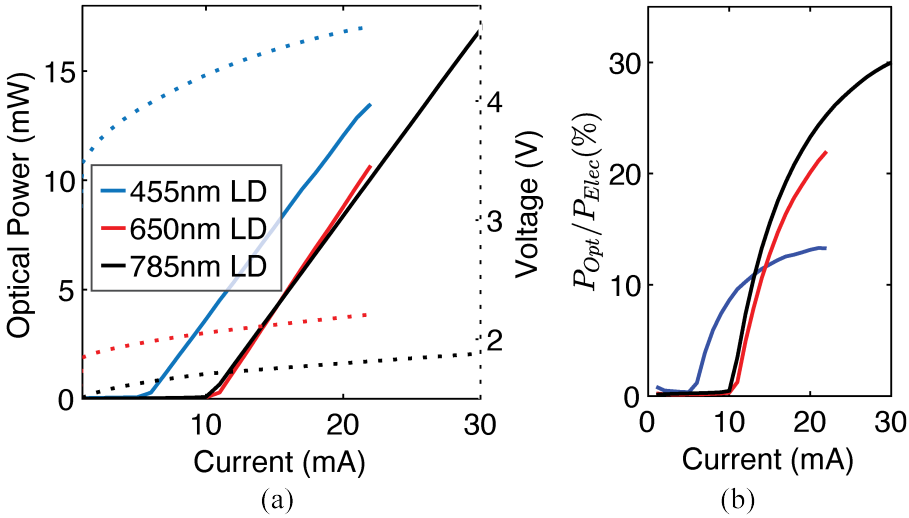

Figure 2.4: Measured laser diode (a) PIV curves and (b) wall plug efficiencies of μLD used in the second generation of the sensor.

2.3 Optical Frontend Design

The optical frontend design expands on our prior work [47] and consists of a multi-bandpass interference filter and a low-numerical-aperture fiber optic plate (FOP). Interference filters offer more-ideal filter characteristics than absorption filters [41] or CMOS metal filters [36, 35, 62], which do not allow for optimal excitation and imaging of organic fluorophores due to their gradual cutoff transitions, weak out-of-band attenuation, and significant passband losses. Hybrid filters combining interference and absorption filters [34, 37, 63] retain the poor passband characteristics of absorption filters. Another major advantage of interference filters is their ability to support multiple passbands across the visible and NIR spectra for multicolor imaging.

However, interference filters are sensitive to angle of incidence (AOI) [64]. At increasing AOIs, the filter passbands shift towards shorter wavelengths, eventually transmitting the excitation light. This property is problematic for lensless imaging where the AOI is not precisely controlled and the excitation light is often angled between the sensor and the tissue above it. To mitigate this effect, the FOP acts as an angle filter, blocking off-axis excitation light that would otherwise pass through the filter. The FOP also improves resolution by eliminating divergent fluorescent emissions that contribute to blur, albeit at the cost of reducing the overall collected signal.

Fig. 2.5(a) shows the normal incidence (AOI=0°) transmittance spectra of the filter (ZET488/647/780+800lpm, Chroma Technologies Corp) which has three passbands with greater than 93% average transmittance. The first two bands pass the emissions of FAM and Cy5, the fluorophores used in our *ex vivo* imaging studies. The 800 nm band, provides another fluorescence channel in the NIR-I window (700–900 nm), a preferred region for *in*

vivo imaging where tissue scattering, absorption, and autofluorescence are minimal compared to the visible spectrum (400–700 nm) [65, 66]. At normal incidence, the filter provides more than 6 OD attenuation at both 450 nm and 650 nm as well as more than 5 OD attenuation at 785 nm, which are the wavelengths of the lasers used in the second generation of the sensor.

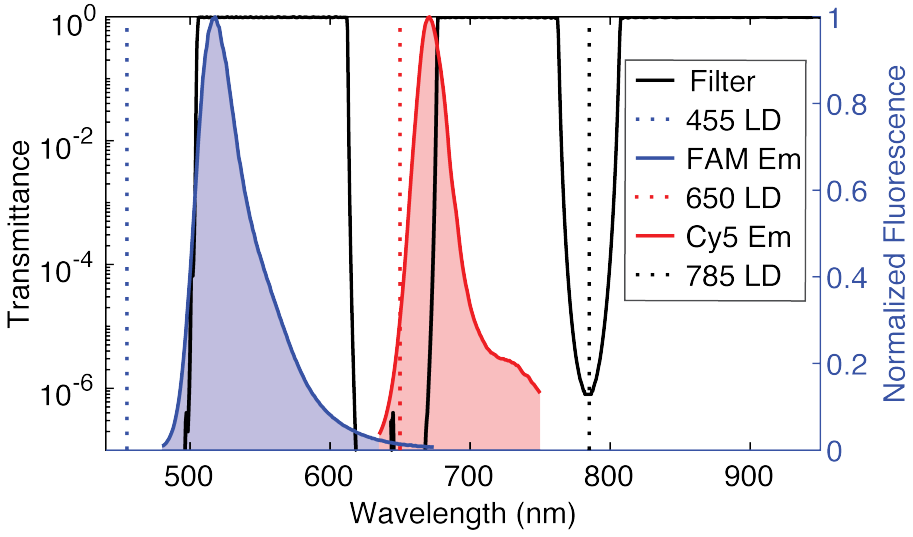

(a)

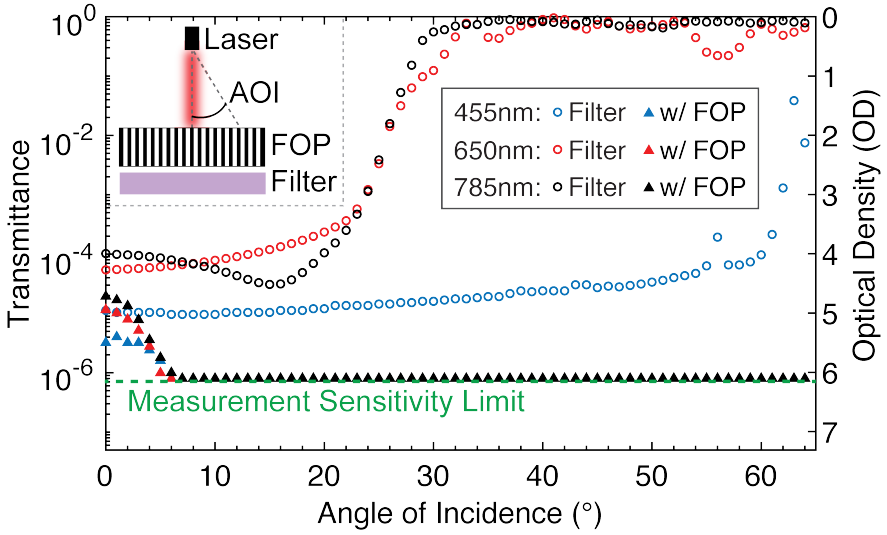

(b)

Figure 2.5: (a) Normal incidence transmittance spectra of the multi-bandpass interference filter. (b) Angular transmittance of the filter with and without the FOP measured at the excitation laser wavelengths.

The 500 μm-thick FOP (LNP121011, Shenzhen Laser, LTD) consists of a matrix of 10 μm optical fibers embedded in black, highly absorptive glass. It has a normal incidence

transmittance of 35% and a full-width at half maximum (FWHM) of 10∘ at 455 nm, which both reduce at longer wavelengths. Beyond an AOI of 35° the FOP provides more than 6 OD attenuation of all three lasers.

Fig. 2.5(b) shows the transmittance through the filter with and without the FOP across different AOIs measured at the excitation wavelengths using collimated, fiber-coupled lasers. The filter attenuation at AOI=0° is different from that in Fig. 2.5(a) due to out-of-band emissions from the lasers. While the filter blocks the excitation lasers near 0°, the laser transmittance rapidly increases beyond AOIs of 20° for 650 nm and 785 nm and 60° for 455 nm. However, with the FOP, the optical frontend provides more than 6 OD of attenuation of all excitation lasers at AOIs greater than 5°. The maximum measured attenuation is limited by the sensitivity of the power meter (PM100D with S120C Photodiode, Thorlabs) used for this measurement.

For fabrication, the interference filter is directly deposited on the FOP, resulting in a total thickness of approximately 510 μm. The optical frontend is fixed to the chip using optically transparent epoxy (SYLGARD 184, Dow Chemicals). The filter is placed in between the chip and the FOP to ensure that it blocks any excitation light scattered through the FOP [47].

2.4 Ultrasound Link

We use a 1.5×1.5×1.5 mm^3 piezoceramic (lead zirconate titanate) as the US transceiver for wireless power transfer and bi-directional communication. The thickness of the piezo is directly proportional to the harvested voltage and inversely proportional to the operation frequency [45]. Therefore, we chose a thickness of 1.5 mm to balance minimizing the overall size of the piezo with the need for harvesting a high enough voltage (>5 V DC) to drive the lasers while operating at a lower frequency with less tissue attenuation as tissue attenuation increases with higher frequencies of operation. An aspect ratio of one is selected as a compromise between volumetric efficiency and backscattering amplitude, as outlined in [67].

Fig. 2.6 shows the impedance and harvested open circuit voltage of the piezoceramic across frequency inside canola oil at a depth of 2 cm for the first generation of the sensor. Canola oil has 0.075 dB/cm acoustic attenuation at ∼1 MHz and 1.34 MRayl acoustic impedance [68] similar to the impedance (1.4–1.67 MRayl) of tissue [44]. The piezo is mounted on a flexible PCB for testing. The frequency dependency of the normalized harvested voltage is shown for the piezoceramic both without loading and loaded with the equivalent model of the chip (refer to chapter4 for the setup). To maximize the harvested voltage according to the resonance spectrum of the piezoceramic and the US transducer, the frequency of operation is tuned in between the series and parallel resonance frequencies of the piezoceramic at 960 kHz.

For the second generation of the device, the piezo is mounted on a similar flex PCB (Fig. 2.7(a)). On the backside of the piezo, an air gap is created by covering a through-hole via with a 3D-printed lid. The air gap reduces the acoustic impedance of the backside medium

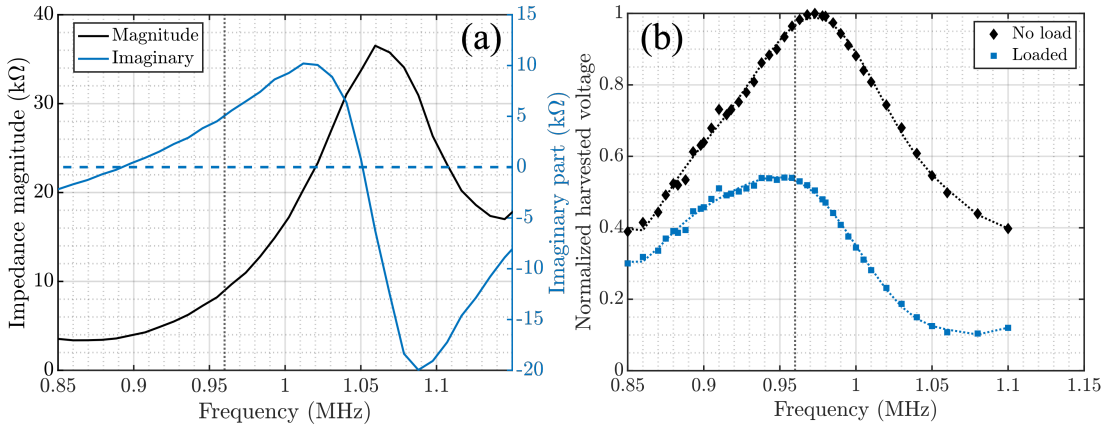

Figure 2.6: Characterization of the piezoceramic used in the first generation of the sensor: Frequency spectrum of (a) magnitude and imaginary part of the impedance and (b) normalized harvested voltage of the piezoceramic with no load vs. being loaded with the equivalent of the chip's input impedance.

from 1.34 MRayl in canola oil to ∼0 MRayl in air, decreasing the electrical impedance of the piezo to improve the power transfer efficiency [69].

Fig. 2.7(b) shows the impedance spectrum of the piezo measured within canola oil. The series and parallel resonance frequencies of the piezo occur at, f_S=894 kHz and f_P=960 kHz, respectively. Fig. 2.7(c) shows the normalized harvested voltage across frequency when the piezo is unloaded and when it is loaded with the chip (refer to chapter 6 for the setup). While operating near f_S minimizes the impedance, the open circuit voltage is maximized near f_P. Therefore, the maximum harvested voltage with the chip occurs between f_S and f_P at 920 kHz.

2.5 Fluorescence Signal Quantification

To derive the required harvested energy per image for sizing the storage capacitor, we estimate the signal detected by a pixel from Cy5-labeled CD8+ T-cells, a type of immune cell imaged in our *ex vivo* studies. The total emitted optical power, P_{CELLS}, from a total of N_{CELLS} fluorescently labeled cells as a function of the input excitation flux is given by

$$P_{CELLS} = N_{CELLS}\, N_{FL}\, \sigma\, QY\, I_{IN}$$

N_{FL} is the number of fluorophores bound to each cell. Typically, between 0.5–2.1×10^6 CD8+ antibodies bind to a single CD8+ T-cell [70] with each antibody containing 2–8 fluorophores [71]. σ and QY are the absorption cross-section and quantum yield of the fluorophore, respectively (9.55×10^{-16} cm^2 and 20% for Cy5 [72]). σ is a measure of the ability of the fluorophore to absorb photons and QY is the ratio of the number of photons emitted

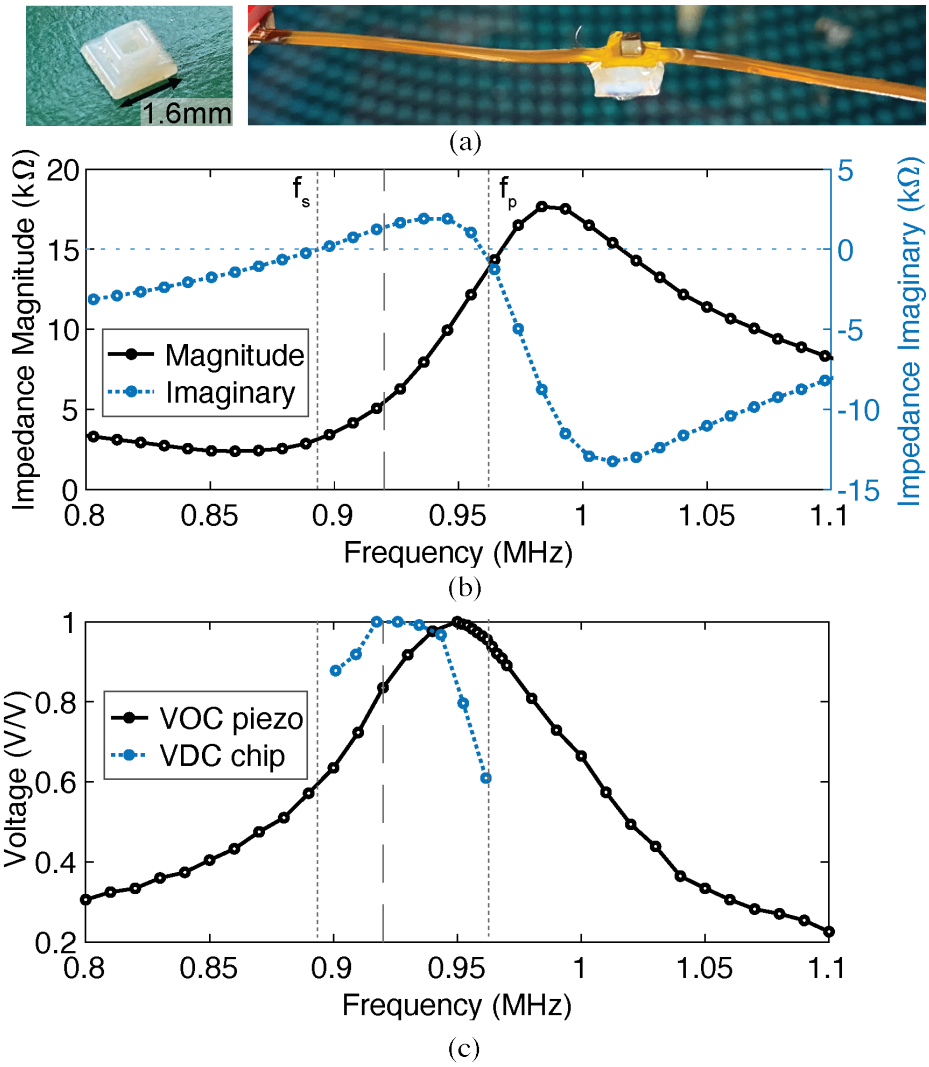

Figure 2.7: Piezoceramic used in the second generation of the sensor. (a) Piezo assembly with the air gap. (b) Measured electrical impedance of the piezo across frequency. (c) Measured harvested voltage across frequency with the piezo in open circuit condition (V_{OC}) and loaded by the chip.

to the number of photon absorbed. Assuming that the 650 nm μLD uniformly illuminates the FoV of our sensor (2×2.2 mm^2) and outputs 10 mW of optical power at I_{LD}=20 mA bias (see Fig. 2.4), the optical power density, I_{IN}, is approximately 223 mW/cm^2. Therefore, the estimated total fluorescence signal from 100 cells is 20 nW. This signal can be converted to the expected photodiode current, I_{PD}, according to

$$I_{PD} \;=\; P_{CELLS}\,\frac{A_{pixel}}{4\pi z_{DIST}^2}\,(1-L_{FOP})\,R$$

This equation accounts for both the spreading loss over the z_{DIST}≈500 μm distance to the pixel with area, A_{pixel} (44×44 μm^2 in our design) and the insertion loss of the FOP, L_{FOP} (∼75% at 650 nm). Given that the pixel has a responsivity, R, of 0.21 A/W at 650 nm, we expect I_{PD} on the order of 6.3 fA.

2.6 System Design Considerations

A simplified diagram of the pixel during imaging is shown in Fig. 2.8. In the capacitive trans-impedance amplifier (CTIA)-based pixel architecture reused from [33] the photocurrent is sensed by integrating it on a capacitor, C_{INT}=11 fF, during the exposure time, T_{EXP}, resulting in a detected signal of

$$V_{sig} \;=\; \frac{I_{PD}\,T_{EXP}}{C_{INT}}$$

Sensing the fluorescence signal relies on V_{sig} exceeding the noise floor, characterized by the signal-to-noise ratio (SNR). SNR is defined as:

$$SNR = \frac{signal}{noise} = \frac{V_{sig}}{\sqrt{\overline{v_{shot}^2}+\overline{v_n^2}}} = \frac{V_{sig}}{\sqrt{\frac{2q_e I_D T_{EXP}}{C_{INT}^2}+\overline{v_n^2}}}$$

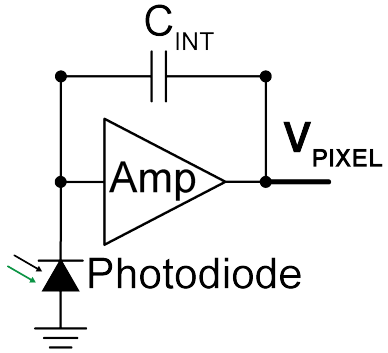

Figure 2.8: Photocurrent integration in a simplified pixel diagram during the exposure time.

The noise has two components: shot noise, $\overline{v_{shot}^2}$, from the photocurrent and dark current, $I_D = I_{PD} + I_{dark}$ and readout noise, $\overline{v_n^2}$. Readout noise refers to the overall noise contribution

of the in-pixel circuitry. For a CTIA-based pixel, it consists of the thermal and flicker noise of the transistors in the pixel amplifier, and the thermal noise of the sample and hold and reset switches. Fixed pattern noise from dark current and pixel variation can be eliminated by subtraction of the dark imager or calibration of the pixels, hence they are not included in the analysis. q_e is the charge of an electron. A detailed quantification of pixel noise is presented in [33].

Generally, SNR can be improved by increasing the total imaging time either through a longer exposure time, T_{EXP}, or by averaging multiple images. Alternatively, we can maintain the initial SNR after decreasing T_{EXP}, by averaging to reduce uncorrelated noise by a factor of $\sqrt{n}$ where n is the total number of averages. For the overall measurement time to stay constant, the number of averages can be scaled by the same ratio of downsizing T_{EXP}. SNR of the image with an exposure time of T_{EXP}/n after taking n averages is given by

$$signal = \frac{\sum_{i=1}^{n} x_i}{n} = \frac{1}{n}\sum_{1}^{n}\frac{I_{PD}\frac{T_{EXP}}{n}}{C_{INT}} = \frac{I_{PD}T_{EXP}}{nC_{INT}}$$

$$noise = \frac{1}{n}\sqrt{\sum_{1}^{n}\sigma_i^2} = \frac{1}{n}\sqrt{\sum_{1}^{n}\overline{v_{shot}^2} + \overline{v_n^2}} = \frac{1}{n}\sqrt{\frac{T_{EXP}}{C_{INT}^2}2q_eI_D + n\overline{v_n^2}}$$

$$SNR(n\ T_{EXP}/n) = \frac{signal}{noise} = \frac{\frac{I_{PD}T_{EXP}}{C_{INT}}}{\sqrt{\frac{T_{EXP}}{C_{INT}^2}2q_eI_D + n\overline{v_n^2}}}$$

This equation enables study of the SNR tradeoff between (1) taking a single exposure of T_{EXP} (n=1) and (2) averaging n images with exposures of T_{EXP}/n. The factor of n only appears in the readout noise term. Therefore, if shot noise is the dominant source of noise, for small n, both (1) and (2) result in the same SNR. However, with increasing n and lower exposure time per frame, readout noise dominates the overall noise of the averaged image, necessitating a greater number of averages to maintain the same SNR as a single exposure.

Using the estimated I_{PD} and the measured noise values reported in chapter 6, we calculate that without averaging, a T_{EXP} of 98 ms is required to achieve an SNR of 20 dB (10×). This result corresponds to a minimum required energy ($I_{LD}V_{LD}T_{EXP}$) of 4.16 mJ per image.

Delivering I_{LD}=20 mA from the incident US signal, given a piezo impedance of 5.4 kΩ at 920 kHz, requires an open circuit voltage of at least 108 V, which is not practical within FDA limits. Therefore, harvested energy must first be stored on a capacitor to later supply the lasers when taking an image. To derive requirements for size of the storage capacitor, C_{STORE}, the simplified model of the chip in Fig. 2.9 can be used. The laser driver is modeled with a current source turned on only during the exposure time. During exposure, the current of the laser diode, I_{LD}, dominates the current consumption of the rest of the chip modeled with a single current source.

The size of the storage capacitor, C_{STORE}, is determined by $C_{STORE} = \frac{I_{LD}T_{EXP}}{\Delta V_{CSTORE}}$ in order to supply I_{LD} for the duration of T_{EXP}. ΔV_{CSTORE} is the voltage drop on the capacitor

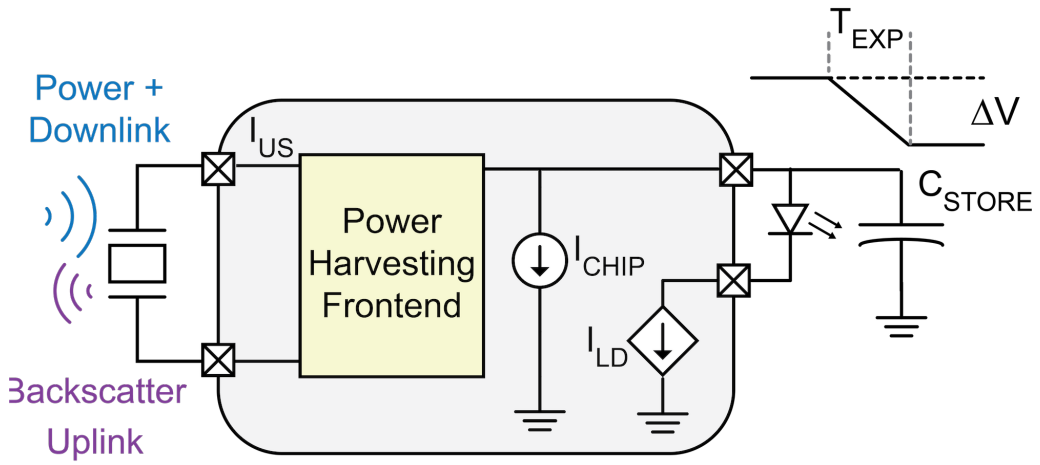

Figure 2.9: Simplified block diagram during the exposure time with linear voltage drop on V_{CSTORE} to supply the laser driver from C_{STORE}.

during T_{EXP}. Maximizing ΔV_{CSTORE} results in a smaller capacitor size, but is limited by the maximum harvested voltage and the minimum supply requirements for operating the chip or laser. Assuming a ΔV_{CSTORE}=3 V, results in a capacitor size of 650 μF. Capacitors of this size are large physical components, increasing implant volume as in [50]. Therefore, the capacitor size can be minimized by reducing the required energy per image by shortening T_{EXP} through the averaging strategy discussed above while keeping I_{LD} and therefore the optical power of the μLD constant.

Fig. 2.10(a) compares SNR of the pixel in a dark image with different levels of averaging. Each data point on the black curve represents an exposure time of T_{EXPi} and a number of averages n_i such that the total exposure time, $n_i T_{EXPi} = 96ms$, stays constant. As T_{EXPi} decreases (and n_i increases), readout noise dominates the pixel output noise (as shot noise decreases with lower T_{EXPi}), requiring additional averages to achieve the same SNR of a single exposure. The orange curve in Fig. 2.10(a) shows the increased number of averages, $x_i > n_i$, required to reach an SNR (shown in blue) within 90% of the initial SNR for T_{EXP}=96 ms. Therefore, using averaging to decrease exposure time for individual frames increases the overall imaging time to greater than 96 ms. As shown in Fig. 2.10(b), the capacitor size decreases linearly with lower T_{EXPi} ranging from 640 μF for T_{EXPi}=96 ms to 50 μF for T_{EXPi}=8 ms. Charging such a capacitor through US takes several seconds to minutes, dominating the frame time (see chapters 4 and 6). Thus, for small exposure times, the additional required averages can significantly increase the total imaging time. The total imaging time must be less than several minutes to capture the motion of immune cells, which have mean velocities of 10 μm/min in the tumor microenvironment [73, 74].

Following these guidelines, we chose an 0805 100 μF tantalum capacitor for C_{STORE} with a size of 2×1.25×0.9 mm^3 (0.002 cm^3). This capacitor can supply 20 mA of laser current for T_{EXP}=16 ms while dropping its voltage by 3 V. Averaging is employed to enhance SNR to

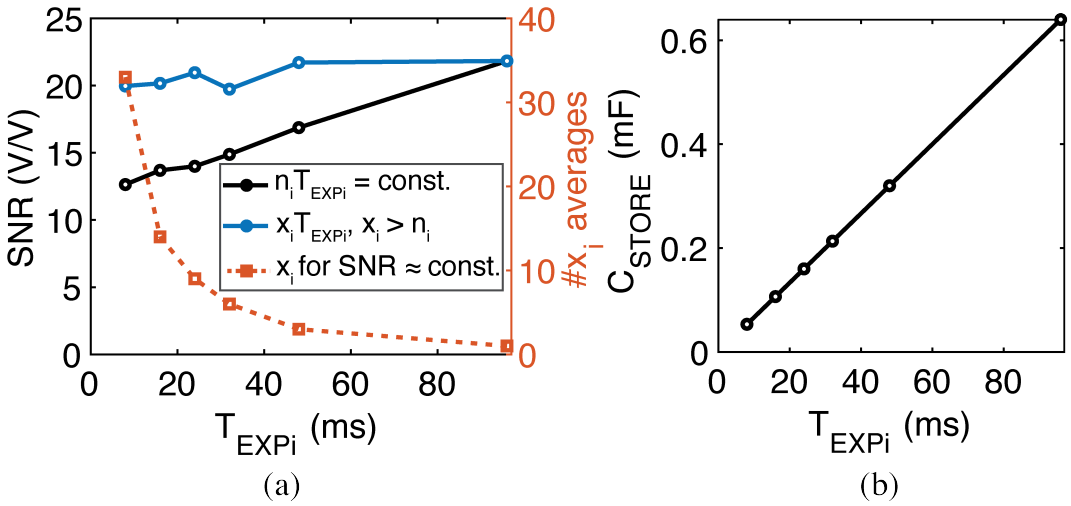

Figure 2.10: (a) SNR of the pixel in a dark image with different levels of averaging. (b) Capacitor size vs. exposure time.

levels comparable to those achieved by longer exposure times. We use a tantalum capacitor as opposed to a ceramic capacitor, which can lose up to 40–80% of its initial capacitance as the DC bias voltage increases, reducing the dielectric permittivity [75].

2.7 FoM for a Wireless Image Sensor

The design of the imager array is based on our previous work in [33]. Each pixel incorporates a 44x44 μm^2 photodiode and has a pitch of 55 μm. The pixels are fabricated in a 180 nm 1.8/5/32 V TSMC CMOS process. Imaging is performed using a global shutter as the μLD only illuminates the sample for a limited time, which is by far the primary power-consuming operation of the imager, and therefore all pixels must image during this limited time window. This demands that each pixel be able to amplify, sample and hold its data until it is read out via a single channel US-based uplink which will be discussed in chapter 3.

The pixel size (W_{pixel}) and the integration (exposure) time (T_{EXP}) are chosen to maximize sensitivity to the dynamics of small cell foci (a few 100 cells) to evaluate the immune response. To capture cell movements in real-time, the pixel must be small enough to track the displacement of cells within consecutive frames. The minimum interval between frames is constrained by the charging time of the storage capacitor as it is used to supply the energy for the μLD during T_{EXP}. Therefore, given a constant power consumption of the μLD, the minimum frame time is a function of the time it is switched on, T_{EXP}. For each T_{EXP}, the pixel dimension must be consistent with the typical displacement of cells with an average velocity of 10 μm/min between each frame.

Pixels with dimensions much larger than this displacement may miss the changes in the cell proliferation profile. Conversely, designing an imager array with the same imaging area using smaller pixels results in unnecessarily oversampling the scene. As discussed in [76] there is a fundamental tradeoff for W_{pixel} between maximizing the signal and maintaining spatial resolution. The received fluorescence signal is proportional to the active area of the photodiodes until the field of view of a pixel matches the size of the foci being imaged. It should be noted that the goal is to track changes in cellular distribution (in response to therapy), and not to obtain intracellular or single-cell imaging. Thus, too small of a pixel will capture noise with only a minimal detected signal which results in a low SNR. The typical $\sim$10 μm dimension of each cell introduces a lower bound for the pixel size. Given the size of the pixel's peripheral circuitry needed to ensure low noise in-pixel amplification and sample and hold, shrinking W_{pixel} lowers both the fill factor and the sensitivity to light. Subtending the same field of view inside the tumor microenvironment with smaller pixels results in larger arrays with higher power consumption and longer readout times. The spatial resolution depends on both the resolution of the angle-selective structures as well as the pixel dimension, and therefore lowering the pixel size significantly beyond the optical resolution will not result in further improvements in resolution. Conversely, larger pixels that reduce spatial resolution collect more dark current in addition to the photodiode signal, both as a linear function of the area. Given that dark current in this technology is the dominant factor restricting the dynamic range of the pixel, larger pixel area results in higher photodiode shot noise limiting SNR and thereby the minimum detectable signal.

To quantify the trade-offs outlined above, we propose a figure of merit (FoM) that incorporates the specifications of both the imaging frontend and the wireless system. The proposed metric consists of 1) SNR to ensure sufficient image quality while capturing multicellular dynamics, 2) spatial resolution to enable resolving small feature sizes, and 3) the value of C_{STORE} ($C_{STORE} = \frac{I_{LD}T_{EXP}}{\Delta V_{CSTORE}}$) which determines the overall device form factor to assess practicality of eventual implantation. Given the importance of image quality (SNR, resolution), and, secondarily the need to miniaturize the form factor of the implant, we propose an FoM given by

$$FoM \;=\; \frac{SNR}{Res \times C_{STORE}\; Size^{.5}}$$

Optimization is performed on W_{pixel} and T_{EXP}. The power of each term is chosen to balance dependency on the order of the independent variables. The size of the device is dominated by the storage capacitor which, given a constant μLD power, is proportional to T_{EXP}. Resolution is proportional to the pixel dimension.

Both the photodiode and dark current are proportional to the area of the pixel $A_{pixel} = W_{pixel}^2$ for square-shaped pixels with a width of W_{pixel}. $V_{SW}$is the maximum voltage swing at the output of the pixel. The maximum voltage generated from the photodiode signal is constrained by the contribution of the dark current in the pixel output voltage (V_{dark}). This introduces an upper bound for the maximum signal that can be detected by each pixel.

The spatial resolution of the imager is defined by the dimension of the pixel and the optical angle selective structures. Assuming that the optical structures provide sufficient resolution, the overall resolution is limited by W_{pixel}. Fig. 2.11 demonstrates FoM and its contours for combinations of W_{pixel} and T_{EXP}. The blurred region corresponds to the design space resulting in SNR values lower than 10 dB which lack adequate image quality for accurate detection of the desired cell clusters. The dashed line represents the lower bound of the pixel size needed to capture cell displacements in consecutive frames. This is computed given average cell velocities (10 μm/min) and the minimum achievable frame time for each T_{EXP}. Oversampling the scene with an imager made with smaller pixels than the lower bound increases the number of pixels, and thereby the power consumption and data transmission period. To maintain adequate resolution in detecting multicellular-level dynamics in the tumor microenvironment, an upper bound on the pixel size is defined as highlighted in Fig. 2.11(b).

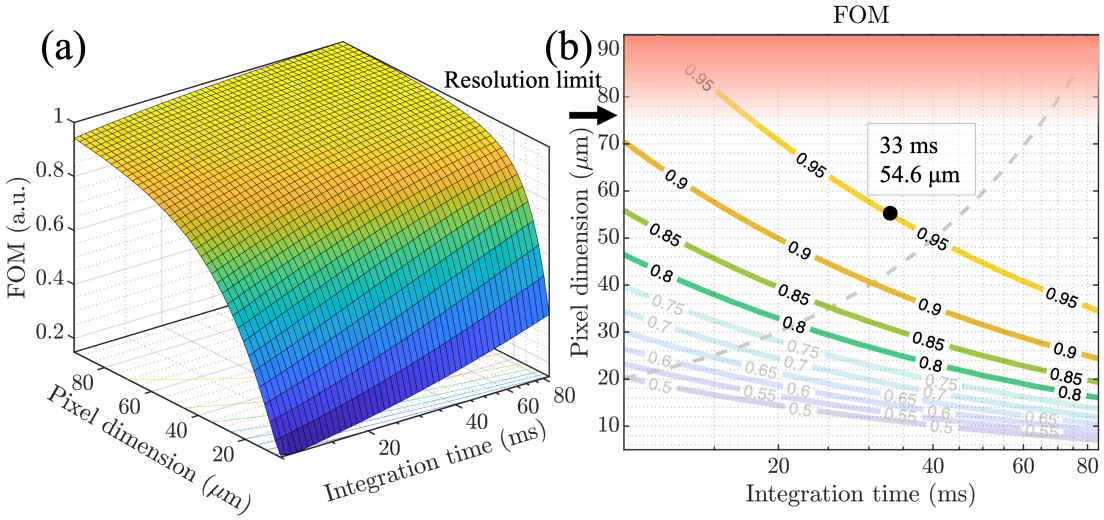

Figure 2.11: (a) Normalized FoM for a range of W_{pixel} and T_{EXP}. (b) FoM contours with 1) blurred regions corresponding to SNR<10 dB, 2) dashed line representing the sufficient lower bound W_{pixel} for each T_{EXP} according to cell dynamics and 3) highlighted region for the upper bound on W_{pixel} to ensure sufficient resolution.

According to the FoM optimization analysis, an imaging array of 36×40 pixels with a 55 μm pitch is chosen to fit a 44×44 μm^2 photodiode, an in-pixel amplifier, and sample and hold circuits for each pixel. To visualize multicellular clusters of a few 100 cells illuminated with the μLD using these pixels, an exposure time equal to 32 ms is chosen to optimize the FoM within 95% of its maximum. With T_{EXP} programmability, our proposed system can maintain a high FoM tailored to capture different cell profiles and fluorescence signal intensities in the tumor microenvironment.

2.8 Contributions

The figures in this chapter are adapted from the following articles:

1. **R. Rabbani***, M. Roschelle*, S. Gweon, R. Kumar, A. Vercruysse, N. W. Cho, M. H. Spitzer, A. M. Niknejad, V. M. Stojanovic, M. Anwar, "17.3 A Fully Wireless, Miniaturized, Multicolor Fluorescence Image Sensor Implant for Real-Time Monitoring in Cancer Therapy," *2024 IEEE International Solid-State Circuits Conference (ISSCC)*, San Francisco, CA, USA, 2024, pp. 318-320. (* Equally credited authors)

2. **R. Rabbani**, H. Najafiaghdam, M. Roschelle, E. P. Papageorgiou, B. R. Zhao, M. M. Ghanbari, R. Muller, V. Stojanovic, M. Anwar, "Towards A Wireless Image Sensor for Real-Time Fluorescence Microscopy in Cancer Therapy," in *IEEE Transactions on Biomedical Circuits and Systems (2024)*.

Acknowledgments: M. Roschelle designed the optical front end for multicolor imaging, characterized the light sources and collaborated in establishing system level specifications. The pixel design and pixel noise contributions were adapted from the work of E. P. Papageorgiou. M. M. Ghanbari contributed to both the design and measurement of the ultrasound link. E. Yang assisted in assembling the piezoceramic. M. Roschelle and A. Vercruysse contributed to the design and assembly of the mechanical package.

Chapter 3

Design of the Single-Color Wireless Fluorescence Image Sensor

Fig. 3.1 shows the block diagram of the ASIC including 4 main functional blocks: (1) power management unit (PMU), (2) imaging front-end, (3) laser driver, and (4) finite state machine (FSM). The PMU incorporates an active rectifier and several low-dropout voltage regulators (LDOs) to supply various subblocks.

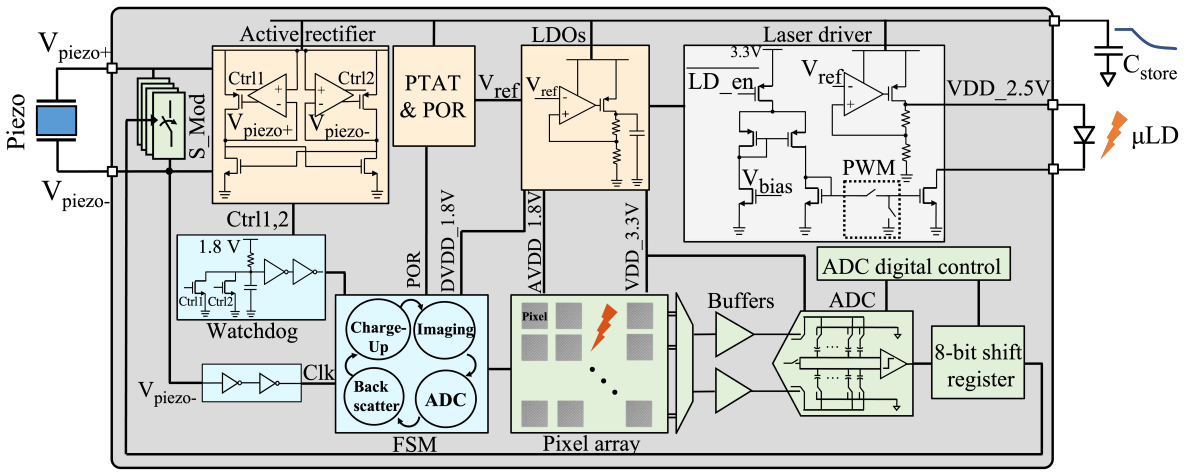

Figure 3.1: Block diagram of the IC including power management, imaging front end, laser driver, and FSM. The IC is connected to the piezoceramic, external C_{store}, and μLD.

The imaging front-end consists of the pixel array shown in Fig. 3.2(a) with the architecture of the pixel and the sample and hold in Fig. 3.2(b) and (c) as discussed in [33]. The imager array is followed by the readout circuitry, buffers, and a differential 8-bit SAR ADC for reading out and digitizing the analog pixel values as illustrated in Fig. 3.1. The laser driver supplies a constant current to the laser diode from the charge stored in C_{store}. The FSM controls the timing and operation of the chip and synchronizes it with the external US

transducer. To obviate the need for bulky optical lenses, on-chip microfabricated structures based on angle-selective gratings (ASGs) with FWHM of 36° are utilized to restrict the angle of incident light resulting in images with higher spatial resolution. The use of ASGs, along with in-pixel electronics, yields an effective fill factor of 28%.

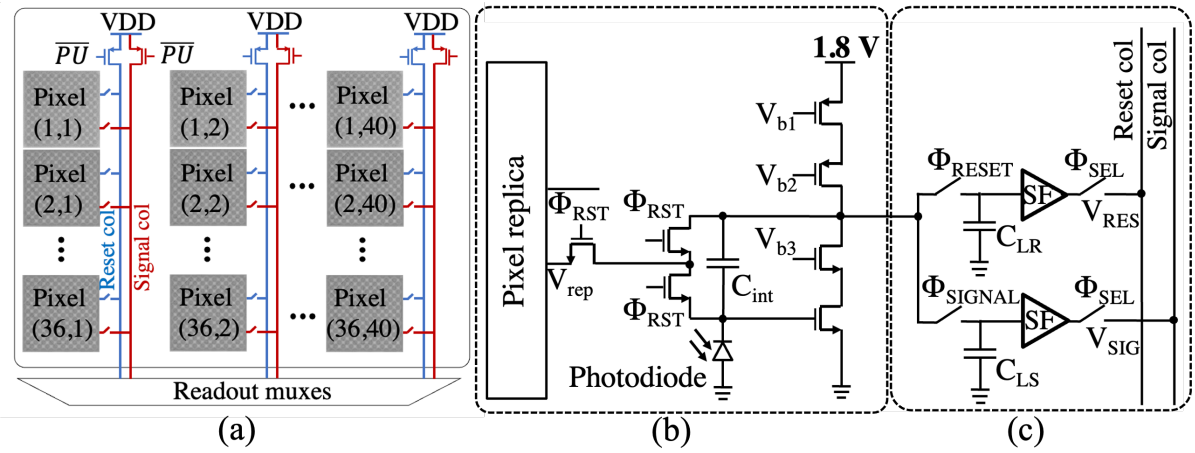

Figure 3.2: (a) Architecture of the imager array. (b) Schematic of a pixel including the photodiode, the pixel CTIA and the replica circuit from [33].(c) In-pixel correlated double sampling.

The micrograph of the ASIC is shown in Fig. 3.3. The chip measures 2.5 mm by 5 mm with the pixel array taking up 41% of the overall area. The design and operation of each block are described in detail in the following:

3.1 Power Management and Control

As shown in the timing diagram in Fig. 3.4, the operation of the chip is divided into 4 states: *Charge-Up*, *Imaging*, *ADC Operation*, and *Backscatter Modulation*. To eliminate the complexity of data downlink and ensure that on-chip state transitions are synchronized with the transducer, the transmitted US carrier is modulated with a pulse sequence. The different pulse widths of the US signal for each state of operation are programmed with an FPGA which controls the output of the US transducer shown in Fig. 3.4 (V_{piezo+}). A watchdog control signal demodulates the incoming US waveform's envelope to navigate the state transitions of the FSM.

The active rectifier converts the US signal to a DC voltage (V_{rect}) while charging C_{store} up to 5 V. To initialize the chip and reset the FSM, an on-chip power-on reset (POR) signal is triggered as V_{rect} reaches 4.2 V to guarantee that the LDO voltages are established. Various on-chip LDOs (1 V, 1.8 V, 2.1 V, 2.5 V, 3.3 V) with a total current consumption of 8.2 μA regulate the supply voltage for the analog front-end, the laser driver, and the FSM. Despite

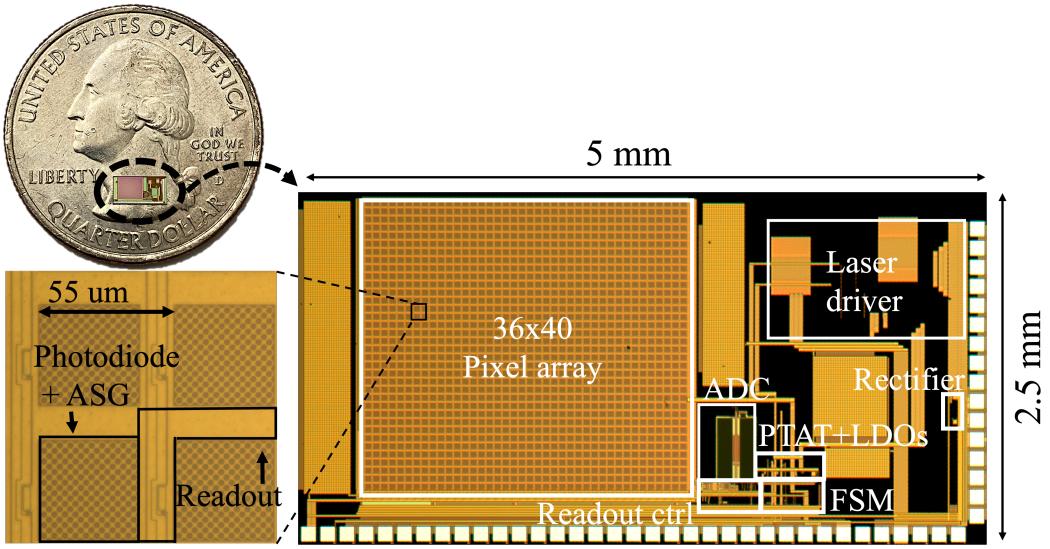

Figure 3.3: Chip micrograph with pixel array measuring 2x2.2 mm^2. Close-up view of the pixel with a 55 μm pitch including a 44x44 μm^2 photodiode area covered with ASGs and the readout circuitry.

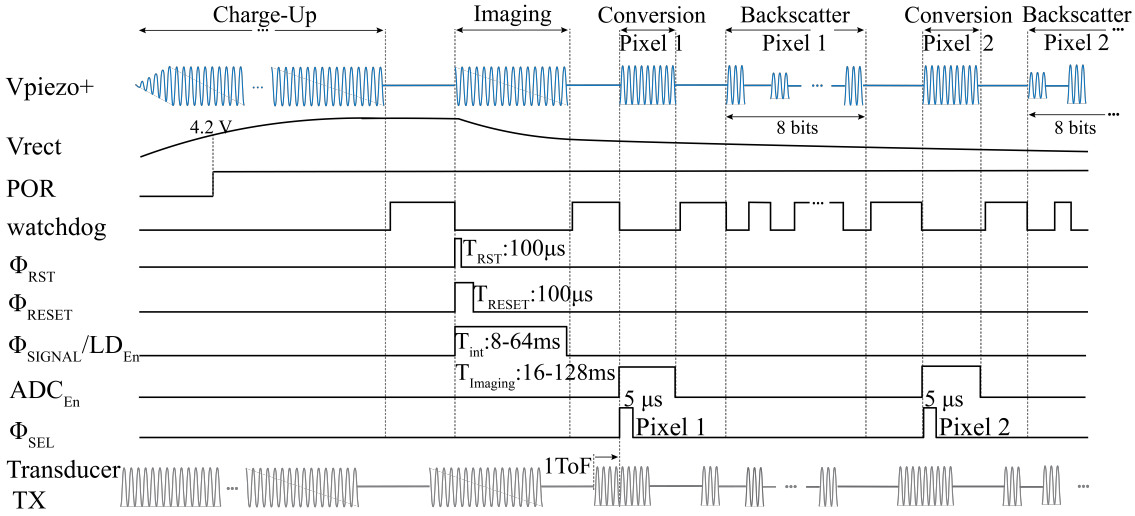

Figure 3.4: Timing diagram and state transitions of the system with the control signals.

the droop in V_{rect} during the *Imaging* state, the LDOs are designed to operate with V_{rect} as low as 3.5 V to ensure the functionality of the device after *Imaging* for *ADC Operation* and *Backscatter Modulation*. A CLK signal with a frequency of 960 kHz is extracted directly from the acoustic carrier.

Power-intensive blocks including the laser diode driver, the pixel array, the ADC, and

the buffers preceding the ADC are turned off during *Charge-Up* to prevent disrupting and extending the chip's power-up. The enable signals for the laser diode driver (LD_{En}), ADC (ADC_{En}), and ADC buffers (Φ_{SEL}) are shown in Fig. 3.4. Followed by the *Imaging* state, the first rising edge of the watchdog signal is indicative of the end of the *Charge-up* period. The exact duration of the *Charge-Up* state can be empirically determined by characterizing the rise time of V_{rect} to reach its final value (5 V) for a given C_{store}. During *Imaging*, the sample is illuminated by the sensor-powered laser diode and after the image is captured, the pixels are read out, digitized, and backscattered sequentially. Each pixel's voltage is wirelessly transmitted by modulating the impedance of the same piezoceramic used for power transfer. Data transmission continues until the watchdog timer counts the entire 1440 pixels based on the transitions of the watchdog signal. The data transfer protocol is discussed later in this chapter.

3.2 Imaging and Laser Driver Operation

During *Imaging*, the photodiodes convert incoming photons from the fluorescently labeled cells into a photocurrent, which is integrated into the feedback capacitor of the pixel CTIAs, C_{int} as shown in Fig. 3.2(b). The output voltage is sampled twice, once at the beginning (V_{RES}), and again at the end of the exposure time (V_{SIG}) generating reference and signal values respectively, which are subtracted from each other to provide the net signal. This correlated double sampling (CDS) approach in Fig. 3.2(c) suppresses offset and low-frequency noise of the pixel. The pixel array is turned on only during the *Imaging* state when it consumes a total current of 145 μA. A detailed design of the pixels is presented in our previous work [33]. The laser driver schematic is shown in Fig. 3.1. To prevent the LD from overheating, the driver supplies the laser diode with 50% duty-cycled 50 kHz current pulses as opposed to a continuous current. Therefore, the integration time is effectively half of the duration of the *Imaging* state (T_{int}=32 ms for a 64 ms *Imaging* state). A PWM controller sets the frequency and duty cycle of the pulses based on the main CLK frequency. The output of the PWM block drives a complementary set of switches to control the current of the laser driver. The supply voltage of the laser driver is regulated to 2.5 V to comply with the maximum voltage allowed for the laser diode. A small off-chip resistor in series with the laser diode can adjust the voltage in case of variations. Based on the signal intensity and size of C_{store}, 8 integration times ranging from 8 ms to 64 ms in steps of 8 ms can be configured into the chip at the package level.

3.3 Data Conversion and Backscattering

Once the image is captured, both the laser driver and the pixel array are switched off and the FSM transitions lead the chip to *ADC Operation* and *Backscatter Modulation* states. At the beginning of each ADC state, the correct row is selected by digital row-driving circuitry.

In each row, the reset and signal voltages of each pixel from CDS are read sequentially and sampled during a 5 μs sampling phase of the differential ADC. During this sampling phase referred to as Φ_{SEL} in Fig. 3.4, the ADC input buffers turn on and the readout circuitry selects the correct pixel from the imager array. The output of the ADC is serialized with an 8-bit shift register and is backscattered using pulsed-echo on-off keying (OOK) modulation to sustain a low bit error rate (BER). Backscatter modulation is realized by altering the electrical load resistance of the piezoceramic which affects the acoustic reflection coefficient of the incident acoustic signal [67]. The pulsed-echo modulation scheme is implemented to separate power and data transfer in the time domain while using a single piezoceramic for both.

The proposed backscatter modulation scheme is shown in Fig. 3.5. For a depth of 2 cm, the 8-bit packet of each pixel is divided into 4 sets of 2 bits fit within the 26.7 μs roundtrip (=2ToF, time-of-flight) of the acoustic waves in oil. The US transducer interrogates the piezoceramic with the modulated waveform shown in Fig. 3.5. After each sequence of 2 bits, the transducer stops interrogating for 2ToF, to eliminate interference from the high voltage power waveform with the weaker backscattered signals. Once the signal reaches the piezo after a single ToF, it is modulated based on the acoustic reflection coefficient resulting from the impedance of the chip, R_{Load}. At the series (f_s) and parallel (f_p) resonance frequencies, the normalized backscattered echo amplitude is proportional to $R_{Load}/(R_{Load}+R_{piezo,s})$ and $R_{piezo,p}/(R_{Load}+R_{piezo,p})$, respectively, where $R_{piezo,s}$ and $R_{piezo,p}$ are the equivalent resistances of the piezo at f_s and f_p. For the rest of the frequencies, the reflection coefficient can be computed given the piezoceramic properties and R_{Load} as quantified in [67]. A modulation switch, S_{Mod} in Fig. 3.1, is used to modulate R_{Load} and ultimately the echo amplitude for OOK modulation. A programmable switch with 4 impedance values (1,2,4,8 kΩ) sets the modulation depth based on the piezoceramic's equivalent impedance at the operating frequency. Finally, after the second ToF, the backscattered signal appears on the transducer which is now in the receiving mode and will be demodulated and post-processed in MATLAB to reconstruct the image.

For each pixel, the FSM alternates between *ADC* and *Backscattering* states until all the image data for a single frame is transferred. The conversion and backscattering for all pixels take 389 ms for an implantation depth of 2 cm.

3.4 Contributions

Some of the figures in this chapter are adapted from the following articles:

1. **R. Rabbani**, H. Najafiaghdam, M. Roschelle, E. P. Papageorgiou, B. R. Zhao, M. M. Ghanbari, R. Muller, V. Stojanovic, M. Anwar, "Towards A Wireless Image Sensor for Real-Time Fluorescence Microscopy in Cancer Therapy," in *IEEE Transactions on Biomedical Circuits and Systems (2024).*

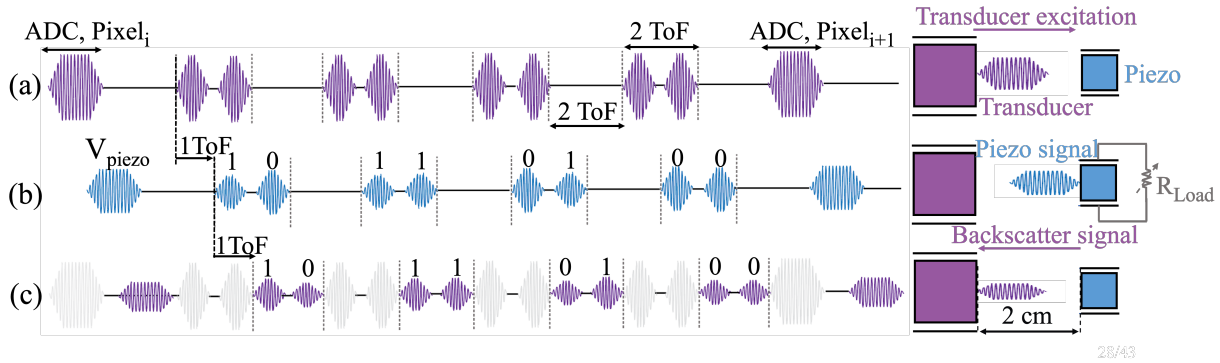

Figure 3.5: Backscatter modulation scheme (a) The US transducer interrogates the piezoceramic with a sequence. (b) After 1 ToF, the piezoceramic receives the signal and modulates the pulses with R_{Load} according to each bit's value (c) The backscattered signal is received by the transducer after a second ToF.

2. **R. Rabbani**, H. Najafiaghdam, B. R. Zhao, M. Zeng, V. M. Stojanovic, R. Muller, M. Anwar "A 36×40 Wireless Fluorescence Image Sensor for Real-Time Microscopy in Cancer Therapy," *2022 IEEE Custom Integrated Circuits Conference (CICC)*, Newport Beach, CA, USA, 2022, pp.

3. **R. Rabbani**, H. Najafiaghdam, M. M. Ghanbari, E. P. Papageorgiou, B. R. Zhao, M. Roschelle, V. M. Stojanovic, R. Muller, M. ANwar, "Towards an Implantable Fluorescence Image Sensor for Real-Time Monitoring of Immune Response in Cancer Therapy," *2021 43rd Annual International Conference of the IEEE Engineering in Medicine & Biology Society (EMBC)*, Mexico, 2021, pp. 7399-7403.

Acknowledgments: B. R. Zhao and M. M. Ghanbari contributed to brainstorming and developing the project. H. Najafiaghdam and B. R. Zhao were involved in the design of various blocks including the LDOs, POR circuit, laser driver. M. M. Ghanbari provided valuable experience and expertise for power management design. The pixel array was adapted from the work of E. P. Papageorgiou.

Chapter 4

Performance of the Single-Color Wireless Fluorescence Image Sensor

4.1 System Characterization

Fig. 4.1(a) shows state transitions of the chip after a 150 s *Charge-Up*. A 64 ms *Imaging* state (T_{EXP}=32 ms) and a portion of the *ADC* and *Backscatter Modulation* states are shown. After a linear 1 V drop during the *Imaging* state, due to the use of a larger 1.2 mF storage capacitor to lower the voltage drop, V_{rect} maintains a voltage higher than 3.5 V. In Fig. 4.1(b), the *ADC* and *Backscattering* states are shown for a single pixel with the modulated piezo signal corresponding to the bit values.

Since V_{rect} cannot drop below 3.5 V to maintain chip operation, we maximize the peak harvested voltage on V_{rect} to allow for minimizing the size of C_{store} for the same acoustic flux. In order to obtain V_{rect} = 5 V, the acoustic power flux density was increased to 905 mW/cm2 which exceeds the FDA-approved limits by 26%. In the future, this can be mitigated by lowering the required harvested voltage and using a voltage multiplier to reach the final 5 V.

Fig. 4.2 shows the setup to visualize the output optical power of the laser driver, measured using the photodiode voltage output of a power meter(PM100D, Thorlabs), V_{pd}. V_{pd} is proportional to the detected optical power and is demonstrated in Fig. 4.3(a) for the duration of the *Imaging* state as V_{rect} drops from 5.2 V to 3 V. As shown in Fig. 4.3(b), V_{pd} is a 50 kHz, 50% duty-cycled signal tracking the current applied to the laser diode.

The laser driver's current is measured through the voltage across a 1.4 Ω resistor in series with the μLD. The laser driver current varies from 38.5 mA to 34.3 mA with a mean of 36.1 mA as V_{rect} drops from 5 V to 3.5 V. These currents correspond to optical powers ranging from 4.4 mW to 2.2 mW with a mean of 2.9 mW. The 11.5% current drop throughout the *Imaging* state stems from the drop in V_{rect} leading to a change in the PTAT output current which determines the laser driver current. This can be improved by using a larger storage capacitor. This results in the laser driver's average electrical efficiency of 50%.

The laser diode used in this work is a class III laser (P_{out}<5 mW). According to the

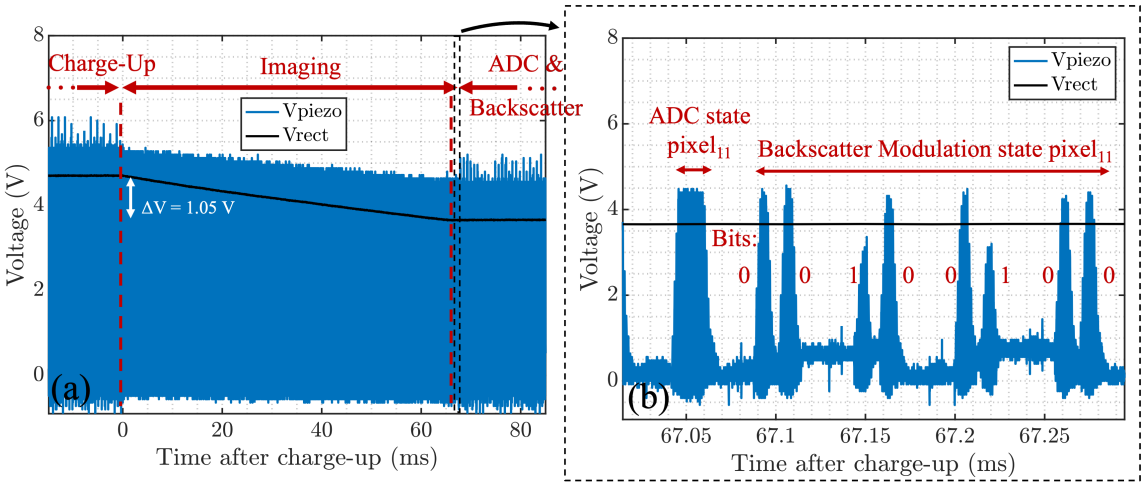

Figure 4.1: (a) Measured waveforms during sections of *Charge-Up*, *Imaging*, and initial part of *ADC* and *Backscatter Modulation* states. (b) *ADC* and *Backscatter Modulation* states for one pixel.

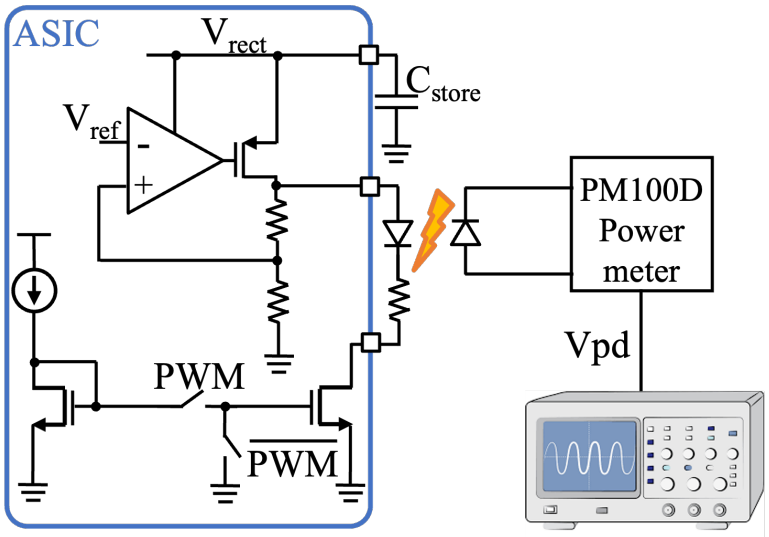

Figure 4.2: Setup for measuring optical power of the laser diode.

American National Standard for Safe Use of Lasers (ANSI Z136.1-2014) the maximum exposure equal to $1.1t^{0.25}$ J/cm^2. Where t refers to the total exposure time of the laser. For an exposure time of T_{EXP}=64 ms, the maximum radiant exposure allowed is 0.55 J/cm^2. With the current optical output power, the radiant exposure He, is 50 mW/cm^2 $\times$ 64 ms = 0.0032 J/cm^2 which is more than 170x lower than the ANSI limit.

The received backscattered waveform is filtered by an FIR bandpass filter in MATLAB to improve signal quality. For measurement performed inside oil at V_{rect} = 5 V (when taking a

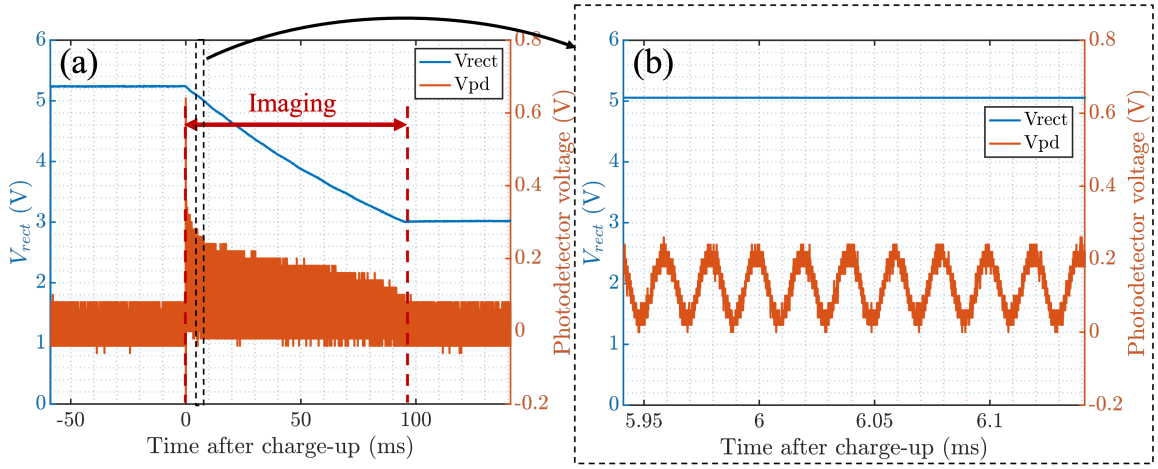

Figure 4.3: (a) V_{pd} during T_{int}= 96 ms. (b) 50% duty-cycled, 50 kHz V_{pd}

dark current image and turning off the laser driver during *Imaging*) the modulation depth is 14.1% and data transmission is error-free for 11.52 kbits of data transmitted resulting in a bit error rate (BER) of better than 8.68×10^{-5}. Lowering V_{rect} to the minimum of 3.5 V decreases the modulation depth to 7.4% increasing the BER to 3.47×10^{-3} for the transmitted data (11.52 kbits). The histograms of the 0 and 1 bits for each value of V_{rect} are shown in Fig. 4.4. Future work to add error correction codes to the on-chip transmitter [77] or further averaging the image can reduce the error in the final reconstructed image.

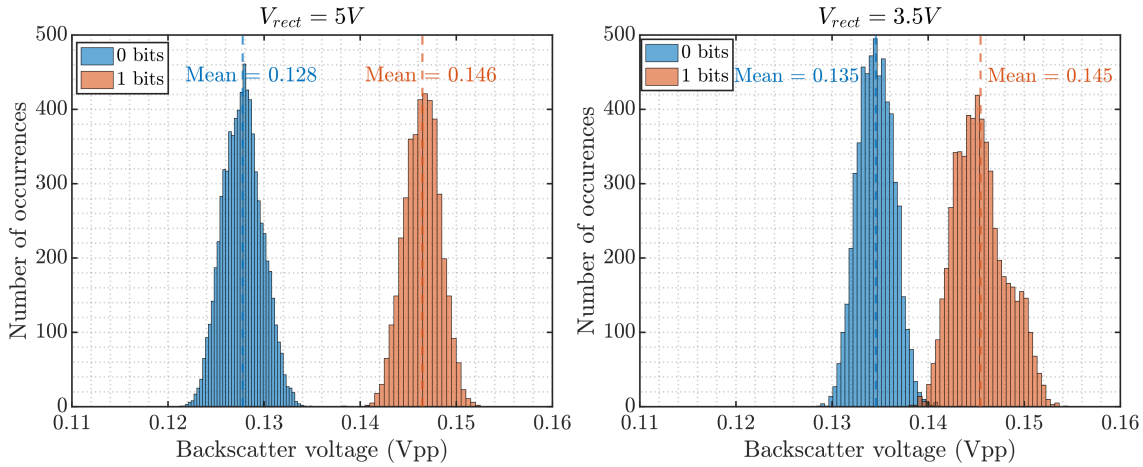

Figure 4.4: Modulation depth of 14.1% and BER $< 8.6\times10^{-5}$ (error-free 11.52 kbits of data) for V_{rect} = 5 V and modulation depth of 7.4% and BER = 3.47×10^{-3} for V_{rect} = 3.5 V.

4.2 Wired Mode *Ex Vivo* Imaging of the Immune Response

The performance of the imaging front-end is tested by imaging *ex vivo* samples of a mouse model of cancer in an experiment monitoring the response to immunotherapy over 18 days.

Experimental Setup

During the therapy, a group of 30 mice (strain: 006772) with a functional immune system (BL6 mice) against cancer (colorectal cancer, MC38 cell line) is selected. For each mouse, the tumor is implanted by injecting 5 x 10^5 cells in 100 μL of MC38 cells in each flank. Once the tumors reach an appropriate size ($\sim$5 mm), the mice are injected with 200 μg of immune checkpoint inhibitors, anti-PD1 and anti-CTLA4 [78, 79], two of the critical therapeutics that activate the immune system against cancer. The injections were repeated every 2-3 days, and 3 mice were collected at each serial time point (spanning 18 days with injection only happening during the first 12 days). The experiment is conducted under IACUC (Institutional Animal Care and Use Committee) protocol AN194778. At each time point, for each of the 3 mice, the draining lymph nodes from the tumor are harvested, fixed in formalin, embedded with paraffin and stained for CD8+ T-cells with the Ventana Discovery Ultra automated slide stainer. To match with the laser diode excitation wavelength, the samples are stained with the Cyanine5 (Cy5) dye-labeled antibodies targeted CD8+ T-cells with absorption and emission peaks at 651 nm and 670 nm, respectively. As a proof of concept, CD8+ T-cell populations in the lymph nodes of the untreated mice (day0, before injection, n=3) as controls and mice at the latest timepoint (day 18, n=3) are imaged with our proposed sensor and a fluorescence microscopy scanner (Axio Scan.Z1, Zeiss), to provide the ground truth.

The experiment setup is shown in Fig. 4.5(a). Illumination is provided with the 635 nm μLD controlled and powered by the chip which illuminates the sample from the top via transillumination. The bottom electrode of the μLD is mounted using conductive epoxy and the top electrode is wire bonded to the board. In future work, the μLD will be mounted on the same platform as the sensor. A 500-μm thick chip-size optical filter (ET FITC-Cy5, Chroma, EM: 675-755 nm) is epoxied on the chip using Sylgard 184 Silicone Elastomer mixed with a 1:10 ratio, degassed to remove any bubbles under a vacuum desiccator (SP Bel-Art) chamber, and then cured at 100°C for 45 minutes. The filter demonstrates OD>6 at the excitation wavelength. More details on the optical frontend are included in our prior work [47]. The edges of the imager are covered with black epoxy (EP1046FG, Resinlab) (1:1 mixing ratio, cured at 65°C for 30 minutes) to eliminate bleed-through from the sides and reflection from the wire bonds as shown in Fig. 4.5(b).

To minimize power consumption, the pixel array is turned off outside the *Imaging* state as described previously. At the beginning of the *Imaging* state, in addition to turning on the pixel array, it is necessary to reset the pixel and drain the previously stored charge on C_{int} with the replica circuit as discussed in [33]. Therefore, with the start of the *Imaging*

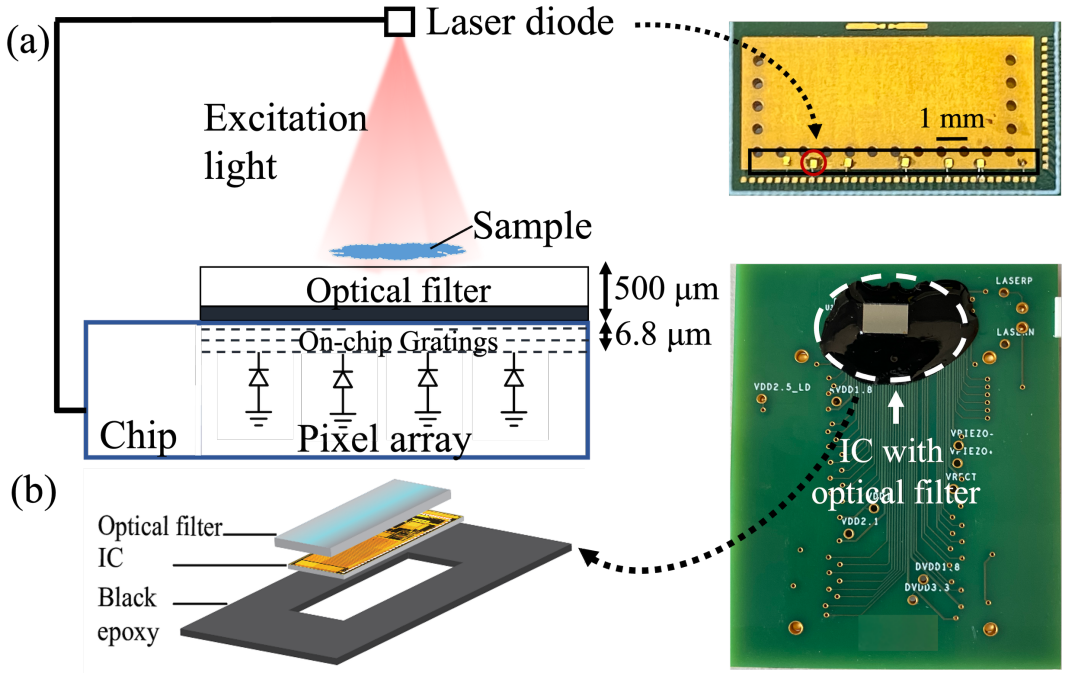

Figure 4.5: (a) Measurement setup for *ex vivo*microscopy in wired mode. The chip is powered up using a 250 kHz sinusoidal from the function generator instead of the 960 kHz piezo input. (b) Fabrication of the imager with the optical filter on the top and black epoxy on the sides.

state, both the pixel array power gating control and the pixel reset control are turned on by the FSM. In cases where the pixel array is not fully switched on during parts of the pixel reset phase, the pixel array settling time affects sensitivity in detecting weak signals from biological samples. In future work, this can be addressed by an earlier start of the pixel array to allow sufficient time for settling before the *Imaging* state. In this work, since the reset timing control is embedded in the FSM, this was only possible by overriding the power gating switch assisted with a wired mode setup while still retaining the power management interface. In future designs, the control over power-gating the imager array will be independently adjustable via the wireless link, ensuring the pixel array is on and in a settled state prior to *Imaging*. For each frame, the serialized pixel data from the on-chip ADC is streamed out to reconstruct the image.

Measurement Results and Analysis

The exposure time of the fluorescence scanner is 2 s and the chip images are taken with T_{EXP}=64 ms. The fluorescence images of the slide samples from untreated and treated mice taken with the scanning microscope and our imager are presented in Fig. 4.6. CD8+ T-cells (shown in pink) are overlaid with the cell nuclei of the entire sample (DAPI, shown in blue).

Compared to untreated control samples, the treated mice at later time points are expected to show a significant increase in the population of CD8+ T-cells indicating successful immune system activation.

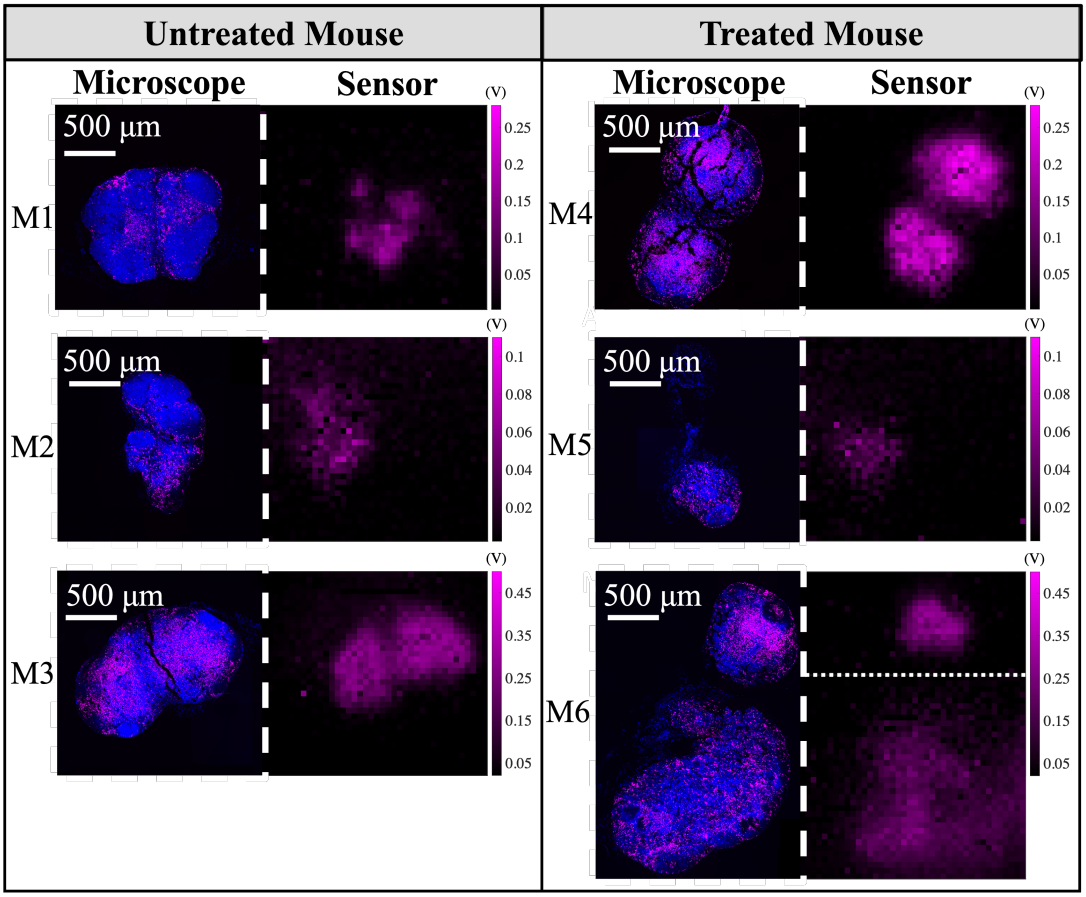

Figure 4.6: *Ex vivo* images from Zeiss fluorescence slide scanner and our sensor. Images from the 3 untreated mice (M1-M3) are shown on the left panel. The images from the mice treated with immunotherapy (M4-M6) are shown on the right. The scale bar is the same for all images. All units are in Volts. The lymph node sample in M6 spans beyond the field of view of the sensor thereby the full image is a composite of 2 overlapping images taken with the sensor.

The images from our proposed system are consistent with the results of the high-resolution microscope. To quantify the therapeutic response, T-cell density in the sample is computed by taking the average CD8+ T-cell intensity divided by the total nodal area imaged. The comparison between CD8+ T-cell density in untreated vs. treated mice is shown in Fig. 4.7. On average, CD8+ T-cell density increases by 9.8% in the microscope images and 17.2% for the sensor images after immunotherapy, however, owing to inherent mouse-to-mouse heterogeneity, there is wide variability in the baseline immune activity in different samples

resulting in outliers such as M3 and M5. Thus, tracking the dynamic response and the change in cell populations is more informative than capturing a single time point image without information about the pre-therapy baseline. This inherent heterogeneity motivates future work for *in vivo* experiments where dynamic changes in response can be observed through implantation of the device without the need for sacrificing the mice and losing the continuous-time data.

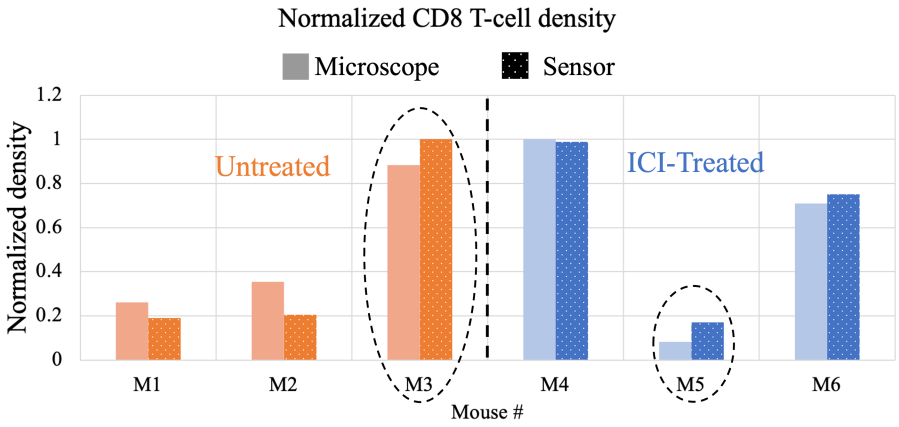

Figure 4.7: Normalized CD8+ T-cell density computed for the sensor and fluorescence microscope images for untreated and treated mice after immunotherapy. The outlier mice samples (M3 and M5) are circled.

4.3 Wireless Mode Imaging

After verifying the performance of the individual blocks including the imager, the overall operation of the system is tested by imaging a fluorescent dye (Cyanine5.5-NHS), distributed underneath a standard resolution test target (USAF, Thorlabs). In this measurement, the acoustic interrogation from the transducer powers up the device to capture an image, and then the backscattered pixel data is transmitted back to the transducer to be processed for image reconstruction.

Experimental Setup

Fig. 4.8 represents the measurement setup. The piezoceramic is placed at a depth of 2 cm away from the US transducer in oil. An acoustic absorber (Aptflex F28P, Precision Acoustics) is used to minimize the reflection from the bottom and sides of the tank. The transducer is controlled by a high-voltage pulser board (Max14808, Maxim Integrated) which is digitally controlled by an FPGA (Opal Kelly XEM6010) to apply the desired interrogation sequence to the chip as previously presented in Fig. 3.4 (V_{piezo+}). Externally, the piezoceramic

is connected to the chip in the optical setup where it is fabricated with the optical filter (ET FITC-Cy5, Chroma). The USAF resolution target is covered with Cyanine5.5-NHS (Excitation: 683 nm, Emission: 703 nm) underneath and is positioned on top of the imager array to evaluate the image resolution.

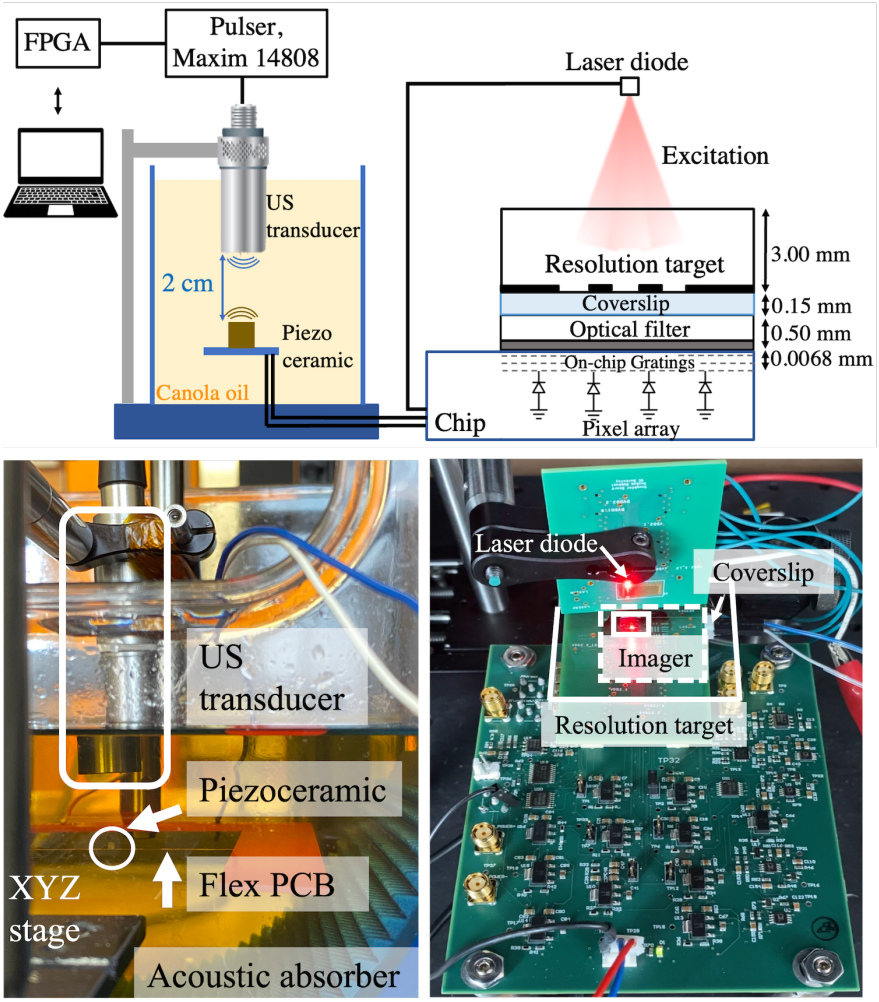

Figure 4.8: Measurement setup for imaging patterns on a USAF resolution target covered with a coverslip containing Cy5.5 fluorescent dye. The image on the right is a snapshot of the instant the laser diode is turned on. For visibility purposes, a positive USAF resolution target is chosen over a negative pattern to show the components underneath the target.

Backscattered Images

The backscattered images taken from the highlighted regions on the resolution target are shown in Fig. 4.9. The images are taken after a 150 s *Charge-Up*. Instead of a continuous

waveform, the ultrasound interrogation is 40% duty-cycled to ensure the safe operation of the transducer without being overheated. The images are taken after a T_{EXP}=32 ms and the backscattered data after a total readout time of 389 ms is captured by the transducer. The frame time is sufficient to capture the movements of cells inside the body [73, 74]. Our platform is successful in distinguishing metallic patterns and features as small as 140 μm with a contrast higher than 87%, making it a viable solution for the detection of clusters of a few hundred cells in immunotherapy. Contrast is calculated from $(V_{max}\text{-}V_{min})/(V_{max}+V_{min}\text{-}2V_{bk})$, where V_{max} and V_{min} are the values of the bright and dark pixels in a row scan inside the region of interest and V_{bk} is the background signal. The outlier pixels in the dark region correspond to the BER while backscattering with the lower V_{rect} values. Taking multiple images and averaging can further improve image quality.

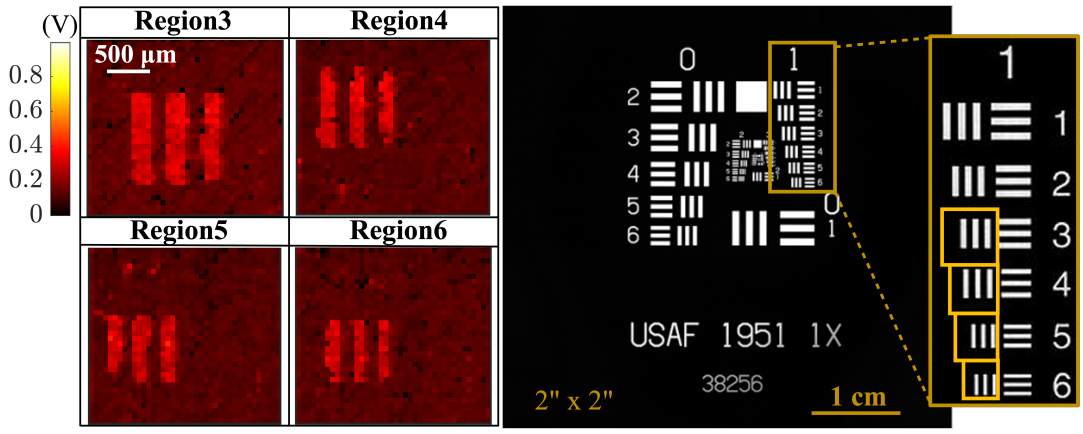

Figure 4.9: Backscattered images from the highlighted regions on the USAF resolution target. The scale bar is in Volts.

Image Outlier Correction

In wireless measurements, the bit error rate from backscattering can lead to outlier pixels in the reconstructed images. The outliers can be detected with an algorithm that compares the value of each pixel with the surrounding pixels. For each pixel, the mean and standard deviation of the 8 neighboring pixels is computed (except for the edge or corner pixels with 5 and 3 neighboring pixels respectively). Once the pixel value falls outside a certain range according to the statistics of the surrounding samples ($\mu \pm 2\sigma$ in this case, where μ is the mean and σ is the standard deviation of the neighboring pixels excluding the pixel of interest), its value is replaced by the average of the surrounding pixels. The algorithm is built on the function proposed in thislink. The images before and after applying the outlier detection are shown in Fig. 4.10.

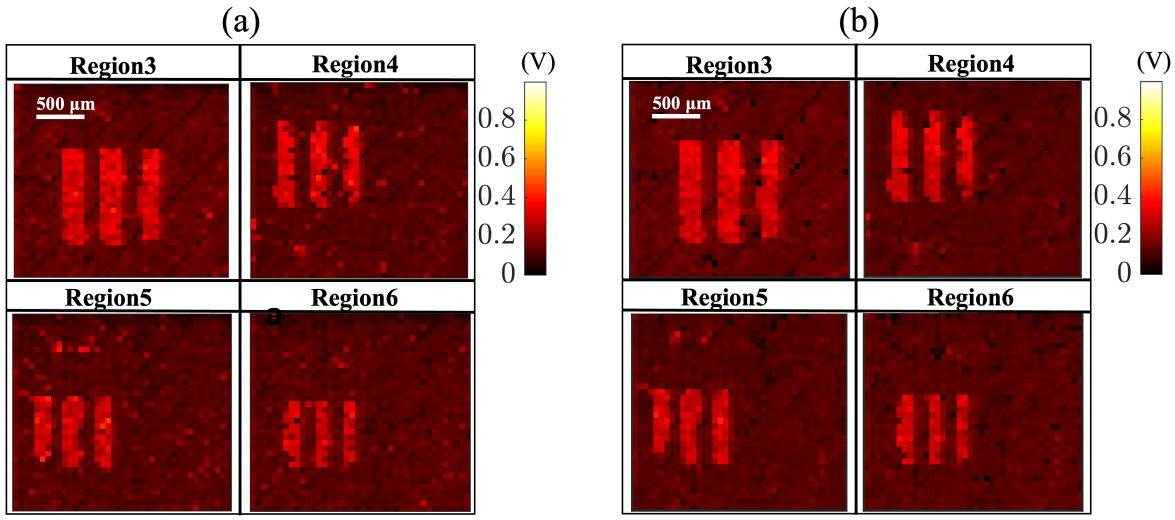

Figure 4.10: Outlier detection and correction for backscattered images. (a) Initial image. (b) Same image after outlier removal. The units of pixels are in Volts and the scale bar is the same for all images.

4.4 Comparison of Current Illumination with Implanted Setup

The implanted setup in the conceptual diagram in Fig. 1.2 requires the laser diode to be assembled next to the sensor while illuminating the target via epi-illumination. Compared to trans-illumination in the current setup shown in Fig. 4.8, epi-illumination lowers the background signal due to the excitation light being reflected off the surface of the sample and not directly incident on the surface of the imager. This can positively affect signal-to-background ratio. However, there are additional effects on signal intensity that need to be addressed:

1. **Spacer thickness:** To deliver light via epi-illumination from the edge emitter laser diode to the sample, a glass spacer between the sensor and the target is required. The thickness of the spacer increases the distance between the source and the target lowering the light intensity absorbed by the fluorophores due to spreading of the laser beam. This effect can be studied using the simplified illumination models shown in Fig. 4.11.

   The intensity of the light received incident on the same surface area of the sample in both cases can be calculated as shown below:

   $$E = I/d^2$$

   E is the irradiance at distance d from a point source of light with an overall intensity

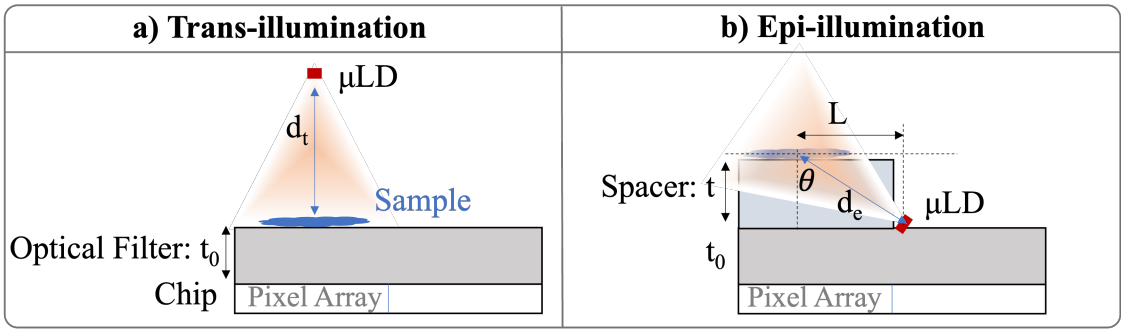

Figure 4.11: Trans-illumination and epi-illumination setups with the chip, optical filter, μLD and glass spacer. The pixel array covers 40% of the chip area. The spacer length (L) is the same as the pixel array length (2.2 mm). The μLD is placed as close as possible to the spacer.

of I.

$$P_{sample,trans} = E_{trans}\ A_{Sample}$$

Where $P_{sample,trans}$ is the light intensity received by a surface area of A_{Sample} trans-illuminated from a distance of d_t.

$$P_{sample,epi} = E_{epi}\ cos\theta\ A_{Sample}$$

Where $P_{sample,epi}$ is the light intensity received by a surface area of A_{Sample} from epi-illumination at a distance of d_e and incident angle of θ. The irradiance at the sensor surface from the fluorescent sample is proportional to:

$$E_{sensor,trans} \propto P_{sample,trans}\ 1/(t_0)^2$$

$$E_{sensor,epi} \propto P_{sample,epi}\ 1/(t+t_0)^2$$

Where t is the thickness of the glass spacer and t_0 is the thickness of the optical filter.

2. **Reflection due to oblique incidence:** Compared to normal incidence, oblique illumination increases reflection at the interface between air and the spacer reducing the transmitted light to the target. The reflection of light at the intersection of air and a second medium with a refractive index of n can be calculated from:

$$R_p = (\frac{cos\phi - ncos\alpha}{cos\phi + ncos\alpha})^2$$

$$R_s = (\frac{cos\alpha - ncos\phi}{cos\alpha + ncos\phi})^2$$

Where R_p and R_s refer to reflections of TM and TE waves, respectively [80]. α is the angle of the incoming beam in air and ϕ is the angle of the transmitted rays in the second medium. For normal incidence reflection can be simplified to

$$R = (\frac{1-n}{1+n})^2$$

The ratio of light transmitted at the intersection of air and the medium n can be calculated from:

$$T = 1 - R$$

Assuming n=1.45 for tissue, 96.6% of the light will reach the sample in Fig. 4.11(a). For oblique incidence, the transmitted power from air to glass (n=1.5) for a range of incoming angles is shown in Fig. 4.12(a). The reflection coefficient is not calculated for the interface of glass-tissue because of their similar refractive indices.

Combing the effect of distance (part 1) and reflection (part 2) the relative irradiance of the emitted light for the same laser power is plotted as a function of the thickness of the spacer in Fig. 4.12(b). The process is repeated for a range of μLD-sample distances in trans-illumination. The plots are generated considering a 500 μm thick optical filter, s-polarized light with lower transmission for worse case, and L=2.2 mm in Fig. 4.11(b). The dashed lines are generated considering the effect of reflection for both trans-illumination and epi-illumination.

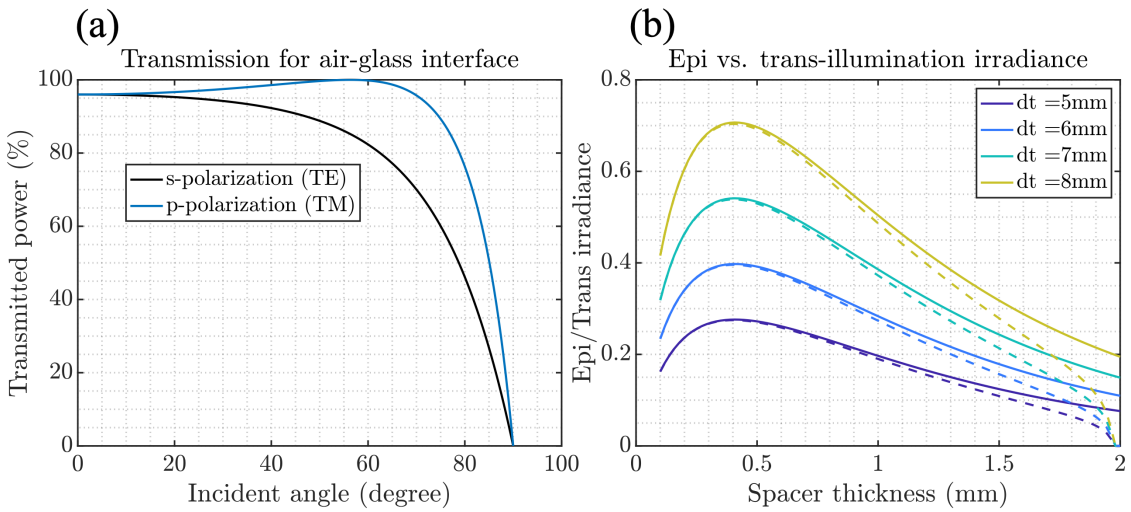

Figure 4.12: (a) Transmission of light from air to glass for different incoming angles of incident. (b) comparison of the irradiance between epi-illumination and trans-illumination across spacer thicknesses.

As shown in Fig. 4.12(b), compared to trans-illumination at distance of d_t=7 mm (similar to the experimental setup), with an optimized spacer width of 400 μm, the intensity is reduced by 45% for epi-illumination. The loss in signal intensity can be improved by increasing the integration time for each frame. Another effect is the lower resolution due to the larger distance of the sample from the sensor caused by the spacer which linearly diminishes resolution [81].

4.5 US Envelope Detection Glitches

The schematic of the watchdog circuit is shown in Fig. 4.13(a). The inputs V_{CTRL+} and V_{CTRL-} are generated in the active rectifier with the architecture shown in Fig. 4.13(b). Upon arrival of the US signal on the piezo terminals, transistors M1 and M2 pull watchdog down. During the rise time of the US carrier, due to the lower strength of V_{CTRL+} and V_{CTRL-} in turning on M_1 and M_2 fully, the internal node V_0 will not be fully pulled down, therefore resulting in glitches at the onset of the US signal at the falling edge of the watchdog.

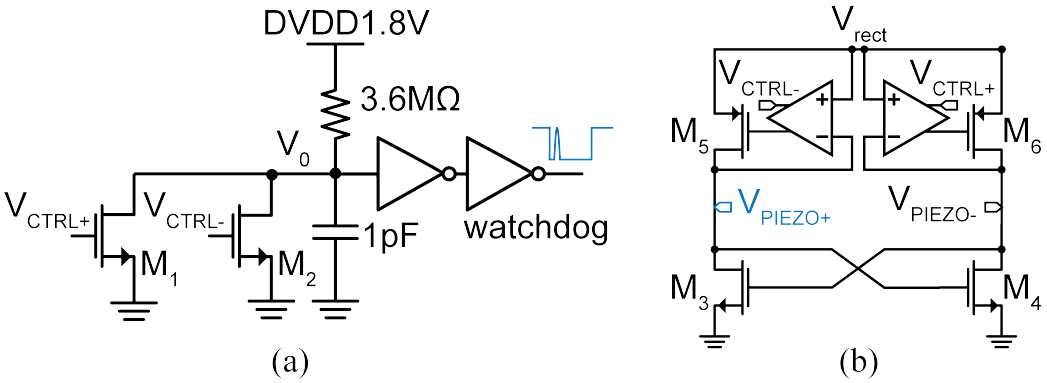

Figure 4.13: (a) Schematic of the watchdog circuit with glitches. (b) Generation of V_{CTRL+} and V_{CTRL-} in the active rectifier.

An example of a watchdog glitch is demonstrated in Fig. 4.14. Due to the significance of watchdog in controlling the state transitions of the FSM, any wrong transition interrupts the operation of the ASIC during operation. A custom digital control circuit is proposed in chapter 5 to eliminate the glitches in the watchdog upon the arrival of the US signal.

4.6 Sensor Frontend Sensitivity

The choice of the 250 kHz sinewave instead of the 960 kHz frequency was driven by the need to lengthen the initial reset phase of the pixel array. As shown in Fig. 3.2(b), the pixel is reset (during Φ_{RST}) at the onset of *Imaging* to remove any previously stored charge on the integration capacitor C_{int}. Φ_{RST} is set to ~100 μs assuming a 960 kHz clk extracted

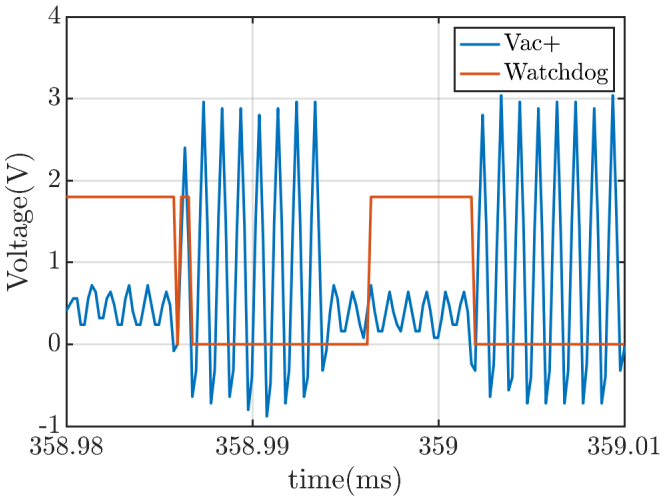

Figure 4.14: Glitch at the falling edge of watchdog.

from the AC input's frequency (either piezo or sinewave from the function generator). As mentioned, the pixel array is power-gated to turn on only during the *Imaging* state to save power. However, some of the pixel biasing circuits require more than 100 μs to settle after activating the pixel array power gating switch. Because the control for turning on the pixel array and Φ_{RST} from the FSM are shared on the chip, some pixel array biasing circuits are not fully settled during Φ_{RST}. Without the pixel array fully settled during Φ_{RST}, the imager sensitivity in detecting weak signals from biological samples is compromised. To address this, a lower frequency source (250 kHz) has been used instead of the piezo to increase the duration of reset to 400 μs to provide the pixel array with additional time to settle before the reset phase is over. Below, pixel sensitivity to input light from an LED with varying currents is plotted for different durations of Φ_{RST} for a pixel with a 1 V dynamic range.

Fig. 4.15 shows the improvement in the sensitivity of the pixel for a t_{RST} = 400μs compared to the nominal 104 μs achieved with 960 kHz clk.

4.7 In-pixel Leakage

As shown in Fig. 4.16, the correlated double sampling scheme involves sampling the reset and signal values on C_{LR} and C_{LS} capacitors, respectively. The reset value is sampled shortly after the start of the *Imaging* state (after 200 μs) and the signal value is sampled after the exposure time (ranging from 8-64 ms). The sampling capacitors (200 fF) are larger than C_{int}=11 fF to hold the data for a longer time. Despite the use of larger sampling capacitors, the pixels at the lower rows of the array suffer from leakage. This leakage issue can be addressed by implementing a faster readout with more ADCs working in parallel, allowing for improved data storage in a memory block in future work. Another additional approach is

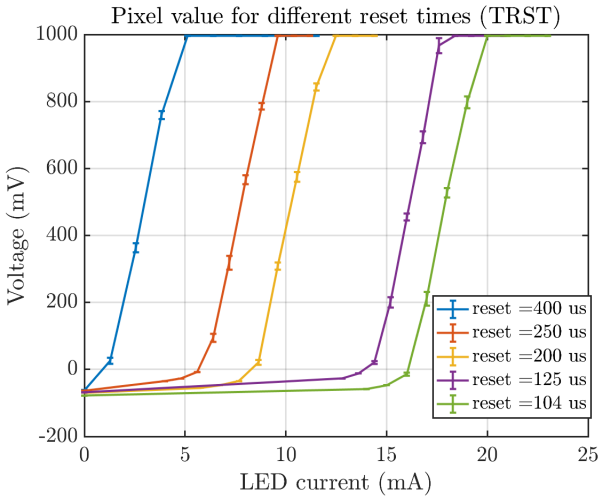

Figure 4.15: Pixel output voltage across LED currents for different T_{RST} values.

decoupling readout from data transmission such that the readout speed is not determined by the speed of the communication protocol. For example, the pixels could be quickly digitized and stored in memory prior to wireless data transmission. Simulation models for leakage in this process are not highly accurate; therefore, the following measurement was conducted to characterize leakage during the readout. The reset (V_{RES}), signal (V_{SIG}), and differential (V_{DIFF} = V_{SIG}-V_{RES}) values are shown after a 100 ms exposure time. During readout, both sampling switches (Φ_{RESET} and Φ_{SIGNAL}) are open and the sampled values decay due to leakage through the switch. (The gate leakage of the source follower amplifiers is negligible). The decay is voltage-dependent resulting in up to 100 mV decay after 389 ms for typical values of V_{DIFF}.

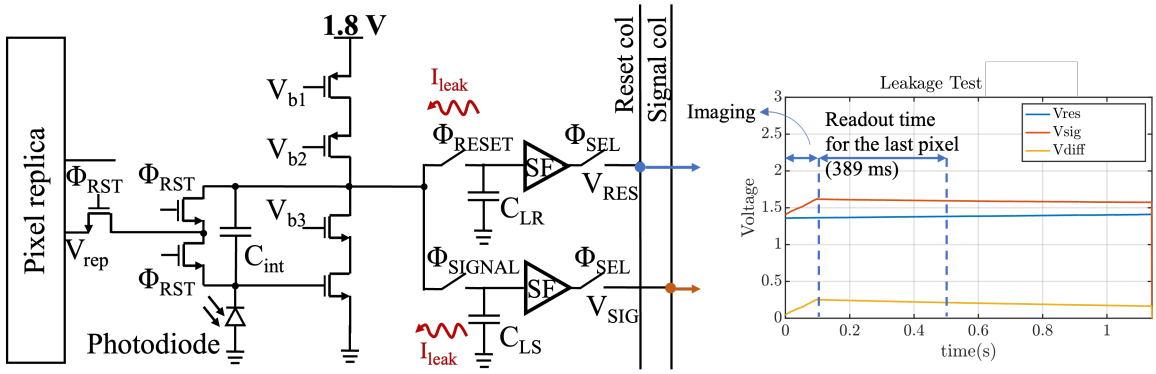

Figure 4.16: Leakage effect on V_{RES} and V_{SIG} voltages over the data transmission period

4.8 Contributions

Some of the figures in this chapter are adapted from the following articles:

1. **R. Rabbani**, H. Najafiaghdam, M. Roschelle, E. P. Papageorgiou, B. R. Zhao, M. M. Ghanbari, R. Muller, V. Stojanovic, M. Anwar, "Towards A Wireless Image Sensor for Real-Time Fluorescence Microscopy in Cancer Therapy," in *IEEE Transactions on Biomedical Circuits and Systems (2024)*.

2. **R. Rabbani**, H. Najafiaghdam, B. R. Zhao, M. Zeng, V. M. Stojanovic, R. Muller, M. Anwar "A 36×40 Wireless Fluorescence Image Sensor for Real-Time Microscopy in Cancer Therapy," *2022 IEEE Custom Integrated Circuits Conference (CICC)*, Newport Beach, CA, USA, 2022, pp.

3. **R. Rabbani**, H. Najafiaghdam, M. M. Ghanbari, E. P. Papageorgiou, B. R. Zhao, M. Roschelle, V. M. Stojanovic, R. Muller, M. ANwar, "Towards an Implantable Fluorescence Image Sensor for Real-Time Monitoring of Immune Response in Cancer Therapy," *2021 43rd Annual International Conference of the IEEE Engineering in Medicine & Biology Society (EMBC)*, Mexico, 2021, pp. 7399-7403.

Acknowledgments: M. M. Ghanbari assisted with the measurement process. M. Roschelle designed the optical frontend.

Chapter 5

Design of the Multicolor Wireless Fluorescence Image Sensor

Fig. 5.1 shows the system block diagram of the ASIC with external connections to the piezo, off-chip storage capacitors, and μLDs. The ASIC has 4 main subsystems: (1) PMU, (2) digital control, (3) laser driver, and (4) imaging frontend with readout.

The PMU consists of an active rectifier for high-efficiency AC-DC conversion of the piezo signal and a charge pump for generating an up to 6 V supply for driving the lasers. Harvested energy is stored on two off-chip capacitors, C_{VCP}=10 μF and C_{STORE}=100 μF, which supply power to the sensor throughout its operation. A PTAT develops current and voltage references and several LDOs generate stable DC power supplies for the chip. The sensor is programmed and controlled through a finite state machine (FSM) with 6 states of operation: charging up the storage capacitors (*Charge-Up*); programming the image sensor and laser driver parameters through US downlink (*Set* T_{EXP} and *Set LD*); taking an image (*Imaging*); digitizing and storing the image (*Readout*); and wirelessly transmitting the data through US backscatter (*Backscattering*). To take an image, the laser driver, configured during downlink, supplies a μLD using energy stored in C_{STORE}. The image is captured on a 36x40-pixel array. During *Readout*, the pixel data is digitized by 4 parallel ADCs and saved in the memory. Finally, image data is transmitted by modulating the reflected amplitude of incident US pulses with the S_{MOD} switch. The design and operation of the subsystems are described in detail below.

5.1 Power Management Unit

Fig. 5.2 shows the schematic of the active rectifier and charge pump. The active rectifier converts the harvested AC signal on the piezo to a 3 V DC voltage (V_{RECT}), which is stabilized by a 4.7 nF off-chip capacitor. V_{RECT} is then multiplied by 1.83x to a 5.5 V supply (V_{CP}) with the cross-coupled charge pump. The cross-coupled topology is chosen for its high power conversion efficiency for an optimized input range [82]. Compared to a rectifier-only

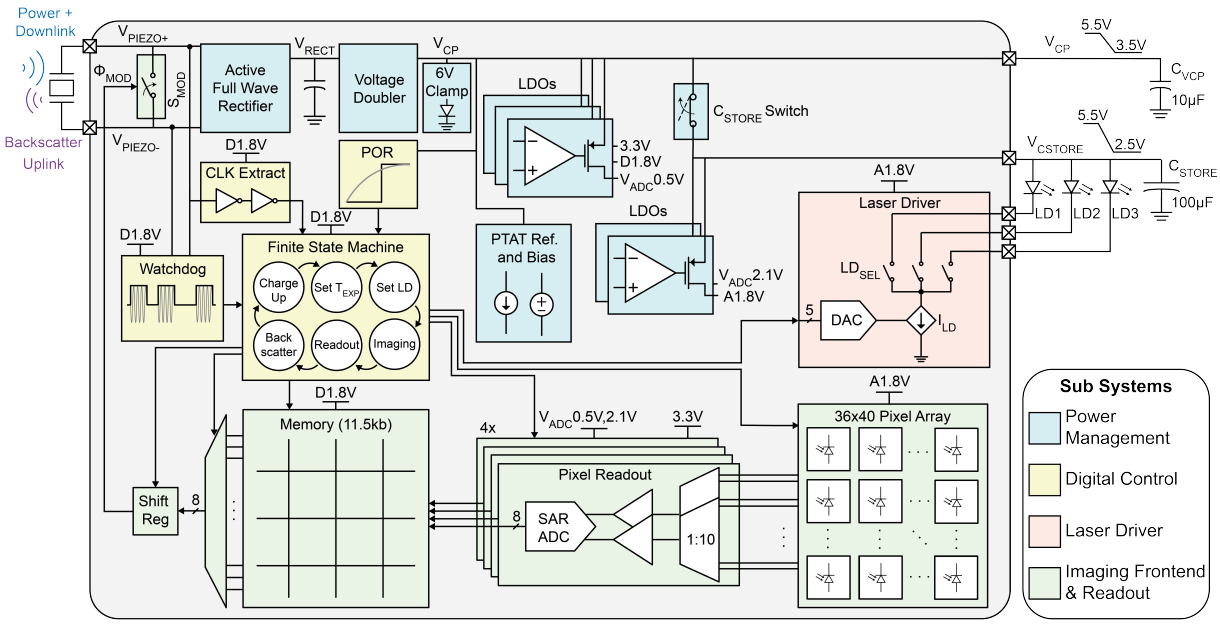

Figure 5.1: System block diagram.

architecture used in chapter 3, the charge pump reduces the required harvested AC voltage on the piezo (V_{piezo}) to achieve an output voltage (V_{CP}) of 5.5 V by 1.7x, which results in a 3x lower acoustic power density requirement. Acoustic power density is a square function of acoustic pressure which is linearly proportional to the harvested AC voltage governed by the following equation:

$$\text{Acoustic power density:} I = \frac{p^2}{\rho c}, p \propto V_{PIEZO} \propto V_{RECT}$$

where p is the pressure of the acoustic waves, ρ is the density of the propagating medium and c is the velocity of sound in the propagating medium. Lowering the required harvested piezo voltage reduces the acoustic power density to ensure operation within FDA safety limits. However, with this architecture, the overall charging time increases due to the energy loss from the charge pump. A diode-based voltage clamp prevents charging beyond 6 V to protect the devices from overvoltage.

During *Charge-Up*, C_{VCP} and C_{STORE} are connected through the C_{STORE} switch and are charged through the PMU. C_{STORE} stores energy for the lasers and imager array and a smaller C_{VCP} stores energy for the readout and digital control. The external US transducer is duty-cycled to prevent overheating. To minimize power consumption during, the laser driver, pixel array, readout circuits and memory are switched off. Five LDOs regulate the harvested voltage into stable DC power supplies and are compensated with off-chip 0201 surface mount capacitors (10-200 nF). They generate reference voltages of 0.5 V and 2.1 V for the ADCs, separate 1.8 V power supplies for the digital control and for the pixel array and laser driver

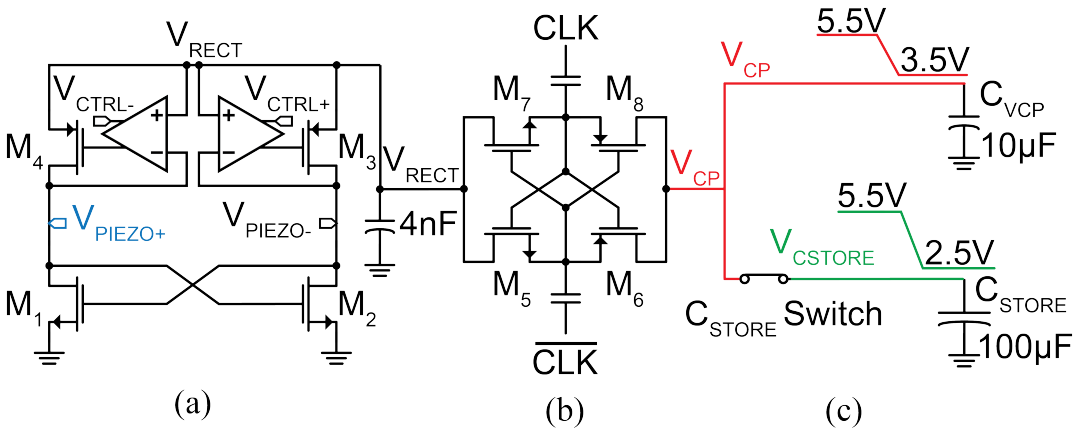

Figure 5.2: PMU schematic consisting of (a) full-wave active rectifier, (b) cross-coupled charge pump, and (c) storage capacitors.

biasing, and a 3.3 V supply for the readout. A PTAT circuit generates a 200 nA reference current, and 1 V and 0.5 V references to bias the chip. To ensure that generated references are stable across the large voltage drop on V_{CP} from 5.5 to 3.5 V, cascode current mirrors with high output impedance are used throughout the design.

5.2 Digital Control

The chip operates according to the system timing diagram shown in Fig. 5.3. When VCP reaches 3.9 V, ensuring stable operation of the chip, the FSM is initialized by a power-on-reset (POR) circuit. The FSM is synchronized to the external US transducer by on-off-key modulation of the US envelope, which is demodulated by a watchdog circuit.

The schematic of the watchdog circuit is shown in Fig. 5.4. A latched-based control eliminates glitches in detecting the presence of the US pulses within 3 μs of the initial rising edge. The unwanted transitions result from insufficient drive strength of the AC inputs to transistors M1 and M2 during the gradual ramp-up of the US pulse. To relay timing information to the FSM, the clock is extracted from the US carrier frequency (920 kHz). An US pulse longer than 1 ms indicates the end of the *Charge-Up* state. At this moment, the C_{STORE} switch is opened to isolate the storage capacitors allowing V_{CSTORE} to drop to a minimum of 2.5 V during *Imaging* while maintaining V_{CP} above 3.5 V for the 3.3 V readout. This approach allows for maximum energy usage from C_{STORE}, resulting in a 33% smaller required capacitance assuming a 5.5 V charge-up voltage.

After *Charge-Up*, the IC is programmed during the *Set* T_{EXP} and *Set LD* states. As shown in Fig. 5.3, the transmitted downlink data is decoded through time-to-digital conversion of the US pulse width. In each state, 4 LSBs are discarded to account for timing variations in the watchdog signal. In *Set* T_{EXP}, the exposure time, T_{EXP}, is set through the 4 MSBs

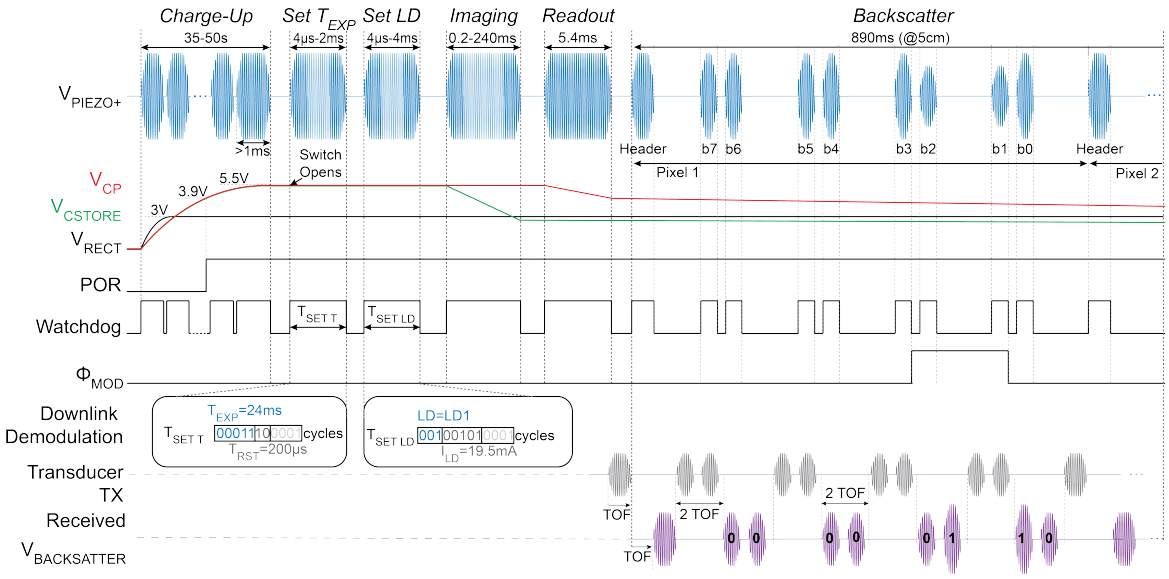

Figure 5.3: System timing diagram.

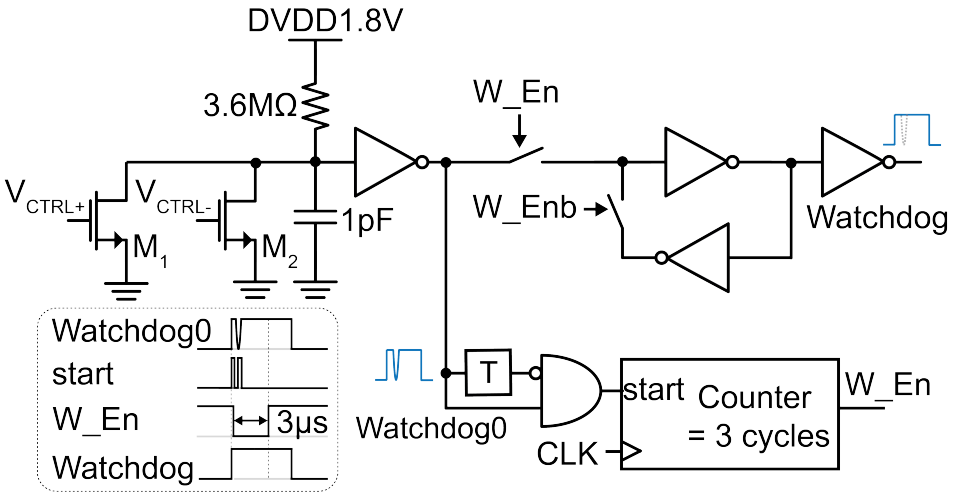

Figure 5.4: Schematic of watchdog circuit with error-free edge detection.

and is programmable from 0-248 ms with an LSB=8 ms. The next 2 bits set the pixel reset time, T_{RST}, which can be 100, 200, 500, or 1000 μs. In *Set LD*, 3MSBs set the 1-hot encoded laser channel and the next 5 bits determine the laser current, ILD. On the falling edge of the watchdog after *Set LD*, the laser driver and the pixel array bias circuits are turned on to prepare for *Imaging*.

5.3 Laser Driver

Fig. 5.5 shows the schematic of the 3-channel laser driver with programmable output current. To minimize the change in driver current, ILD, across the large voltage drop on VC_{STORE} (5.5-2.5 V), the driver must have high output impedance. Therefore, a gain-boosted cascode current source topology is used. With this topology, the output impedance of the current source (M_8-M_{15}) is multiplied by the 65 dB gain of the cascode boost amplifier (M_4-M_7). A 5-bit current DAC (M_{11}-M_{15}) enables a programmable output current from 0-115 mA with a 3.9 mA LSB to supply the laser diodes with different bias currents according to the PIV curves in Fig. 2.4. Since only one laser is turned on at a time, the same driver circuitry is used for all three lasers. Therefore, the cascode transistors also serve as select switches for the laser channels. For maximum output swing, V_x is set by a level-shifting diode, M_3, to bias M_{11}-M_{15} at the edge of the triode. A headroom of 400 mV is required at the drains of M_8-M_{10} to ensure operation in saturation.

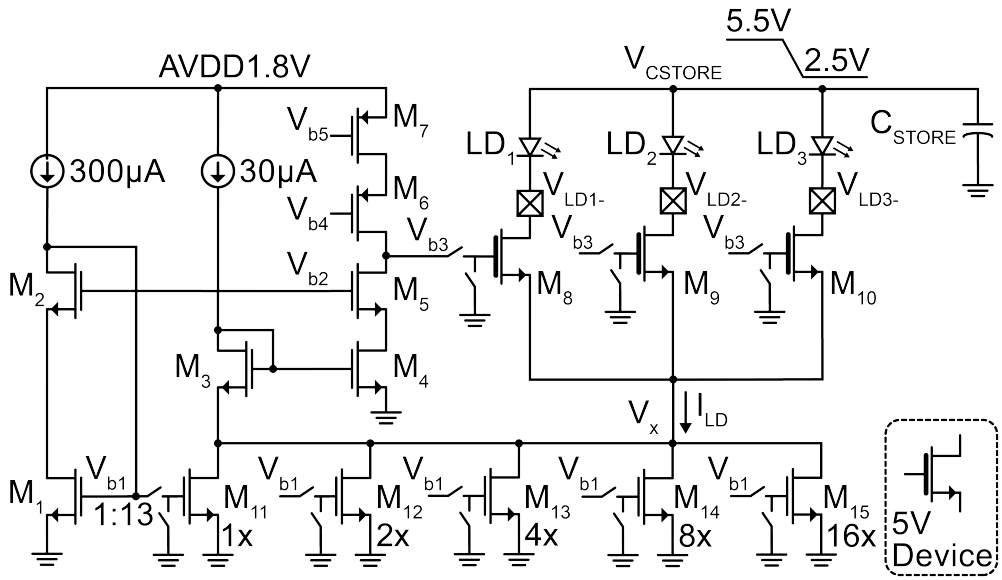

Figure 5.5: Schematic of the programmable 3-channel laser driver.

5.4 Imaging Frontend and Readout

The imaging frontend is similar to that presented in [33], but without the angle selective gratings (ASGs) as image deblurring is now provided by the FOP. The image sensor consists of a 36x40 array of pixels with a 44x44 μm^2 active photodiode area and a 55 μm pitch, covering a 2x2.2 mm^2 FoV. The pixel architecture, shown in Fig. 5.6(a), is based on a capacitive trans-impedance amplifier with C_{INT}=11 fF. To reduce low-frequency noise, reset

switch sampling noise, and pixel offset, a correlated double-sampling scheme is implemented with the following pixel timing (illustrated in Fig. 5.6(b)). First, the voltage on C_{INT} is zeroed out during the initial reset phase, T_{RST}, with timing configured in the *Set* T_{EXP} state. For the exposure time, T_{EXP}, the photocurrent is integrated on C_{INT} generating the pixel output voltage, $V_{OUT} = V_0 + I_{PD}.T_{EXP}/C_{INT}$, which is sampled on reset (C_R) and signal (C_S) sampling capacitors after intervals of 100 μs and T_{EXP}+100 μs, respectively. The final pixel value (V_{PIXEL}) is the difference between the signal (V_S) and reset (V_R) values.

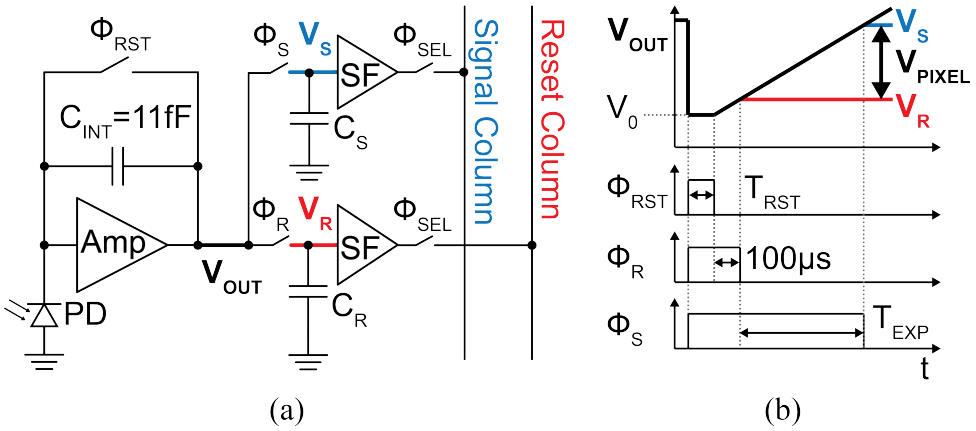

Figure 5.6: (a) Active pixel architecture with correlated double sampling. (b) Pixel timing diagram.

After Imaging, the analog pixel values are digitized and stored in memory during the *Readout* state. *Readout* duration is set to limit the leakage on the in-pixel sampling capacitors to less than an LSB. Therefore, the readout is performed in parallel across 4 channels each spanning 10-pixel columns. Each channel consists of an 8-bit differential SAR ADC driven by a buffer. The ADC has a dynamic range of 500 mV with an LSB of 1.95 mV, below the pixel readout noise (see chapter 6). The readout circuits operate on a 3.3 V supply to ensure sufficient headroom considering that the in-pixel source followers level shift the sampled pixel voltages up by 1 V. Thus, the size of C_{VCP} is chosen to maintain V_{CP} above 3.5 V throughout this state. The signal and reset pixel values are subtracted by the differential ADCs, and the digitized pixel values are stored immediately after conversion in a 11.52 kb latched-based memory. The schematic of the datapath for reading out one channel (=10 columns) of the pixel array and the architecture of a memory cell are shown in Fig. 5.7. Unlike the first work in chapter 4, this design enables a short *Readout* time of 5.4 ms, which is not limited by the longer *Backscattering* state (890 ms at 5 cm depth) that varies with depth.

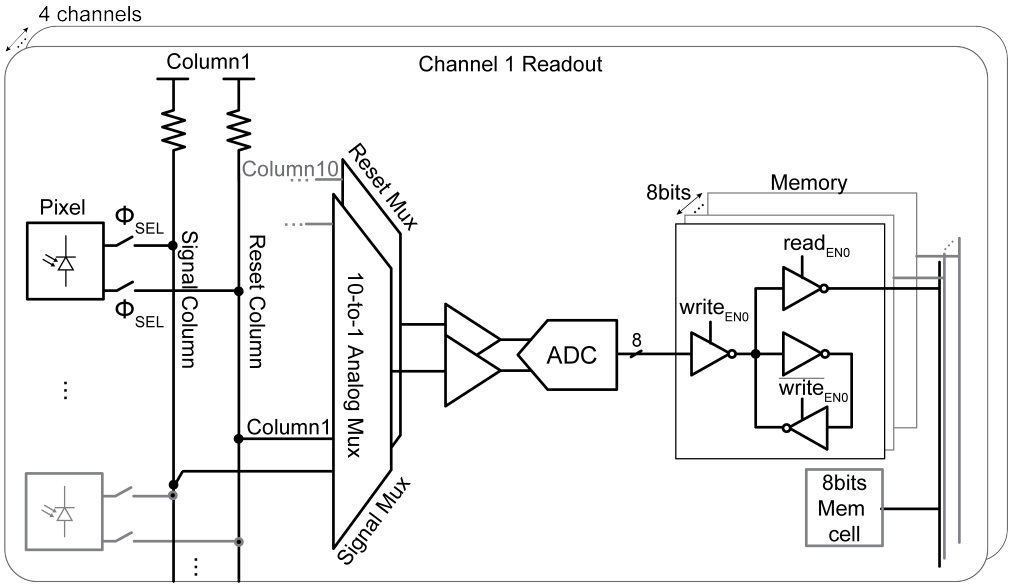

Figure 5.7: Readout data path of one of the channels of the pixel array

5.5 Data Transmission

During *Backscattering*, the memory is read serially (Φ_{MOD} in Fig. 5.1) and transmitted by modulating the amplitude of the reflected (backscattered) US pulses using a switch (S_{MOD} in Fig. 5.1). The uplink communication protocol is shown in the timing diagram in Fig. 5.3. The transmitted data for each pixel comprises a 9-bit packet containing a header (set to 0) followed by 8 data bits. The header pulse is necessary to impose a one-pulse delay to make sure memory is read and loaded into the serializer before data transmission. Additionally, setting the header to a known value of zero can help identify the backscattered bits. The external transducer generates a sequence of pulses each spanning a few cycles of the US carrier for the header and 8 individual bits. As shown in Fig. 5.8, after a time of flight (ToF=33 μs for 5 cm depth) the acoustic pulses reach the piezo and reflect with an amplitude proportional to the reflection coefficient of the piezo, Γ. Γ is a function of the impedance of the piezo, Z_{piezo}, at the operation frequency and is dependent on the electrical impedance loading the piezo, R_{load}, and therefore, can be controlled through the S_{MOD} switch. Near the parallel resonance frequency of the piezo, $\Gamma \propto R_{piezo}/(R_{Load}+R_{piezo})$, where R_{piezo} is the equivalent resistance of the piezo [67]. The switch impedance can be configured (hard-coded) by 2 bits to achieve minimum bit error rate (BER). After a second ToF, the backscattered signal is received by the external transducer and is demodulated to reconstruct the image. To avoid overlap of high voltage Tx and low voltage reflected Rx pulses, the external transducer transmits 2 bits within 2 ToFs and listens for the next 2 ToFs as shown in Fig. 5.3.

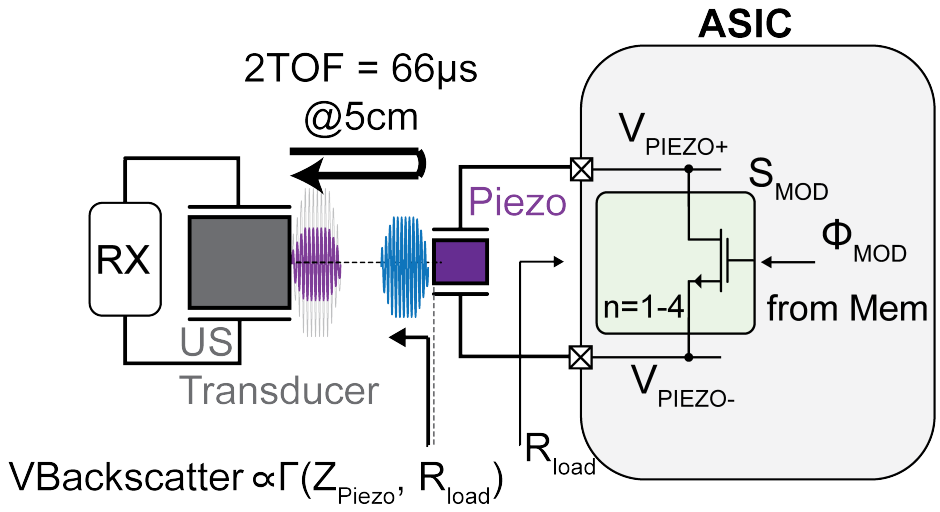

Figure 5.8: System diagram during *Backscattering*

5.6 Contributions

Some of the figures in this chapter are adapted from the following article:

1. **R. Rabbani***, M. Roschelle*, S. Gweon, R. Kumar, A. Vercruysse, N. W. Cho, M. H. Spitzer, A. M. Niknejad, V. M. Stojanovic, M. Anwar, "17.3 A Fully Wireless, Miniaturized, Multicolor Fluorescence Image Sensor Implant for Real-Time Monitoring in Cancer Therapy," *2024 IEEE International Solid-State Circuits Conference (ISSCC)*, San Francisco, CA, USA, 2024, pp. 318-320. (* Equally credited authors)

Acknowledgments: M. Roschelle and I contributed equally to the design of the second generation of the sensor and generating the figures presented in this chapter. S. Gweon assisted in designing various blocks including the redesign of the LDOs.

Chapter 6

Performance of the Multicolor Wireless Fluorescence Image Sensor

Fig. 6.1(a) shows the die photo of the chip. The IC measures 2.5x5 mm^2 and is fabricated in a TSMC 1.8/5/32 V 180 nm CMOS process. Fig. 6.1(b) shows the power breakdown for the chip where the laser driver dominates the power consumption. This section presents system-level measurement results for the wireless link, laser driver, and imaging frontend.

6.1 Measurement Setup

Fig. 6.2 shows the measurement setup for demonstrating fully wireless operation of the chip. In the acoustic setup, the piezo is submerged at a depth of 5 cm in a tank of canola oil. Canola oil has 0.075 dB/cm acoustic attenuation at 920 kHz and 1.34 MRayl acoustic impedance [68] similar to the impedance (1.4-1.67 MRayl) of tissue [44]. An external focused transducer (V314-SU-F1.90IN-PTF, Evident Scientific) at the surface of the tank transmits US signals to the piezo. To minimize interference from US reflections on data uplink, an acoustic absorber (Aptflex F28P, Precision Acoustics) is placed at the bottom of the tank. An FPGA (Opal Kelly XEM7010) generates the desired US pulse sequence as in Fig. 5.3 to control the chip. The timing of the pulse sequence is programmed through a custom user interface that interfaces with the FPGA. The waveforms are sent to a high-voltage transducer pulser board (Max14808, Maxim Integrated) to drive the external transducer accordingly.

The chip is directly connected with wires to the piezo for wireless power harvesting and data transfer via US. It is located inside a black box to reduce the background signal from ambient light during imaging. Slide-mounted samples are placed directly on top of the chip for imaging. The chip drives the μLDs, mounted on separate PCBs, to transilluminate the sample from above. It is important to note that *in vivo* the sample must be epi-illuminated between the sensor and the tissue. Epi-illumination can be accomplished by directing the laser light through a glass separator or light guide plate placed on top of the sensor [68, 83].

After taking an image, the backscattered US pulses are received by the external transducer

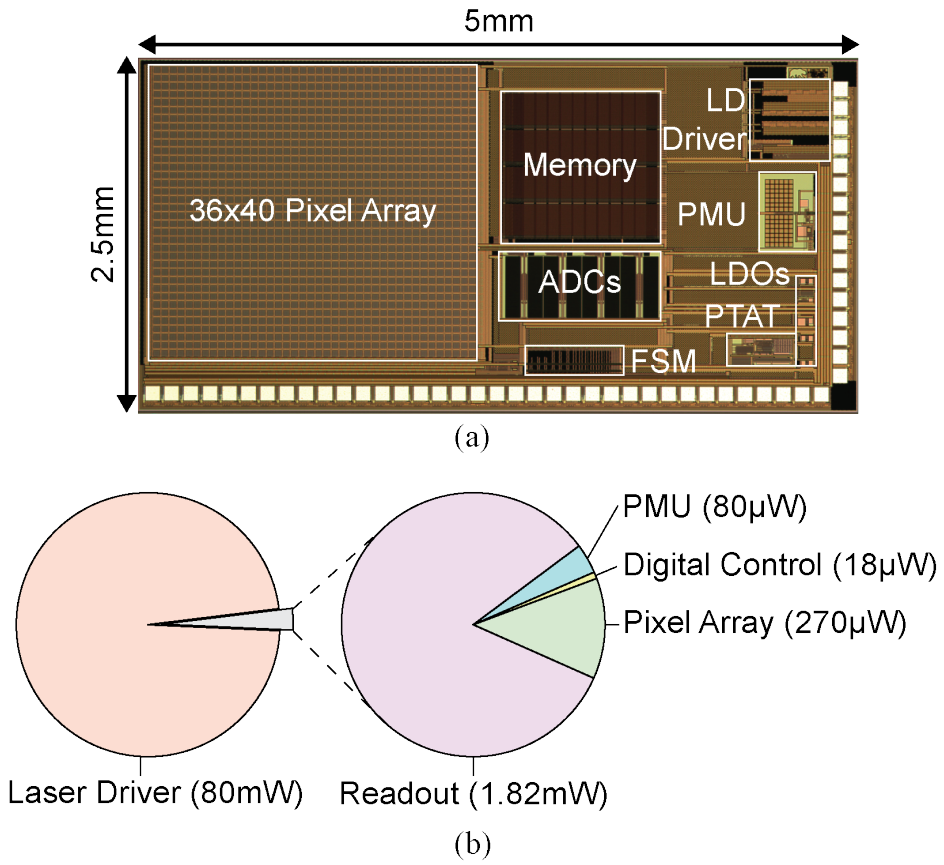

Figure 6.1: (a) Chip micrograph. (b) Breakdown of system power consumption.

and the data is captured on an oscilloscope for processing and demodulation. To remove the pixel-to-pixel DC offsets due to the photodiode dark current and mismatch in the readout circuitry, a dark image with the same integration time but with the laser off is subtracted from the final fluorescence image. The dark image is averaged to minimize its noise contribution.

6.2 Ultrasound Wireless Power Transfer

Fig. 6.3(a) shows the measured PMU waveforms (V_{Piezo}, V_{RECT}, V_{CP}, V_{CSTORE}), verifying wireless operation of the full system at 5 cm depth. In this measurement, the system operates with 221 mW/cm^2 of US power density which falls within 31% of FDA safety limits for US. Under this minimum required acoustic power condition, V_{CP} charges to 5.5 V in 50 s for the initial image. Charging time reduces to 35 s for consecutive frames with a nonzero initial V_{CP}. The Charge-Up time can be further reduced by increasing US power intensity, operating closer to the FDA limits.

Measured PMU waveforms during the *Imaging* and *Readout* states are presented in Fig.

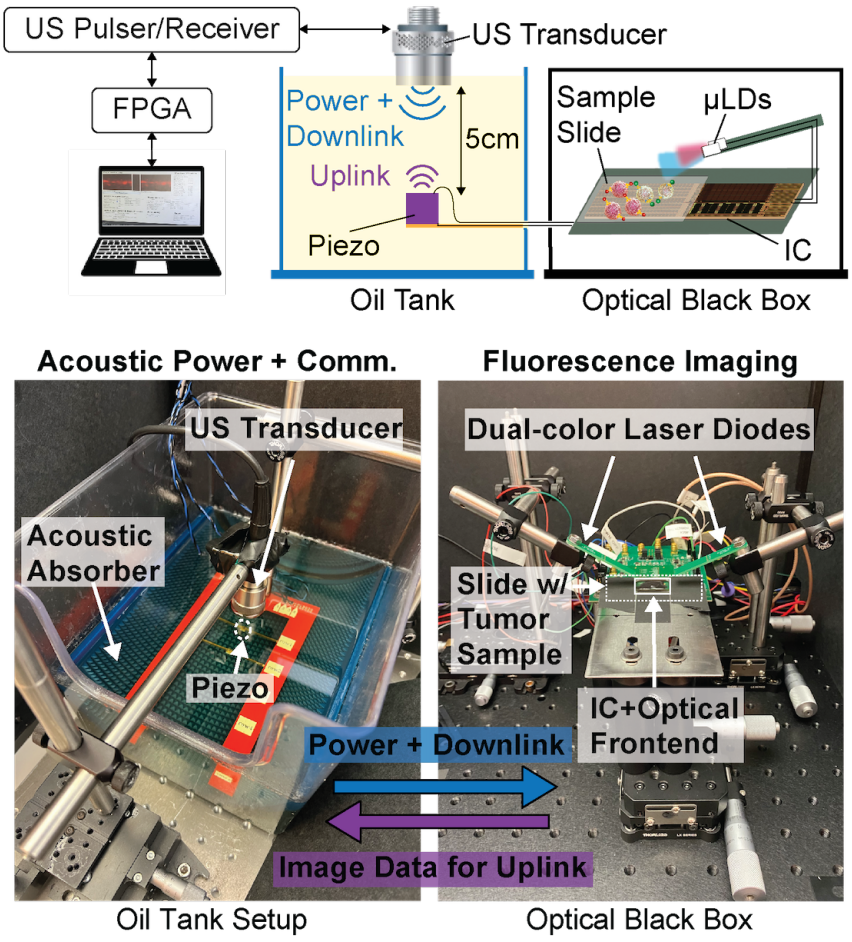

Figure 6.2: Acoustic and Imaging measurement setups for wireless imaging

6.3(b). During *Imaging* (T_{EXP}=8 ms), V_{CSTORE} drops from 5.5 V to 2.5 V while supplying the laser with I_{LD} = 37.5 mA from the energy stored in C_{STORE}. V_{CP} remains at 5.5 V throughout *Imaging* and drops to 3.5 V during Readout. Fig. 6.3(c) shows the measured waveforms while transmitting a single pixel data packet via backscattering. V_{piezo} is modulated according to the serial output of the memory (Φ_{MOD}) and the backscattered pulses are received by the external transducer ($V_{Backscatter}$ in Fig. 6.3(c). The one bits corresponding to a smaller load impedance appear larger in amplitude than the zero bits because the piezo is operated between series and parallel resonance frequencies for maximum voltage harvesting.

Fig. 6.4(a) shows the total acoustic power and acoustic power density (I_{SPTA}) incident on the piezo surface area at 5 cm depth for transverse offsets along the X or Y axis. Fig. 6.4(b) shows a similar measurement as the depth is adjusted along the z axis. The acoustic power density is measured with a hydrophone (HGL-1000, Onda) and it is integrated over the piezo area to measure the available acoustic power at the piezo surface. The measurement setup

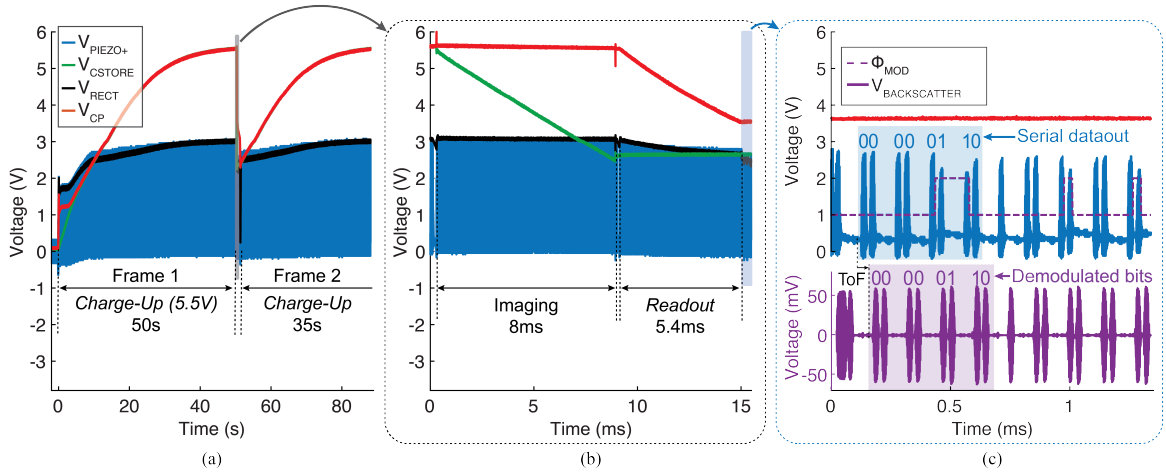

Figure 6.3: Measured power harvesting waveforms during (a) *Charge-Up*, (b) *Imaging* and *Readout*. (c) Measured backscatter waveforms.

inside a water tank is shown in Fig. 6.5. The hydrophone is fixed while the US transducer is transversed both along the depth and horizontal directions. The output of the hydrophone is connected to a pre-amplifier (AH-2010, Onda) to boost the signal by 20 dB. The output voltage of the pre-amplifier is linearly proportional to the measured acoustic pressure, with an overall gain of 7.37 mV/kPa. The spatial-peak time-average intensity (I_{SPTA}) of the acoustic field is an important safety parameter to estimate the temperature increase bound by 720 mW/cm^2 for diagnostic US applications according to FDA limits [84]. For both transverse and depth offsets, the power decreases as the piezo moves away from the focal point (near 5 cm depth) of the external transducer. The measured transverse and axial FWHMs for I_{SPTA} are 4.5 mm and 60 mm, respectively. In the future, misalignment loss can be reduced through dynamic focusing of the US with beam forming [85].

6.3 Energy Conversion Efficiency

Given that harvesting US energy and supplying the ASIC and the lasers are multiplexed in the time domain, we use energy efficiency to evaluate the US link. Electrical input energy is calculated by integrating the instantaneous electrical input power during *Charge-Up*. The output energy of the PMU is calculated by measuring the energy stored in the C_{STORE} and C_{VCP} and the energy consumption of the ASIC during *Charge-Up*.

The static current consumption of the chip, I_{DC}, is determined in DC mode by measuring the DC current of a precision measurement unit (B2912A, Keysight) externally supplying V_{CP} from 0 to 5.5 V. Multiplying I_{DC} by V_{CP} results in the static power consumption of the ASIC. The energy stored in C_{STORE} and C_{VCP} is measured from $\frac{1}{2}(C_{STORE} + C_{VCP})V_{CP}^2$. A summary of the derivation of power and energy components and the corresponding efficiencies

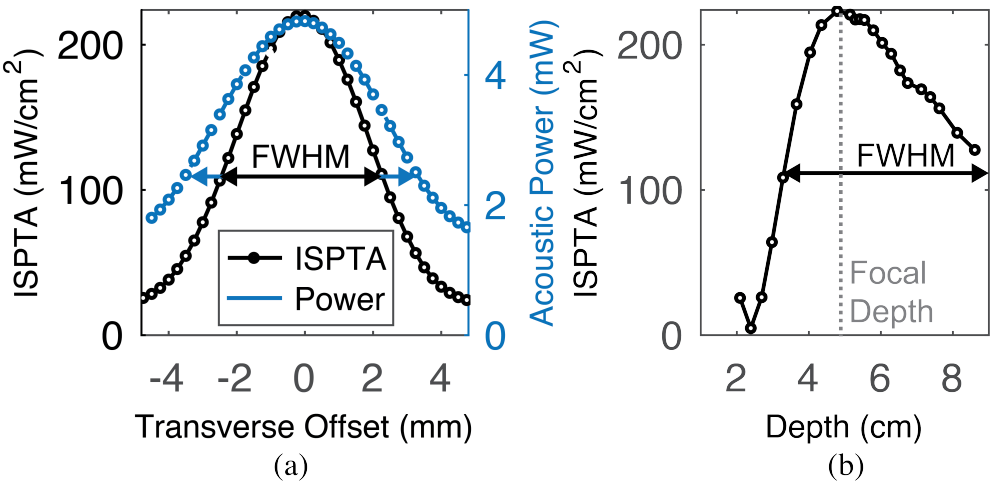

Figure 6.4: Harvested acoustic power vs. (a) transverse offset and (b) depth.

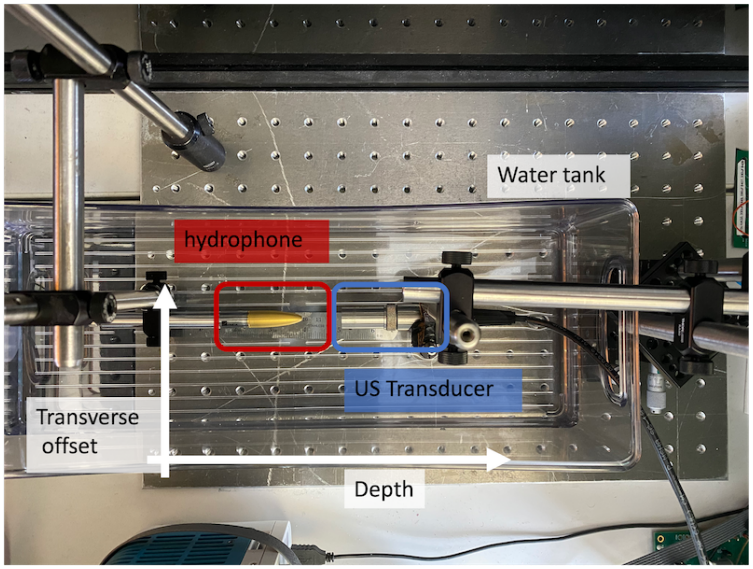

Figure 6.5: Experimental setup for measuring acoustic power density.

and the corresponding circuit model are included in Fig. 6.6.

While charging V_{CP} from 0–5.5 V, the overall energy efficiency of the PMU is shown in Fig. 6.7. The electrical energy conversion efficiency is 12.7%. The efficiency of the system in converting the available acoustic energy on the face of the piezo to the electrical output energy of the PMU is 3.3%. The input acoustic energy is calculated by integrating the measured acoustic power density at the surface of the piezo (Fig. 6.4(a)) throughout this same period. The acoustic to electrical conversion efficiency of the piezo is 26%.

Power	Energy
$P_{input} = V_{AC}.I_{input}$	$E_{input} = \int P_{input}$
$P_{static} = V_{CP}.I_{DC}$	$E_{static} = \int P_{static}$
$P_{store} = \frac{dE_{Cstore}}{dt} = C_{Tot}V_{CP}\frac{dV_{CP}}{dt}$	$E_{store} = \frac{1}{2}C_{Tot}V_{CP}^2$
$\eta_P = \frac{P_{output}}{P_{input}} = \frac{P_{static}+P_{store}}{P_{input}}$	$\eta_E = \frac{E_{output}}{E_{input}} = \frac{E_{static}+E_{store}}{E_{input}}$

(a)

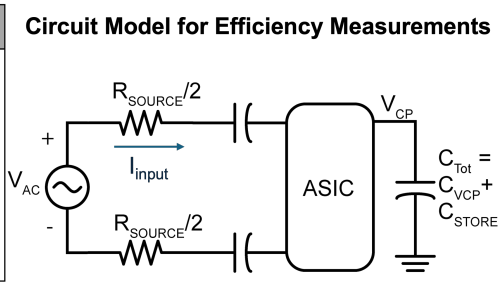

(b)

Figure 6.6: (a) Power, energy and conversion efficiency equations. (b) Circuit model for measuring conversion efficiency

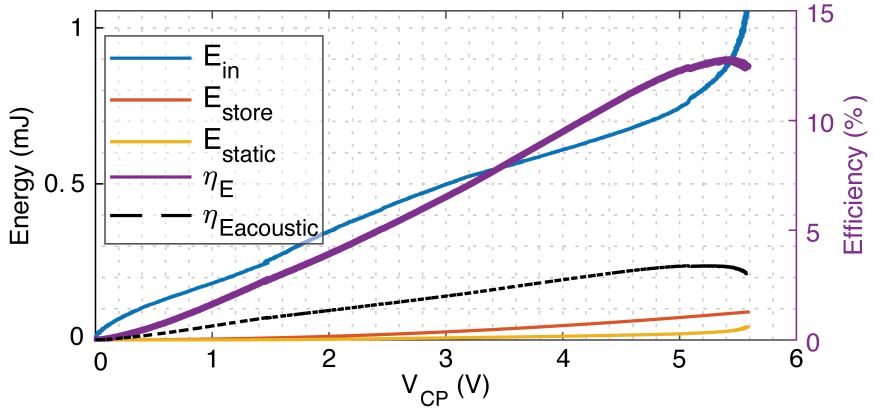

Figure 6.7: Energy conversion efficiency while charging V_{CP} from 0–5.5 V

6.4 Laser Driver

Fig. 6.8 shows measurements of the laser driver and PTAT. The output current of the laser driver (I_{LD}) is measured with a precision measurement unit (B2912A, Keysight). The measured I_{LD} across all DAC codes is shown in Fig. 6.8(a). Fig. 6.8(b) shows the percent change in I_{LD} as the output voltage of the laser driver, V_{LD-}, drops from 3.5–0.4 V. This range corresponds to the output voltage of the laser driver (connected to laser cathode, V_{LD-}) for a 5.5-3.5 V drop on V_{CP} accounting for the 2 V forward bias voltage of the 650 nm μLD. For DAC code=5 (I_{LD}=20 mA), there is less than 1% variation across the 3.1 V. drop. These results are an improvement over chapter 4 where the reference current varied 11.5% over a 1.5 V drop, resulting in a 50% reduction in the laser output power.

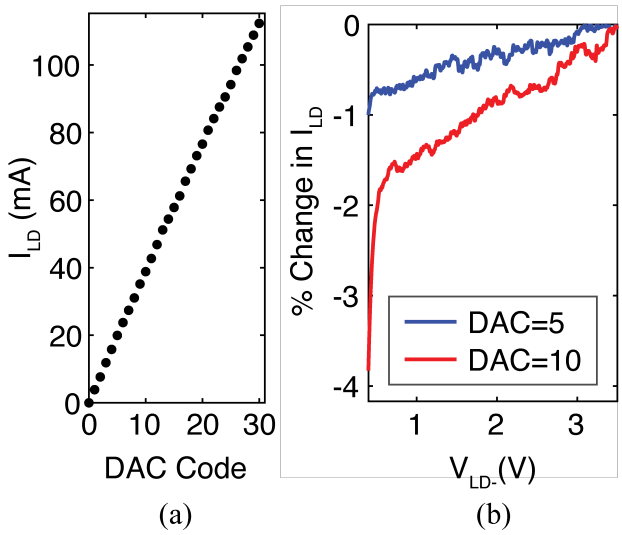

Figure 6.8: Measurements of (a) laser driver current vs. DAC code, (b) laser driver output current vs. driver voltage.

6.5 Ultrasound Data Uplink

At 5 cm depth, transmission of one image (11.52 kb) takes 890 ms, resulting in a data rate of 13 kbps. The received backscattered waveform is processed and demodulated to reconstruct the image as follows. First, the signal is bandpass filtered at the carrier frequency, windowed to select the bit intervals and then reconstructed with sinc interpolation. The peak-to-peak amplitude is measured for each pulse and compared with a predetermined threshold to predict the bit value. The serial output of the chip serves as the ground truth. Fig. 6.9 shows a histogram of the backscattered signal amplitude for each bit normalized to the threshold amplitude, demonstrating a clear separation between one and zero bits. The measurement shows robust error-free transmission of 90 frames including a combination of dark frames and images taken with the 650 nm and 455 nm lasers. The bimodal nature of the histogram results from combining data across different imaging conditions in the same histogram and differing interference from the transmission on the two received pulses within each interval of 2ToFs. The device archives a bit error rate (BER) better than 10^{-6} (0 out of 1,036,800 bits). The average modulation index is 5.6%.

6.6 Imaging Frontend

The photodiode responsivity is determined by measuring pixel output voltage across a range of incident optical powers as shown in Fig. 6.10(a). We use a LED with a collimator and beam expander to ensure uniform illumination of the sensor. A narrow bandpass interference filter placed in front of the LED selects a specific wavelength. Measurements are made at

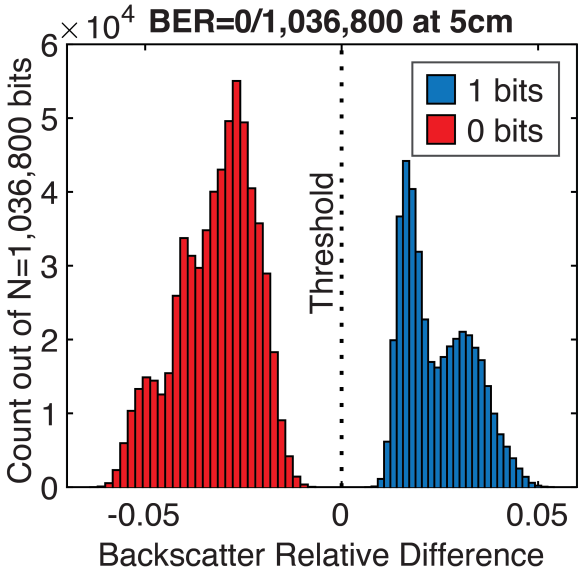

Figure 6.9: Histogram of bits with a measured bit error rate (BER)$< 10^{-6}$ at 5 cm depth in oil.

535 nm and 705 nm, near the center of the optical frontend passbands. The optical power output of the LED is characterized with a power meter (PM100D, ThorLabs). In Fig. 6.10(a), the slope indicates pixel gain in mV/pW with T_{EXP}=8 ms. The photodiode responsivity is calculated by dividing pixel gain by the transimpedance gain of the CTIA. The pixels have a mean responsivity of 0.13 A/W (quantum efficiency (QE)=30%) and 0.21 A/W (QE=37%), at 535 nm and 705 nm respectively. A histogram of the measured dark current across pixels with a Gaussian fit is shown in Fig. 6.10(b). The mean dark current is 14.9 fA (7.7 aA/μm^2) with a standard deviation of 0.7 fA (0.4 aA/μm^2). Fig. 6.10(c) shows the measured pixel output noise in dark condition for different exposure times for a single frame and an average of 8 frames. The output noise increases with the exposure time due to the shot noise from the increased dark signal.

The resolution of the imager is measured with a negative standard USAF target (Fig. 6.11(a)) overlaying a uniform layer of Cy5 NHS Ester (λ_{EX} = 649 nm, λ_{EM} = 670 nm) dissolved in PBS at 10 μM concentration. The dye is contained with a 150 μm-thick glass coverslip and the target is placed on the imager. The resolution measurements were conducted with wired power and data transfer and using a fiber-coupled 650 nm laser for uniform illumination. Fig. 6.11(b) shows the sensor image of the element with 125 μm line spacings compared to the microscope reference image in Fig. 6.11(c). The sensor images this element at 50% contrast as calculated with the line scan in Fig. 6.11(d). Contrast is calculated as (V_{max} - V_{min})/(V_{max} + V_{min} - V_{bk}), where V_{max} and V_{min} are the maximum and minimum pixel values in the bright and dark bars, respectively, and V_{bk} is the background

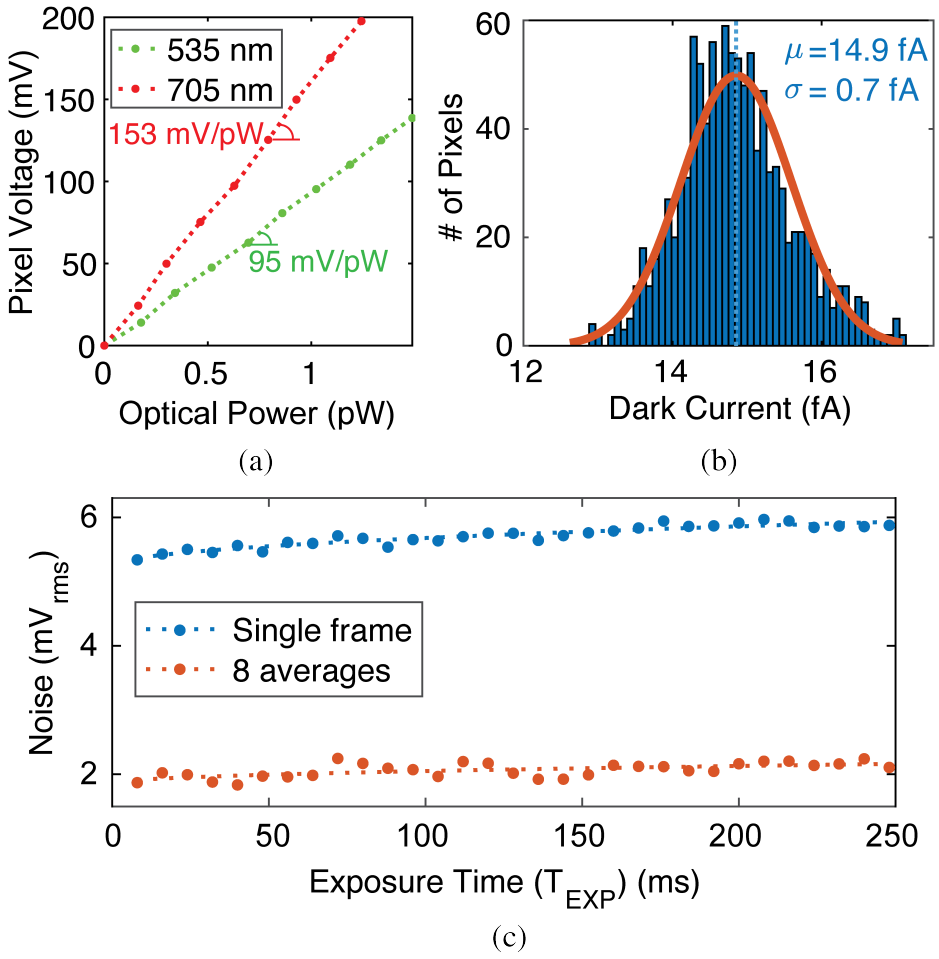

Figure 6.10: (a) Pixel output voltage vs. incident optical power. (b) Histogram of measured dark current across pixels. (c) Measured pixel noise under dark condition without averaging and after 8 averages.

signal. Fig. 6.11(e) shows the full contrast transfer function measured by imaging elements on the target with line spacings ranging from 79-455 μm and calculating the contrast for each. These results demonstrate that with the FOP, the imager can distinguish line spacings as small as 100 μm with greater than 20% contrast.

6.7 3-color Fluorescence Imaging

To demonstrate three-color imaging, we image a sample containing 15 μm-diameter green ($\lambda_{EX} = 505\ nm$, $\lambda_{EM} = 515\ nm$, F8844, Thermo Fisher Scientific), red ($\lambda_{EX} =$

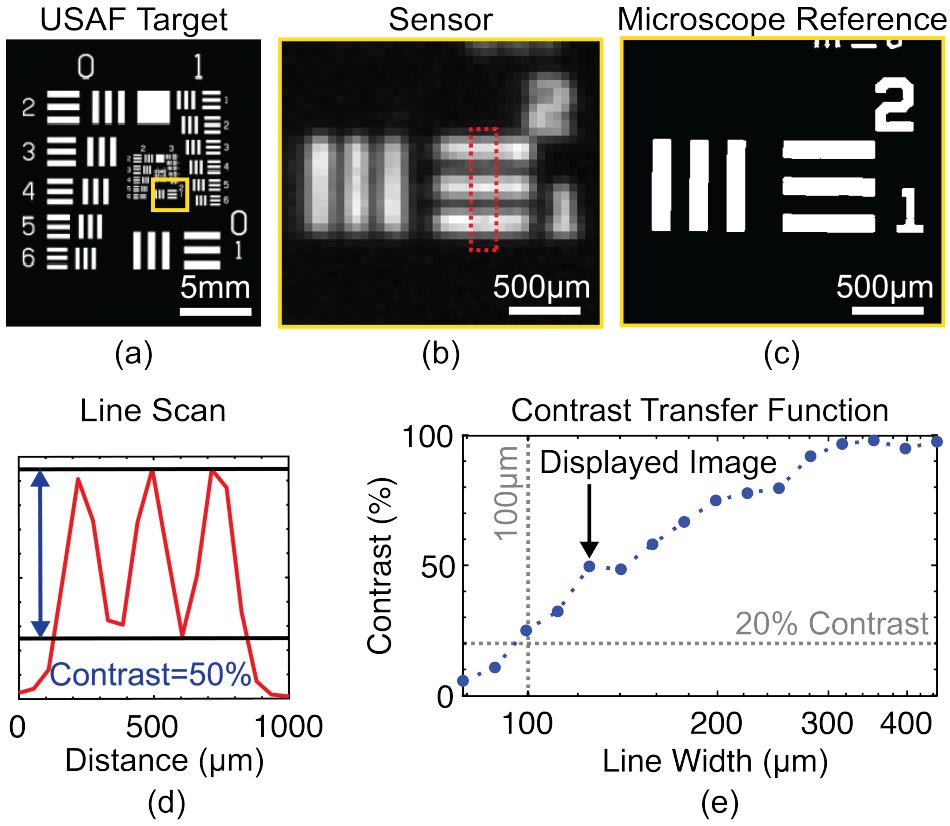

Figure 6.11: Resolution measurements using (a) USAF target. Image of element with 125 μm line width with the sensor (b) and a microscope (c). (d) Line scan of image in (a). (e) Measured contrast transfer function.

745 nm, $\lambda_{EM} = 680\ nm$, F8843, Thermo Fisher Scientific), and NIR ($\lambda_{EX} = 780\ nm, \lambda_{EM} = 820\ nm$, DNQ-L069, CD Bioparticles) fluorescent beads. The beads are suspended in 1x PBS solution at a concentration of approximately 10 beads/μL. 50 μL of solution is pipetted into a micro-well chamber slide for imaging. Imaging results are shown in Fig. 6.12. The sensor images are obtained wirelessly with I_{LD}=18.5 mA, $T_{EXP,GREEN}$=8 ms, $T_{EXP,RED}$=16 ms, $T_{EXP,NIR}$=8 ms. For each color channel, 4 frames are averaged and the channels are colored and overlaid to make the multicolor image. The sensor images correspond well to a reference image taken with a benchtop fluorescence microscope (Leica DM-IRB). A few beads do not appear in the sensor image due to non-uniform illumination from the μLDs. There is also a line artifact visible in the NIR channel due to reflections off the wire-bonds and can be mitigated by as detailed in [47].

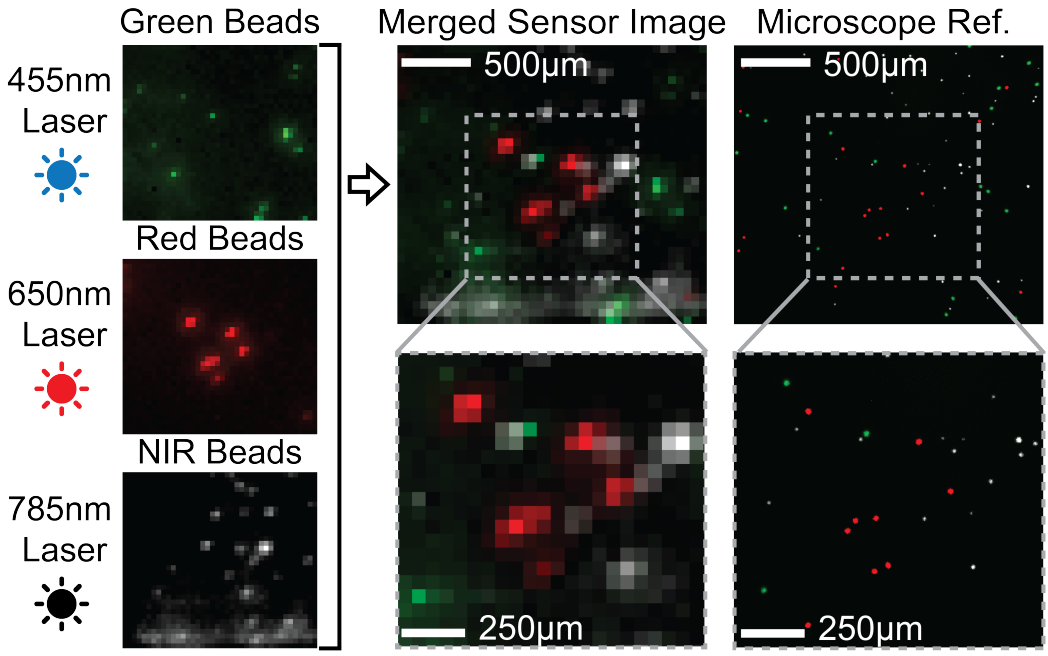

Figure 6.12: 3-color imaging of green, red and NIR fluorescent beads.

6.8 *Ex Vivo* Imaging of Immune Response

We conducted an *ex vivo* mouse experiment to demonstrate the application of our sensor to assessing the response to cancer immunotherapy through dual-color fluorescence imaging of both effector and suppressor cells in the tumor microenvironment. In this study, we measured response to immune checkpoint inhibitors (ICIs), a common type of immunotherapy that activates the immune system against cancer by blocking inhibitory interactions between immune and cancer cells [79, 78]. A successful immune response to ICIs requires the activation and proliferation of CD8+ T-cells, the most powerful effectors in the anticancer response, into the tumor microenvironment [86]. Therefore, CD8+ T-cell infiltration has been identified as an indicator of a favorable immune response [87]. However, CD8+ T-cell activation can be inhibited by suppressor immune cells such as neutrophils, which regulate the immune system and inflammation in the body and are associated with resistance to ICI immunotherapy [88, 89]. Dual-color fluorescence imaging enables differential measurement of the two control mechanisms of the immune response with the same imaging frontend which is not possible with clinical imaging modalities such as MRI, PET, or CT.

Ex Vivo Experiment Design

Figure 6.13 outlines the *ex vivo* experiment design, which uses two engineered cancer models from [67], an LLC breast cancer model (engineered to resist ICIs) and a B16F10 melanoma model (engineered to respond to ICIs). Both tumor models show increased CD8+

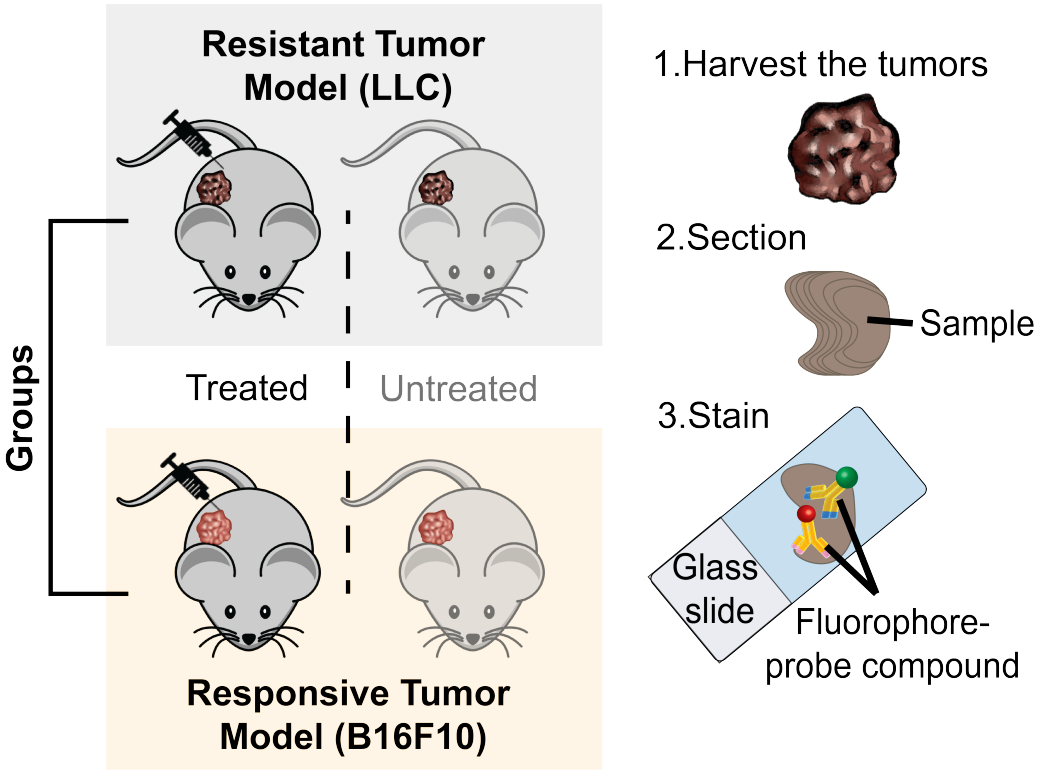

Figure 6.13: Experimental design for the *ex vivo* mouse experiment.

T-cell infiltration over the course of treatment. However, while the B16F10 tumors reliably respond, the LLC tumors are resistant to ICI therapy. This resistance has been linked to a T-cell-driven inflammatory response that triggers an influx of neutrophils into the tumor, suppressing T-cell activation [90]. The experiment includes two groups of mice each bearing one type of tumor. Each group consists of a mouse treated with ICI and an untreated mouse injected with non-therapeutic antibody for control. 2 weeks after the onset of treatment, the tumors are harvested, sectioned to 4 μm-thick samples, and mounted on glass slides. Two adjacent sections from each tumor are labeled separately with fluorescent probes targeting CD8+ T-cells and neutrophils. CD8+ T-cells are stained with a CD8a antibody labeled with Cy5 ($\lambda_{EX} = 649\ nm, \lambda_{EM} = 670\ nm$) and neutrophils are stained with a CD11b antibody labeled with FAM ($\lambda_{EX} = 492\ nm, \lambda_{EM} = 518\ nm$).

Ex Vivo Imaging Results

Images of the tumor samples are captured wirelessly with the sensor and compared with reference images from a benchtop fluorescence microscope. Figs. 6.14(a) and 6.14(b) show the imaging results from the LLC (resistant) and B16F10 (responsive) groups, respectively. For each fluorescent channel, 8 frames are acquired with the chip, using imaging parameters

of I_{LD}=18.5 mA, $T_{EXP,Cy5}$=16 ms, and $T_{EXP,FAM}$=8 ms. The sensor images are averaged across all frames. The microscope images are overlaid with the cell nuclei of the entire sample, stained with DAPI (blue in the image) to highlight the tumor area. The white lines within the images indicate the boundaries of the tumor tissue. The sensor images are qualitatively consistent with the microscope references, albeit at a lower resolution and with varying intensity across the image due to non-uniform illumination from the μLDs.

To quantify the results for each tumor model, the percent change in the density of both cell types between the untreated and treated mice is calculated according to the metrics in Fig. 6.15(b). Ground truth cell densities are determined using the microscope images by counting the fraction of cell nuclei (DAPI) labeled with the targeted probe (red and green channel). As the sensor does not have single-cell resolution, the cell density in the sensor images is determined by the fluorescence intensity in the tumor normalized by the area bounded by the dashed white lines in Fig. 6.14(a-b). The background signal is mostly canceled out by measuring percent change.

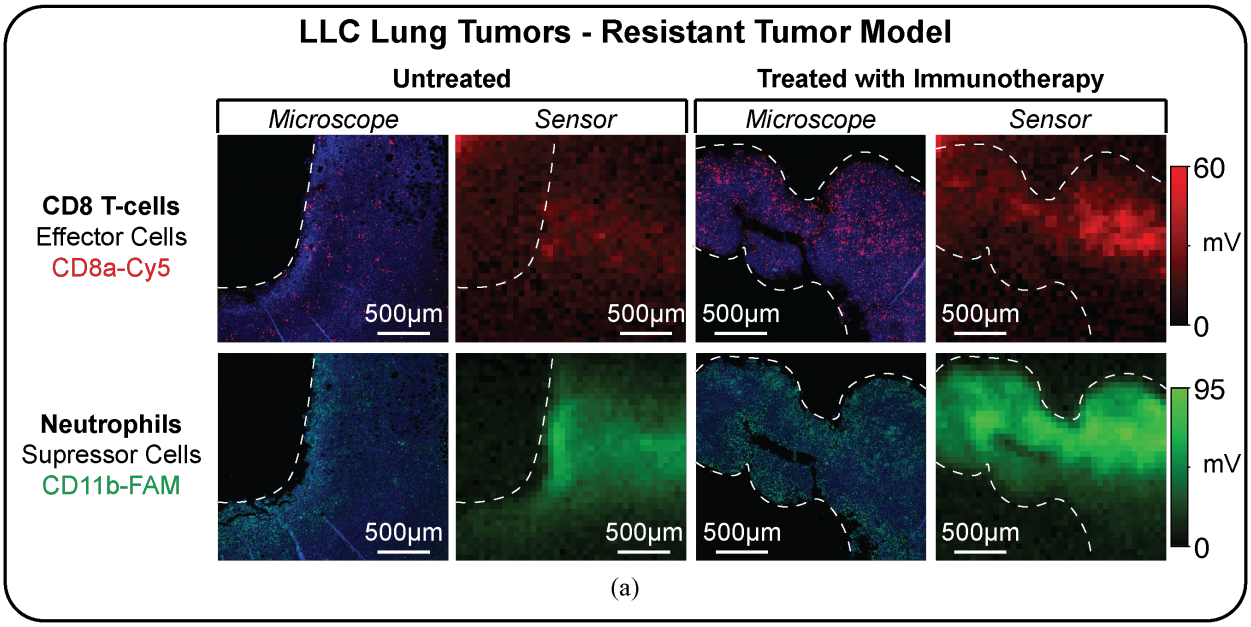

Figure 6.14: *Ex vivo* imaging of mouse tumors with and without immunotherapy. Imaging results for (a) the resistant tumor model (LLC) and (b) the responsive model

The quantified results from the sensor and microscope are shown in Fig. 6.15(a). The sensor captures the general trends observed with the microscope, corresponding with the results in [90]. The notable increase in the density of CD8+ T-cells in both B16F10 samples (sensor: 847%, microscope: 582%) and the LLC samples (sensor: 38%, microscope: 191%) suggests a response to immunotherapy in both models. However, a larger increase in CD11b

density after treatment in the LLC tumors (sensor: 66%, microscope: 75%) over the B16F10 tumors (sensor: 42%, microscope: 51%), suggests resistance in the LLC model due an increase in neutrophils. These trends would better reflect the results in [90] with a larger sample size to account for heterogeneity across the mice and neutrophil-specific biomarkers. However, these results highlight the utility of multicolor fluorescence imaging in evaluating the response to cancer immunotherapy, enabling a differential measurement of both effector (e.g. CD8+ T-cell) and suppressor (e.g. neutrophil) populations. As shown by the increase in CD8+ T-cells in resistant LLC tumors, an increase in effector populations does not always correlate with response as the effector cells may not be activated. Therefore, simultaneously imaging of suppressor populations (e.g. neutrophils) has two advantages: (1) enabling a more accurate assessment of response and (2) revealing the mechanisms of resistance (e.g. neutrophil interference with CD8+ T-cells) that can be targeted with second-line therapies (e.g. blocking neutrophil-T-cell signaling as done in [90]).

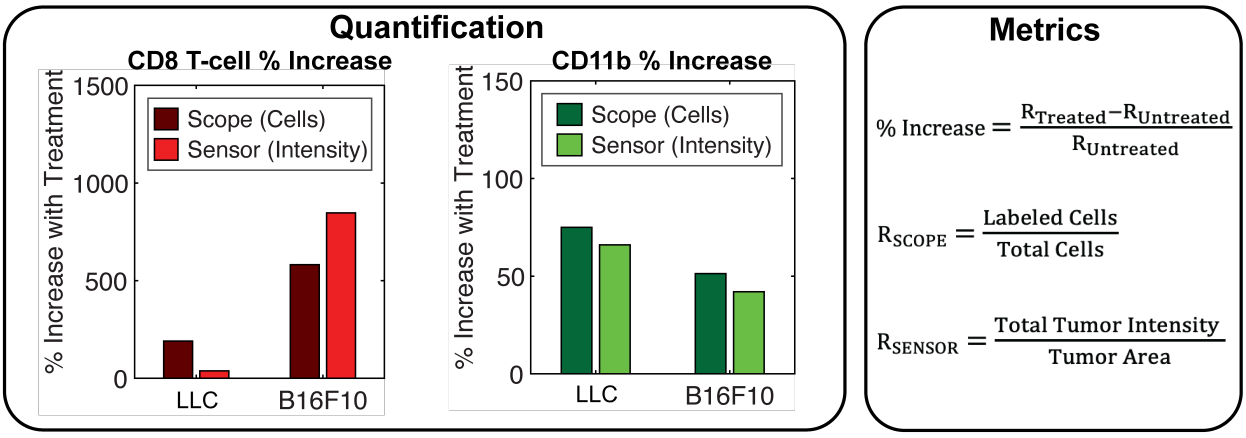

(a) (b)

Figure 6.15: Quantification of the *ex vivo* images. (a) Quantified results. (b) Metrics for quantification of cell populations.

6.9 Contributions

Some of the figures in this chapter are adapted from the following article:

1. **R. Rabbani***, M. Roschelle*, S. Gweon, R. Kumar, A. Vercruysse, N. W. Cho, M. H. Spitzer, A. M. Niknejad, V. M. Stojanovic, M. Anwar, "17.3 A Fully Wireless, Miniaturized, Multicolor Fluorescence Image Sensor Implant for Real-Time Monitoring in Cancer Therapy," *2024 IEEE International Solid-State Circuits Conference (ISSCC)*, San Francisco, CA, USA, 2024, pp. 318-320. (* Equally credited authors)

Acknowledgments: M. Roschelle and I contributed equally to testing the second generation of the sensor and generating the figures in this chapter. S. Gweon and R. Kumar assisted with the design of the test setup. M. Roschelle contributed to the design of the *ex vivo* experiments conducted in collaboration with N. W. Cho, Prof. M. H. Spitzer.

Chapter 7

3D Reconstruction from 2D Images via Deep Learning

The presented lensless image sensors are specifically designed to capture 2D images of the samples within their field of view, in close proximity to their surface. These images contain critical information about the immune responses crucial for both diagnosing cancer and guiding treatment. However, visualizing the 3D location of fluorescently labeled cells *in vivo* is necessary in order to determine the location of cell clusters harbored in sites farther from the imager.

Existing imaging platforms are able to obtain this information intraoperatively during surgery, as described in [91, 92, 93], but they are impractical for minimally invasive monitoring procedures, particularly in the context of complex and hard-to-reach tumors. These bulky instruments rely on large optics and lenses to achieve high resolution, making them unsuitable for miniaturization due to their inherent rigid optical components. Therefore, they are ill-suited for real-time monitoring of treatment response in implantable settings. Consequently, a high precision imaging platform with a smaller form factor is necessary.

Miniaturized imagers face challenges in achieving high resolutions comparable to their larger counterparts. Shrinking the size of the imager imposes limitations on the size of optical filters and focusing lenses, thereby compromising their performance and image resolution. Moreover, wirelessly supplying the illumination from the laser diodes restricts the total photon budget within the system, further limiting the performance of *in vivo* fluorescence microscopy. To achieve reliable 3D information using such small form-factor devices, enhanced custom optical filters and lenses are necessary to match the performance of larger instruments. However, manufacturing such components is often challenging, and image quality remains sub-optimal compared to benchtop microscopes. Therefore, computational techniques capable of enhancing images from small form-factor devices are required.

Miniaturization of these platforms into electronic micro-imagers, as exemplified in [33, 50, 56], enables their placement in hard-to-reach regions, allowing for the visualization of microscopic diseases intraoperatively in cavities several millimeters deep. Moreover, these micro-imagers facilitate real-time monitoring of cell dynamics and treatment assessment *in*

vivo, aided by a network of wirelessly powered implants. Figs. 7.1(a) and (b) illustrate how micro-imagers offer comprehensive visualization of tumors without disrupting the flow of operation or treatment, for intraoperative and implantable applications, respectively. In intraoperative imaging, multiple image acquisitions from different angles can be obtained by scanning the tumor bed with a surgical fiducial, as shown in Fig. 7.1(a). Similarly, a network of implantable imagers can capture images from different angles of the target, as depicted in Fig. 7.1(b).

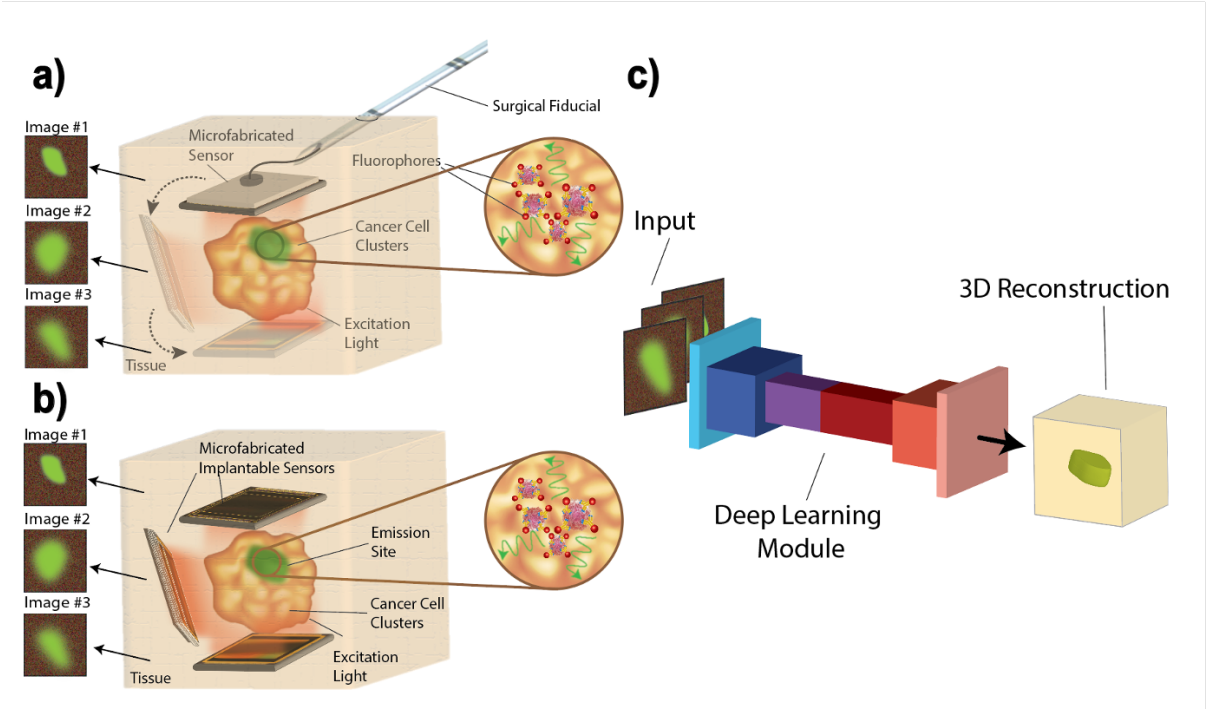

Figure 7.1: Concept of multiple visualization of the tumor using micro-imagers: (a) Multiple images taken by rotating the micro-imager attached to a surgical fiducial intraoperatively. (b) Network of implantable micro-imagers to capture multiple fields of view. (c) Combination of neural networks and micro-imagers enabling 3D visualization and resolution enhancement.

7.1 Convectional Image Processing for Customized Imager

Conventional image processing techniques involve deconvolution, surface projection algorithms and noise enhancement methods. These methods rely on a linear transformation of the image, based solely on raw image data and the point spread function (PSF) of the imaging device, without prior knowledge of the target. The PSF, also known as the transfer function

of the imaging system in spatial domain, describes the response of an imaging system to a point source of illumination [94] and is crucial in linear image formation processes such as fluorescence imaging. The image is a superposition of the convolution of each point source with the PSF. Therefore, the target can be retrieved by deconvolving the image with PSF of the imager.

However, deconvolution methods require calibration for each depth, limiting processing speed and posing challenges for images with overlaid cell foci from different depths. Moreover, the PSF, as a low pass transfer function, removes high-frequency components, leading to a loss of sharpness in the recovered image. Additionally, applying inverse PSF amplifies high frequency noise degrading recovery of the original image. Similar to deconvolution, other linear image processing technique will suffer from similar issues.

To overcome these limitations, a non-linear post-acquisition processing deep learning model, capable of incorporating physiological and spatial information is proposed to enhance the resolution of micro-imager images and provide insights into cell positions in 3D.

Deep learning emerges as a promising approach, combining multiple layers of non-linear transformations to create powerful processing modules capable of complex tasks such as image enhancement, image classification and feature extraction. Yin et al. [95] investigated characteristics of neuronal networks by extracting neuronal culture cluster information from microscopic images of neurons using machine learning models, and Chen et al. [96] were successfully able to demonstrate label-free tumor cell classification using images of flow cytometry. Deep learning allows breaking the tradeoffs of fluorescence imaging and using the computational models to augment hardware complexity and improve upon optical limits, by using a large collection of training data to build the network [97]. By employing adaptive network architectures like residual neural networks (ResNets [98]) and convolutional neural networks (CNNs [99]), this chapter introduces several cancer imaging applications utilizing deep learning to enhance the resolution and capability of custom-made micro-imagers. Fig. 7.1(c) illustrates how the combination of neural networks and micro-imagers can restore image sharpness and resolution and create 3D visualizations of specimens without the need to modify the image sensor.

This chapter presents modules capable of cell presence detection within each layer of the sample in 3D stacks based on the work in [100]. This model introduces an innovative imaging approach utilizing two sensors to capture tissue from different angles. This enables three-dimensional imaging of the sample, offering insights into the spatial distribution of cells within the sample.

7.2 Dataset Synthesis

A training dataset is critical for using a neural network in 3D cellular imaging of tissue is. Training deep neural networks necessitates access to an extensive collection of training data derived from the tumor microenvironment, tailored to each specific application. The impracticality of obtaining a large dataset, taken at varying depths, from tissue motivates

synthesis of a diverse dataset of tumor cell images based on the morphology of real-life tissue samples, to leverage prior knowledge of the tumor cells. To address this, a synthetic and diverse dataset of tumor cell images based on prior knowledge of morphological characteristics of real-life tissue samples is needed.

The synthesis method must be programmable to facilitate the generation of a large dataset by randomly selecting parameters. These parameters lead to images that accurately represent cell foci, thus ensuring the dataset's diversity and accuracy.

To tackle this challenge, this section introduces a methodology for generating a substantial training dataset that mirrors real-life specimens, such as a single layer of cells on a slide, building on prior work [76]. To simulate the 3D structure of a tumor, we generate stacks comprising multiple layers of cells spaced 250 μm apart, within 1 mm from the sensor. Given that the lensless custom imager is optimized for contact imaging of cell clusters, we set 1 mm as the boundary for proof of concept demonstration.

To generate images resembling real-life cell foci, we incorporate a coherent gradient noise generation technique known as Perlin noise [101]. Perlin noise is commonly used to create natural-looking textures, such as marble, wood, and cloud textures for motion picture visual effects [102].

We generate a binary matrix representing a tumor mask, with high values ($>$0.5) indicating tumor areas and low values ($<$0.5) representing non-cancerous background to pinpoint the tumor cell foci. Leveraging the inherent structure of Perlin noise, we achieve a smooth cellular location map filled with signal and background intensity values. Once the cell foci's locations are determined using the tumor mask, we render a tumor image by assigning in-pixel signal and background intensity values based on the mean and variance of real tumor images. To ensure a close correlation with real images, we verify that the statistical parameters originate from a representative range of parameters obtained from real data signal-to-noise ratio (SNR) calculations, demonstrated in [76].

We select an image sensor with a 51$\times$51 array of pixels, assuming a pixel architecture similar to the lensless chip-scale CMOS imager designed for *in vivo* intraoperative cancer imaging [33].

7.3 Deep Learning Model for Depth Estimation

This section introduces a nonlinear model to localize cells from various overlapping and non-overlapping tissue layers and identify their corresponding depths. Leveraging machine learning models for multi-layer depth estimation offers a key advantage in distinguishing dim cell clusters near the imager's surface from brighter cellular responses further away, otherwise challenging without further processing. Achieving multi-layer cell detection from a single 2D image from the customized image sensor with a precision better than 500 μm equips surgeons with sufficient resolution to scan the tumor bed thoroughly.

Multi-level depth information from planar images of our lensless microscope on-chip eliminates the need for bulky optical lenses [103, 104, 105]. This section presents separate

modules for detecting non-overlapping and overlapping multi-layer clusters of cancer cells.

To create the training dataset for non-overlapping cell stacks, pairs of synthesized cell images from two different depth values are randomly selected within the 0 to 1 mm range, with a minimum difference of 500 μm between the adjacent layers. Individual cell images from each layer are convolved with the PSF of the custom-made imager and merged together to form a multi-layer image, with overlapping regions subtracted to separate cell distributions from each layer.

In addition to detecting cells in isolated multi-layer clusters, we explore extracting 3D information from a more complex structure involving overlapping cell stacks. However, the accuracy of recovering 3D information using a single micro-imager is significantly limited when extracting spatial information from distant layers due to attenuation of the optical signal reaching the sensor and PSF non-ideality.

To address this limitation, we add a second sensor to the imaging system, facilitated by the ultra-small form factor of the sensor itself, enabling implantation and surgical practicality. For this experiments, the two sensors are positioned 1 mm apart on both sides of the synthesized three-dimensional tissue.

Both the single and dual-sensor modules comprise a 6-layer CNN (3 convolution and 3 deconvolution layers), with their outputs consisting of 4 binary input-sized layers indicating cell presence in each, where (>0.5) indicates cell presence and (<0.5) indicates absence. Due to the binary nature of the outputs, we can evaluate accuracy in terms of pixels incorrectly labeled ("existence" or "absence" of cells), a metric we will later use to compare their performances.

For reliable 3D tissue imaging, it's imperative that the module maintains sensitivity and specificity performance across the specimen's entire depth. However, the limited performance of this module restricts its use for acquiring reliable 3D information and performing deep tissue imaging on samples thicker than a few hundred microns. Sensitivity is defined by the ratio of pixels accurately predicting cell presence over the total number of cancer cells in the ground truth images, while specificity evaluates the model's performance in predicting absence of cells in pixels indicated by the ground truth images to be empty of cells.

One critical application of cellular-level depth estimation in oncology is monitoring and observing cell movements and dynamics, representing real-time tissue responses to therapy. The speed, direction, and features of cell clusters undergoing these dynamics hold significant clinical value. However, due to the complexity and optical limitations of the imagers this goal remain elusive. Building on the depth estimation module, we present a 3D-reconstruction model architecture capable of capturing these cell cluster dynamics. The model's sensitivity to cell dynamics and movement across layers is evaluated quantitatively with a test set.

7.4 Non-overlapping Multi-layer Depth Estimation

A 6-layer network comprising 3 convolution and 3 deconvolution layers is trained on the dataset and the performance is evaluated on 1000 test samples. Fig. 7.2(a) demonstrates

an example of the merged image from the stacks at 250 μm and 800μm depths from the imagers, the ground truth depth map and the depth map predicted by the model. The error distribution of the depth map predicted by this network is shown in Fig. 7.2(b). The average normalized deviation of pixels from their correct value is 6.2% with a standard deviation of 10.4%.

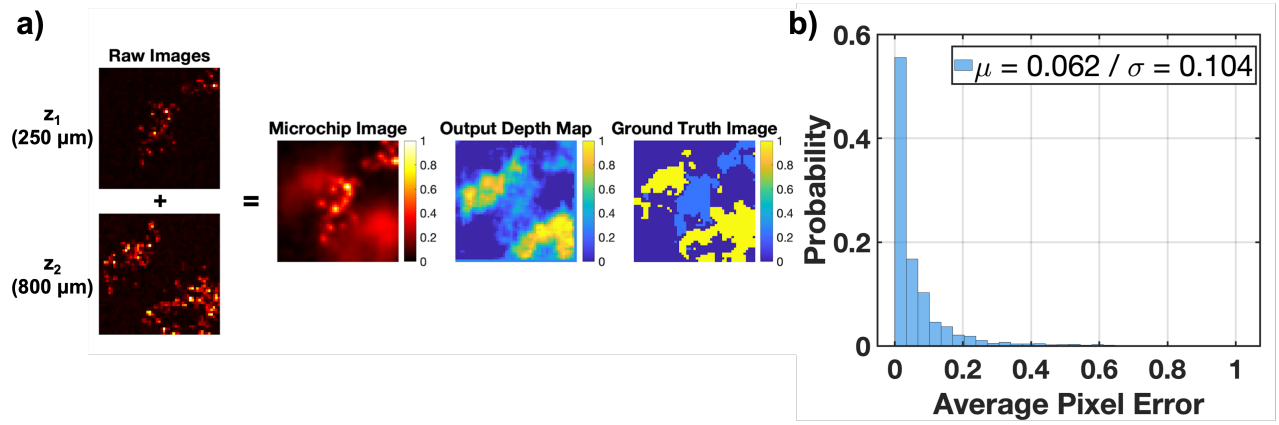

Figure 7.2: Performance of the cell detector module for non-overlapping stacks of cells: (a) Raw images at each depth before applying the PSF, network input and output images for a test sample and the corresponding ground truth image. (b) Distribution of average pixel error for test samples with a mean of 6.2% for 1000 test samples.

7.5 Overlapping Multi-Layer Depth Estimation

After successfully identifying two-layer depth map of tumor cells within a normal tissue background, we expand the application to a more comprehensive case with overlapping clusters of cells in this section.

CNN with Single Sensor

The first module for multi-layer cell detection is based on a single sensor, observing a stack of 4 layers of cells that are randomly spaced between 0 and 1 mm from the sensor itself.Each layer is at least 200 μm apart from the adjacent layer, ensuring full coverage of the three-dimensional space [0,1 mm] with only four layers. These layers are uncorrelated, and contain randomly generated intensities and background levels, providing a realistic emulation of tissue. After applying the corresponding PSF to each layer, the 4 images are merged together into one final image, constituting the sensor's output and serving as raw input to the module.

After training, the model is evaluated over 1000 distinct test inputs. An example of the input image and the corresponding output is shown in Fig. 7.3(a). The distribution of the

performance is shown in Fig. 7.3(b). Our performance metric reveals that the first layer, closest to the sensor, has a lower error rate of 28%, and the performance degrades with farther layers, with the rate of error consistently above 37%.

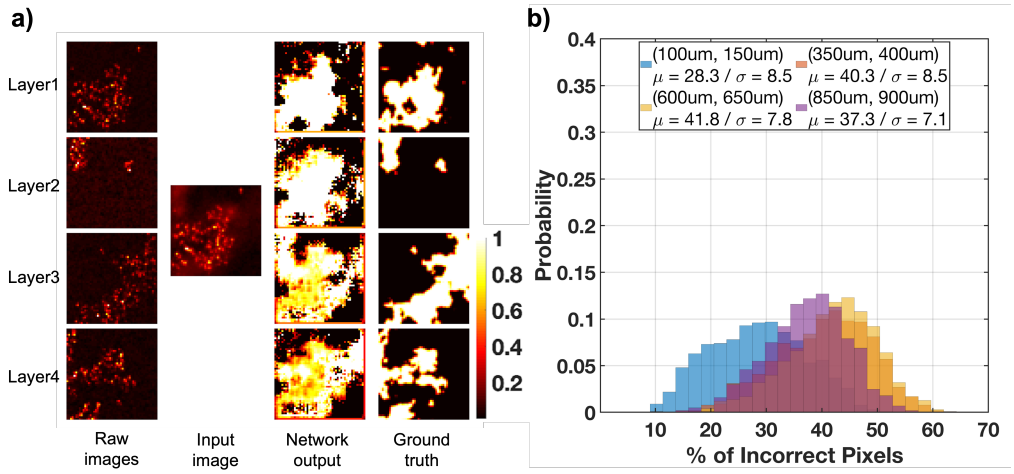

Figure 7.3: Performance of the CNN model with a single sensor. (a) Overlaid input image from 4 raw images of each layer, network output images and ground truth depth maps for each layer. (b) Distribution of average pixel error for test samples for each layer with averaged error rates of 28.3%, 40.3%, 41.8% and 37.3% for layers 1 to 4, respectively.

The performance distribution shown in Fig. 7.3 is influenced by the overlap of cells in the four layers. Further analysis of the individual data confirms that cases with lower counts of incorrect pixels observed in the distant layers result from subsequent cell layers significantly overlapping with the closest one, leading to special cases and lower-than-usual error rates.

CNN with Two Sensors

The effect of adding a second miniaturized imager to the opposite side of the target under test is investigated with the 4-layer overlapping image dataset and the improvement of accuracy is reported.

Using the same network as the single-sensor case, we evaluated the module with 1000 test inputs and the corresponding inputs and outputs for one sample image set is shown in Fig. 7.4(a). The distribution of errors in identifying the depth map in each layers is illustrated in Fig. 7.4(b). As expected, the first and last layers have very similar performances, as do the two middle ones, and this network can lower the error rate to 12% (in the two closest layers), which is less than half of the error rate of its single-sensor model. Compared to the single sensor approach, adding a second sensor reduces the error in the two middle layers – farthest from the sensor – reducing it from 40% to 18%.

Subsequently, by identifying the depth map of cancer cells in each layer, we can reconstruct the 3D distribution of the sample being imaged. Illustrated in Fig. 7.5, using the outputs

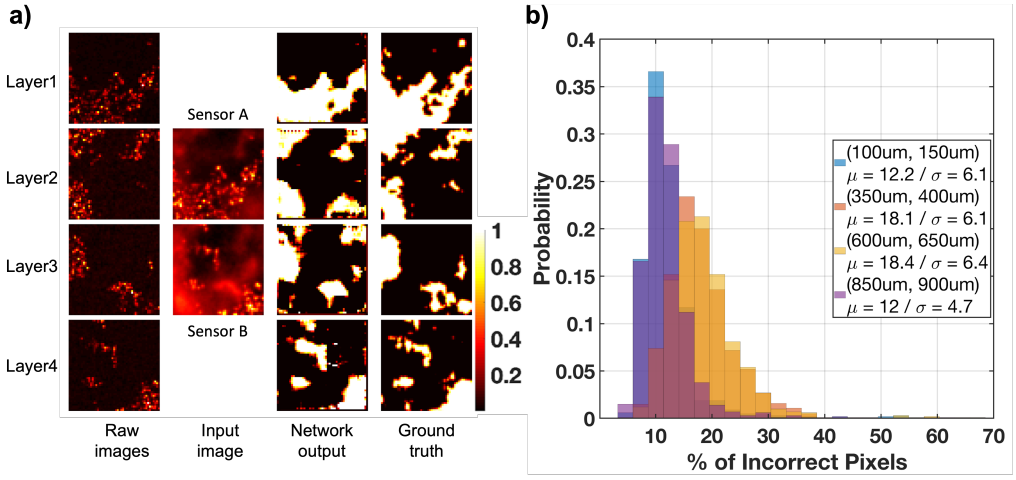

Figure 7.4: Evaluation of the CNN with two sensors. (a) Overlaid input images from 4 raw images corresponding to each layer before applying the PSF, network output images and ground truth depth maps. (b) Distribution of average pixel error for each layer with averaged error rates of 12.2%, 18.1%, 18.4% and 12% for layers 1 to 4, respectively.

shown in Fig. 7.4(a), we have reconstructed the stacked sample, identifying the zones where cancer cells were detected in each layer. For a complete representation of the proposed imaging platform, the two sensors are also shown in Fig. 7.5, separated by the 1 mm thick stack of cell layers in between.

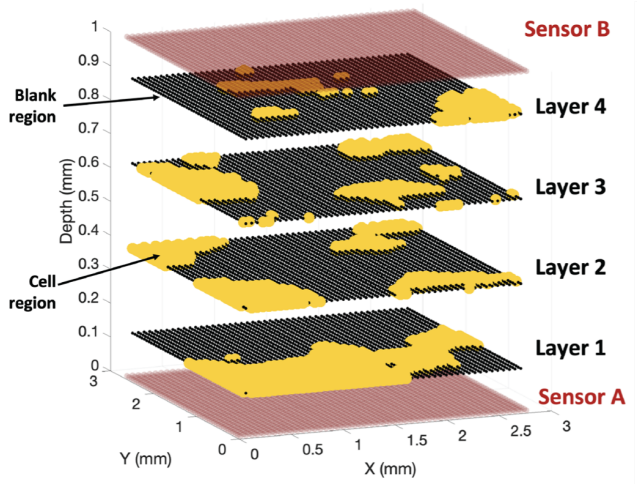

Figure 7.5: Spatial (3D) reconstruction (using network outputs) of the sample test input, where black, yellow and red respectively represent blank (empty of cells) spaces, regions containing cells, and sensor locations.

ResNet+CNN with Two Sensors

In this section, we introduce a module with the capability to identify cell clusters across all depths while exhibiting high sensitivity to subtle changes in the sample, such as those arising from cell cluster movements. By leveraging a larger neural network, this module can detect movements of clusters between layers, enabling visualization of dynamics within the tissue. Building upon the two-sensor architecture introduced earlier to enhance accuracy, we employ a pre-trained 18-layer ResNet architecture before the 2-layer CNN network preceded [106]. We evaluate the performance of the network on the test dataset. The architecture of the network and its input images and output depth maps are shown in Fig. 7.6. The details of the CNN used with the ResNet model are included in Fig. 7.7.

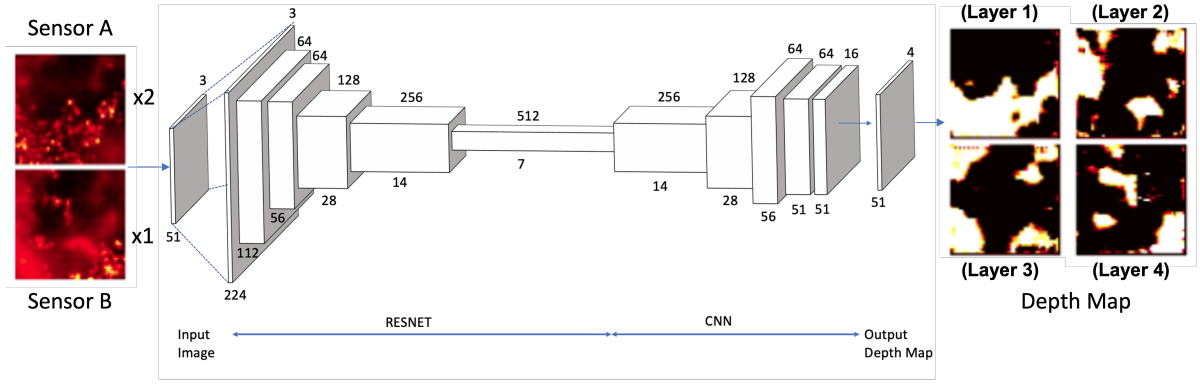

Figure 7.6: Architecture of the deep neural network consisting of 18-layer ResNet and CNN with the corresponding input images from 2 sensors and the output depth maps for 4 layers. A replica of the image from sensor A is added to the 2 input images to comply with the 3-channel input of ResNet.

The test dataset comprises 100 distinct and randomly generated images with a cluster of cells within the three-dimensional space moving across different layers, simulating physiological dynamics observed in real-life scenarios (e.g., immune cells migrating into a tumor or metastatic tumor migrating or dividing within tissue). Fig. 7.8 illustrates the cluster moving across the layers.

The distribution of errors of this module is shown in Fig. 7.9 and revealing that the two closest layers exhibit a very low error rate ($\sim$11%), while the two middle layers show slightly higher rates ($\sim$16%). The performance of the network for all layers demonstrates noticeable improvements compared to the CNN-only architecture.

Fig. 7.10 showcases the outputs of the module, consisting of four sections: raw (unblurred) images at different depths, network outputs, ground truth image, and the two sensor images captured, serving as input to the module. The cluster of cells highlighted in Fig. 7.10 traverses the four layers (from left to right), affecting the two sensor images every time a layer change occurs.

CNN

Layers	Feature size	Kernel	Stride
Upsample1	256x14x14	-	-
Upsample2	128x28x28	-	-
Upsample3	64x56x56	-	-
Conv1	16x53x53	(4,4)	1
Conv2	4x51x51	(3,3)	1

Upsample Layer

Layers	feature size	Kernel	Stride
maxunpool	C.2W.2L	(2,2)	2
conv1	C/2.2W.2L	(5,5)	1
ReLu			
conv2	C/4.2W.2L	(5,5)	1

Figure 7.7: Details of the CNN model and upsampling layers following the pre-trained ResNet model.

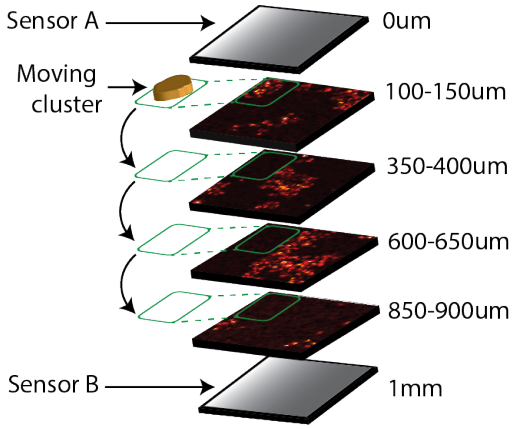

Figure 7.8: Test setup for modeling dynamics of a moving cell cluster.

The module tracks the cluster with an average sensitivity of 72.6% and specificity of 91.7% across all four layers, as depicted in Fig. 7.11(a). The Receiver Operating Characteristic (ROC) for the average performance of the model across all layers is illustrated in Fig. 7.11(b).

7.6 Future Directions

The models presented here combine the computational advantages of neural networks to improve cell detection accuracies in images captured with our customized image sensor. A more thorough exploration to optimize the network architecture is necessary to further

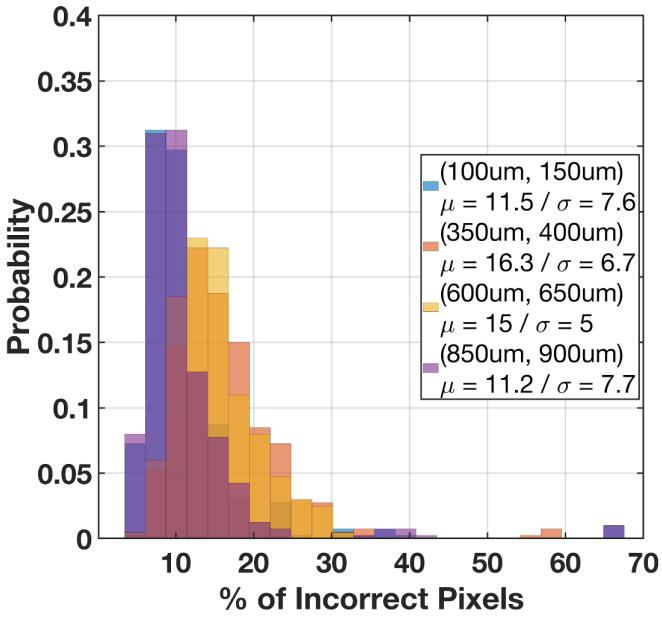

Figure 7.9: Performance of the ResNet+CNN model in identifying cell locations for each layer with average error rates of 11.5%, 16.3%, 15% and 11.2% for layers 1-4.

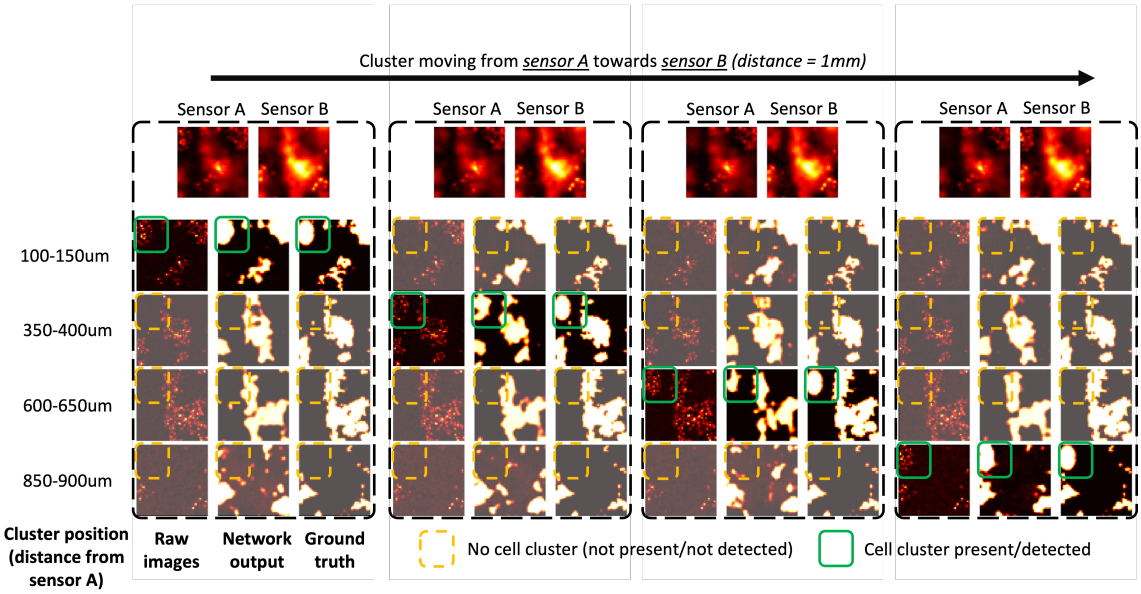

Figure 7.10: Outputs of the module with moving cell foci at each layer including the source images at each depth, the images captured by the 2 sensors, the network outputs and the ground truth cell maps at each depth.

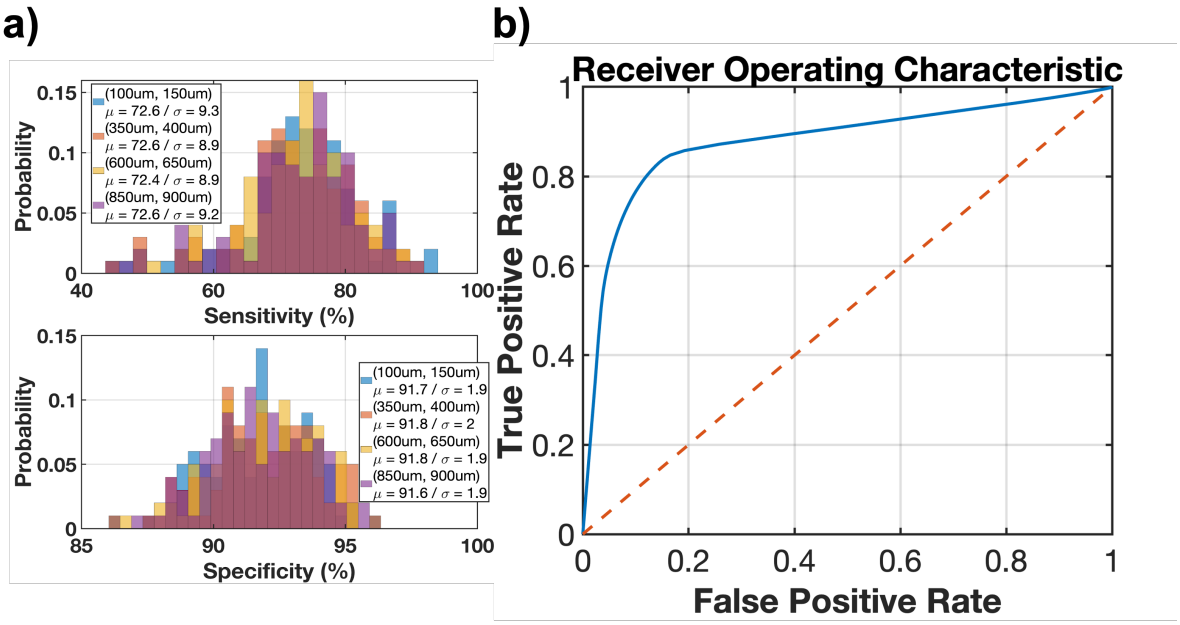

Figure 7.11: Performance of the ResNet+CNN module with the moving cell foci. (a) Sensitivity and specificity with 2-sensor network in detecting dynamics of the moving cell cluster for each layer. (b) Receiver Operating Characteristic (ROC) of the model averaged for all layers.

improve the performance of the proposed models.

However, our work faces several limitations. Despite our efforts to closely replicate real-life sample sets, we relied on a synthesized dataset. Our primary goal was to establish proof of concept with this technique, which can be repeated for any available cell imaging dataset by retraining the neural networks on that specific dataset. Despite the synthetic nature of the dataset, the final model (ResNet+CNN) demonstrates high level of performance when applied to real-life images in Fig. 7.12. While acquisition of a large number of real-life images of cancer cells exceeds the scope of this work, we applied the module to a limited number of cancer cell slides. Initially, these samples were imaged using a high-resolution fluorescence microscope (shown in the first column in Fig. 7.12). Subsequently, each slide was assigned a randomly selected depth, and the corresponding PSF was applied. After applying the PSF, all 4 layers were merged to generate the sensor image. A similar procedure was repeated for the second sensor. The sensor images obtained are shown in the second column of Fig. 7.12. The network output is presented in the third column, and an overlay composite image of the outputs with the microscope images is also shown in the rightmost column in Fig. 7.12, showing an almost perfect level of localized cell detection.

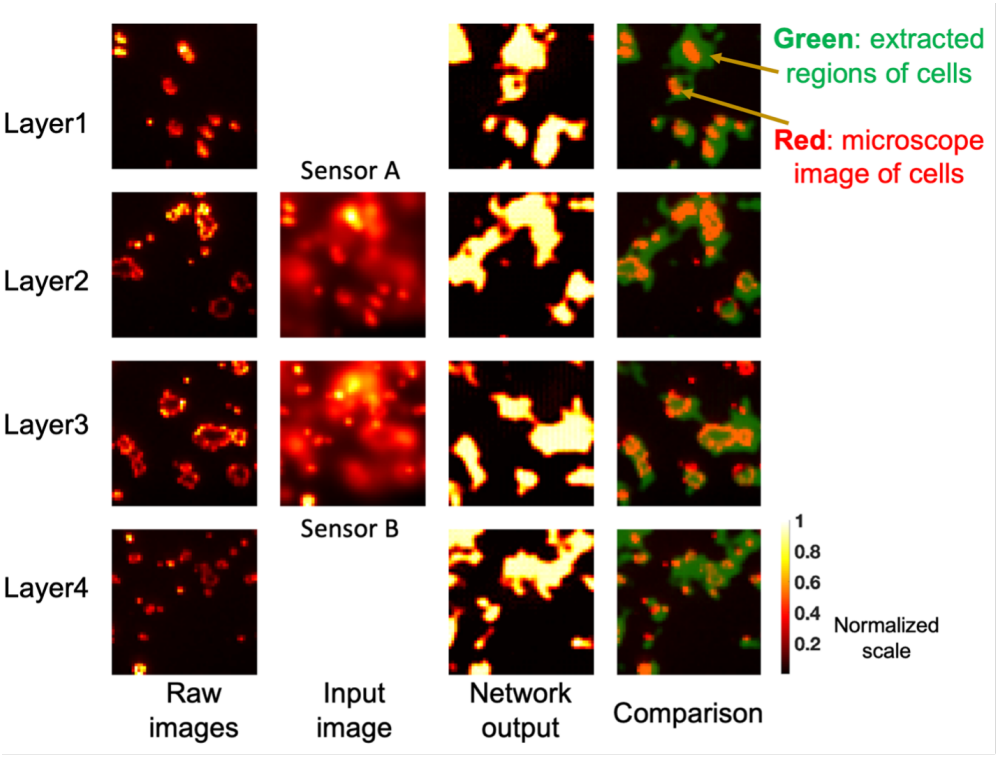

Figure 7.12: Evaluation of the CNN with two sensors on real-life cancer cell slides. (From left) input images from 4 raw microscope images corresponding to each layer before applying the PSF, sensor images, network output images showing regions where cells were detected, and merged image of network output and microscope images for each layer.

7.7 Contributions

The figures in this chapter are adapted from the following article:

1. H. Najafiaghdam, **R. Rabbani**, A. Gharia, E. P. Papageorgiou, M. Anwar, "3D Reconstruction of cellular images from microfabricated imagers using fully-adaptive deep neural networks". *Scientific Reports* 12, 7229 (2022).

Personal Contribution: I contributed to the synthesis of the training dataset for the non-overlapping and overlapping images. I collaborated on the design and evaluation of the RESNET+CNN network and generating the ROC plot.

Acknowledgments: H. Najafiaghdam was the main contributor of this work. He designed of the CNN networks and tested the network's performance with the moving cell foci and the real cancer cell images. The image sensor model was adapted from the work of E. P. Papageorgiou. A. Gharia worked on image data synthesis using Perlin noise.

Chapter 8

Conclusion

This thesis presents a wireless fluorescence image sensor aiming to monitor the intricate dynamics of immune system's response to cancer immunotherapy providing insights for assessing therapeutic response and disease progression. Detection of resistance mechanisms at early time points of therapy is essential to enable personalized medicine which is currently not possible with the clinical modalities such as MRI, CT or PET.

8.1 Summary

To accomplish this goal, we introduced the first chip-scale, multicolor fluorescence image sensor capable of 1) wireless operation and 2) in-situ illumination for imaging deep in the tissue. Miniaturization is necessary for chronic implantation and is achieved by 1) device-level integration of the μLDs and elimination of bulky optics such as focusing lenses and fibers and 2) wireless power transfer and communication using a 1.5x1.5x1.5 mm^3 piezo instead of batteries or any external wiring. Prior chip-scale fluorescence imagers in [34, 36, 37] lack wireless compatibility or rely on batteries for power [35], thus they are not practical for long-term implantation.

In this thesis, we outlined system design requirements for detection of small cell foci to determine the components needed for the system. Next, we introduced the first generation of the device, a proof-of-concept platform for wireless, single color fluorescence imaging and showcased its performance. The system incorporates an off-chip capacitor to store wireless energy from an ultrasound link and later provide high instantaneous power for fluorescence excitation. For each frame, 11.52 kbits of image data are transmitted via ultrasound backscattering using the same piezoceramic transceiver used for power transfer. In the wired mode, the imager can capture high-resolution *ex vivo* images of CD8+ T-cell profiles, an indicator of the immune response, consistent with images taken with a high-resolution fluorescence microscope. The overall system performance is demonstrated by resolving 140 μm features on a resolution test target obtained wirelessly with the sensor. However, limitations such as operation above FDA limits and low imager sensitivity restricted wireless imaging to

high concentrations of fluorescent dye. Challenges such as size, input power requirements, leakage, lack of wireless programmability and inadequate depth of operation motivated design of the next generation of the sensor.

Therefore, we expanded the idea to a fully wireless, multi-color fluorescence image sensor with new capabilities specifically designed for multiplexed imaging of multiple cell types. The new system features a three-channel laser driver to supply μLDs with different wavelengths, a US downlink for programming imaging and laser configurations, and an optical frontend design comprising a multi-bandpass interference filter and a FOP. Through a power harvesting frontend incorporating a cross-coupled charge-pump, we achieve safe operation at a 5 cm depth in oil, with US power densities at 31% of FDA limits. The robust communication link demonstrates a BER better than 10^{-6} at a 13 kbps data rate. Additionally, optimizing the storage capacitor sizing enables a compact form factor of 0.09 cm^3, as demonstrated through mechanical assembly of the implant. The optical frontend provides >6 OD of excitation rejection to accommodate the small Stokes shift of organic fluorophores.

To showcase the significance of multicolor fluorescence imaging in identifying immune system's control mechanisms in immunotherapy, we imaged CD8+ T-cell and neutrophil populations in *ex vivo* mouse tumors with or without immunotherapy. A comparison of both sensors with recent chip-scale fluorescence imagers and sensors is provided in Table 8.1.

As the sensors discussed in this work are lensless contact imagers, detection is limited to the targets in close proximity to the imager. Therefore, access to 3D information from the multicellular foci remains elusive. Linear deconvolution techniques with the point spread function of the image sensor require calibration and are susceptible to noise and they are blind to the properties of the image. As a result, we proposed deep neural networks for 3D reconstruction through depth estimation from images acquired with the custom designed imager. To train the networks, a large synthetic dataset representative of real cancer cell images is presented. Accuracies of 93.8% and 86.5% for cell localization and depth estimation of non-overlapping and overlapping stacks of multiple layers of cells are achieved, respectively.

8.2 Future Directions

While we have successfully demonstrated the sensor's capability in imaging the dynamic, multiplexed biological processes, key challenges are yet to be addressed before conducting *in vivo* experiments in the future. A summary of future steps to facilitate *in vivo* applications of the device is listed below:

Efficiency Improvements

With the current power management unit, the charge-up interval (35-50 s) dominates the frame time. This duration can be significantly reduced by incorporating more efficient power harvesting interfaces. During charge-Up, the active rectifier extracts the input energy solely when the AC voltage exceeds the rectified voltage, occurring within a limited portion

	Metric	Rustami et al. TCAS-I 2020 [37]	Moazeni et al. TBioCAS 2021 [34]	Aghlmand et al. JSSC 2023 [36]	Zhu et al. TBioCAS 2023 [35]	**This work Sensor I**	**This work Sensor II**
System	Application	*In vivo* neural imaging	*In vivo* neural imaging/stimulation	Bio-molecular sensing	*In vivo* bio-molecular sensing	***In vivo* imaging of treatment response**	***In vivo* imaging of treatment response**
	Technology	350nm	130nm	65nm	65nm	**180nm**	**180nm**
	Power Source	Power Supply	Power supply	Power supply	Battery	**Wireless (US)**	**Wireless (US)**
	Wireless Link	No	No	No	Yes (RF)	**Yes (US)**	**Yes (US)**
	Bit Error Rate	N/A	N/A	N/A	10^{-3}–10^{-7}*	**$4x10^{-3}$–$9x10^{-5}$****	**$<10^{-6}$**
	Wireless Depth	N/A	N/R	N/A	N/A	**2cm†**	**Up to 5cm**
	Implant Volume	N/A	N/A	N/A	1.37cm^3	N/A	**0.09cm^3††**
Fluorescence Imaging Frontend	Filter Type	Absorption + interference (bandpass)	Absorption + interference + time gating (longpass)	CMOS grating (single bandpass)	CMOS nano-plasmonic (longpass)	**Interference (bandpass) + FOP**	**Multi-bandpass Interference + FOP**
	Fluorescent Target	*Ex vivo* brain slice	Fluorescent beads	*In vitro* E. coli cells‡	*In vitro* DNA assay	**Fluorescent dye**	***Ex vivo* immune cells**
	Excitation/ Emission Peak (nm)	473/510 (GFP)	470/520 (YG beads)	440/570 (mCherry), 550/600 (LSSmOrange)‡	405/800 (Qdot 800)	**683/703 (Cy5.5)**	**455/500 (FAM), 650/670 (Cy5), 785/800 (beads)**
	Excitation Rejection	N/R	5OD	2.8OD	3.9OD	**>6OD‡‡**	**>6OD‡‡**
	Resolution	22μm	<60 μm	N/A	N/A	**140μm**	**<125μm**
	Pixel Array Size	40×400	160×160	3×4	3×5	**36×40**	**36×40**
	PD Active Area	7.5×7.5μm^2	7.5μm (diameter)	100×100μm^2	150×170μm^2	**44×44μm^2**	**44×44μm^2**
	Total Output Noise§	N/R	N/R	3.8mV§§	1.4mV#	**N/R**	**5.4mV##**
	Imager Power¶	N/R	40mW	19.1mW	N/R	**N/R**	**2.09mW**

N/A Not Applicable, N/R Not Reported, OD Optical Density, * Depends on transmitter power, ** Depends on harvested voltage, † Exceeds FDA limits by 26%, †† Mechanical Assembly, ‡ Other targets and fluorophores also used, ‡‡ at angles > 5∘, § Under dark condition, §§ T_{EXP}=1 s, # Estimated from reported shot and CTIA noise, ## T_{EXP}=8 ms, ¶ Includes power of full pixel array, readout, and control.

Table 8.1: Comparison of state-of-the-art chip-scale fluorescence image sensors

of the complete period of the US carrier. Moreover, the energy extraction window is further reduced as the rectified voltage stabilizes to its final value.

Synchronized switch harvesting techniques on inductors (SSHI) [107] have been proposed to minimize the transition period and improve efficiency of the rectifier by up to 4×. In this method, teh voltage across the piezo is synchronously flipped to minimize energy loss due to charging the internal capacitor of the piezo (∼10s of pF). However, inductors are not practical for miniaturized implants due to their large volume. The work in [108] introduces synchronized switch harvesting techniques on capacitors (SSHC) resulting in up to 9.7× improvement in performance compared to full bridge rectifiers while significantly reducing the volume. Designing a full-fledged digital control circuit for the implant to enable switching the rectifier is critical for employing these techniques.

Encapsulation

Implantable devices use inorganic (Al2O3, HfO2, SiO2, SiC, etc.) or organic (Polyimide, Parylene, liquid crystal polymer (LCP), silicone elastomer) materials for biocompatible encapsulation [109, 110]. The optimal duration of most immune checkpoint inhibitor immunotherapy procedures is typically less than 2 years [111]. Biocompatible encapsulations with Parylene C, Polyimide, PDMS have shown lifetimes ranging from several months to years according to failure tests ensuring that the device will maintain its performance throughout the majority of immunotherapy procedures [109, 112]. Thin layers of Parylene C are popular due to low moisture and gas permeability and have been used in several implants for their small damping effects on the acoustic vibrations [5, 113].

Possible mechanisms of optical loss in the encapsulation layers for our system are intensity reduction due to absorption and reflection at the interface of tissue, and degradation of resolution due to scattering as shown in [114]. The effect of light penetration for the implant coated with a 10-μm thick layer of Parylene C which has demonstrated an equivalent lifetime of one or more years at 37∘ [29] is analyzed given its refractive index of 1.592- 1.639.

Absorption: Absorption is negligible due to the small thickness of the Parylene C layer. I is the light intensity after passing through the coating layer and I_0 is the initial intensity. $\mu_a \approx 1$ cm^{-1} is the absorption coefficient at λ=635 nm [115]. d=20 μm is the round trip distance to and from the sample passing through the encapsulation layer assuming similar μ_a for excitation and emission wavelengths:

$$I = I_0 exp(-\mu_a d)$$

$$Transmittance: T = \frac{I}{I_0} = 99.8\%$$

Reflection: Transmission at the Parylene(n=1.62)-tissue(n=1.45) interface is plotted in Fig.8.1 across incidence angles for both TE and TM modes [80]. Transmission is zero for angles larger than the critical angle (63.4). For angles <50°, transmission is higher than 97%.

The above results demonstrate an overall transmission higher than 96% (for incident excitation angles $> 50°$) indicating the viability of biocompatible encapsulation for optical devices. Even though polymer-based encapsulations are preferable due to simplicity and lower processing temperature, they don't provide an impermeable barrier. Therefore, better encapsulation methods using hermetic barriers such as ceramics, and glasses with higher hermeticity can be used for longer-term applications.

Characterization of Foreign Body Reaction

Foreign body reaction to implanted biosensors is one of the key challenges that need to be addressed for *in vivo* experiments. This effect has been investigated extensively, indicating that factors such as size, shape, flexibility, and material type play an important role in determining biocompatibility of the device [116, 117].

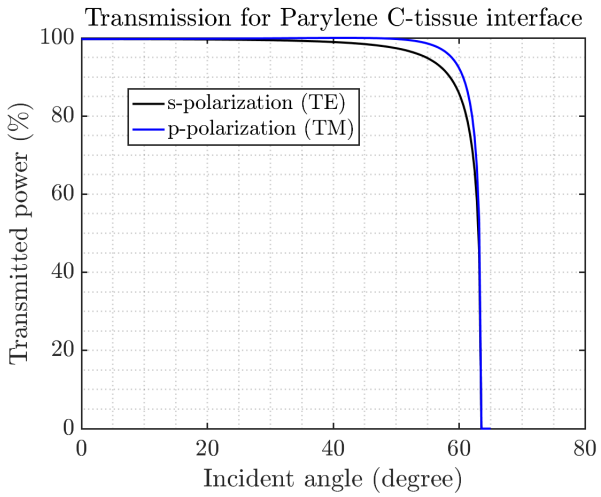

Figure 8.1: Transmission in Parylene C - tissue interface across angles of incidence

An important distinction between an image sensor and a fluorescence sensor lies in the access to cell-type identity information – as determined by molecular markers. By looking for specific cell types, this allows for elimination of changes of the majority of non-contributory cell information (such as general tissue inflammation response, tumor stroma changes, etc.). This feature enhances our ability to discern the tumor microenvironment beyond mere signal intensity which can give insights into changes in cell distribution, cell movements, and cell-to-imager distance as real-time images can be obtained wirelessly in the future.

Given that the device is designed for real-time imaging, the immune response can be monitored during the inflammatory reaction to device implantation. Once the inflammatory response has settled, we can then focus on capturing the immune response to cancer. A baseline measurement with the sensor before administration of the therapy can be subtracted from subsequent measurements after the administration of therapy to rule out any confounding response to the implant.

With future advancements in system integration in a biocompatible package and minimization of the form factor, our platform holds promise for enabling real-time chronic monitoring of multiple cell populations deep within the body, increasing visibility into the tumor microenvironment and guiding cancer therapy.

Bibliography

[1] Hatice Ceylan Koydemir and Aydogan Ozcan. "Wearable and Implantable Sensors for Biomedical Applications". In: *Annual Review of Analytical Chemistry* 11.1 (June 12, 2018), pp. 127–146.

[2] Azar Yadegari, Mohammad Azim Karami, and Mohammad Reza Daliri. "Neural Monitoring With CMOS Image Sensors". In: *Basic and Clinical Neuroscience* 9.3 (2018), pp. 227–235.

[3] A. Kim et al. "An Ultrasonically Powered Implantable Microprobe for Electrolytic Ablation". In: *Scientific Reports* 10.1 (Jan. 30, 2020). Number: 1 Publisher: Nature Publishing Group, p. 1510.

[4] Kyeongha Kwon et al. "A battery-less wireless implant for the continuous monitoring of vascular pressure, flow rate and temperature". In: *Nature Biomedical Engineering* (Apr. 10, 2023). Publisher: Nature Publishing Group, pp. 1–14.

[5] Soner Sonmezoglu et al. "Monitoring deep-tissue oxygenation with a millimeter-scale ultrasonic implant". In: *Nature Biotechnology* 39.7 (July 2021). Number: 7 Publisher: Nature Publishing Group, pp. 855–864.

[6] Hodi F. Stephen et al. "Improved Survival with Ipilimumab in Patients with Metastatic Melanoma". In: *New England Journal of Medicine* 363.8 (2010). Publisher: Massachusetts Medical Society, pp. 711–723.

[7] Reck Martin et al. "Pembrolizumab versus Chemotherapy for PD-L1–Positive Non–Small-Cell Lung Cancer". In: *New England Journal of Medicine* 375.19 (2016), pp. 1823–1833.

[8] Shirish Gadgeel et al. "Updated Analysis From KEYNOTE-189: Pembrolizumab or Placebo Plus Pemetrexed and Platinum for Previously Untreated Metastatic Nonsquamous Non-Small-Cell Lung Cancer". In: *Journal of Clinical Oncology: Official Journal of the American Society of Clinical Oncology* 38.14 (May 10, 2020), pp. 1505–1517.

[9] Alyson Haslam and Vinay Prasad. "Estimation of the percentage of us patients with cancer who are eligible for and respond to checkpoint inhibitor immunotherapy drugs". In: *JAMA Network Open* 2.5 (May 1, 2019). Publisher: American Medical Association.

[10] Golnaz Morad et al. "Hallmarks of response, resistance, and toxicity to immune checkpoint blockade". In: *Cell* 184.21 (Oct. 14, 2021). Publisher: Elsevier B.V., pp. 5309–5337.

[11] Satya Das and Douglas B. Johnson. "Immune-related adverse events and anti-tumor efficacy of immune checkpoint inhibitors". In: *Journal for ImmunoTherapy of Cancer* 7.1 (Nov. 15, 2019). Publisher: BioMed Central Ltd.

[12] Vivek Verma et al. "A systematic review of the cost and cost-effectiveness studies of immune checkpoint inhibitors". In: *Journal for Immunotherapy of Cancer* 6 (Nov. 23, 2018), p. 128.

[13] Chi-leung Chiang et al. "Cost-effectiveness of Pembrolizumab as a Second-Line Therapy for Hepatocellular Carcinoma". In: *JAMA Network Open* 4.1 (Jan. 19, 2021), e2033761.

[14] Fathinul Fikri Ahmad Saad. *Molecular Imaging*. Publication Title: Selected Topics on Computed Tomography. IntechOpen, May 15, 2013.

[15] Chrysafis Andreou, Ralph Weissleder, and Moritz F. Kircher. "Multiplexed imaging in oncology". In: *Nature Biomedical Engineering* 6.5 (May 2022). Number: 5 Publisher: Nature Publishing Group, pp. 527–540.

[16] Louis F. Chai et al. "Challenges in assessing solid tumor responses to immunotherapy". In: *Cancer Gene Therapy* 27.7 (Aug. 1, 2020). Publisher: Springer Nature, pp. 528–538.

[17] Mizuki Nishino, Hiroto Hatabu, and F. Stephen Hodi. "Imaging of cancer immunotherapy: Current approaches and future directions". In: *Radiology* 290.1 (Jan. 1, 2019). Publisher: Radiological Society of North America Inc., pp. 9–22.

[18] Lesley Seymour et al. "iRECIST: guidelines for response criteria for use in trials testing immunotherapeutics". In: *The Lancet. Oncology* 18.3 (Mar. 2017), e143–e152.

[19] Marcus Unterrainer et al. "PET/CT imaging for tumour response assessment to immunotherapy: current status and future directions". In: *European Radiology Experimental* 4.1 (Dec. 1, 2020). Publisher: Springer Science and Business Media Deutschland GmbH.

[20] Edwin C. Pratt et al. "Simultaneous quantitative imaging of two PET radiotracers via the detection of positron–electron annihilation and prompt gamma emissions". In: *Nature Biomedical Engineering* 7.8 (Aug. 2023). Publisher: Nature Publishing Group, pp. 1028–1039.

[21] William W. Moses. "Fundamental Limits of Spatial Resolution in PET". In: *Nuclear instruments & methods in physics research. Section A, Accelerators, spectrometers, detectors and associated equipment* 648 Supplement 1 (Aug. 8, 2011). Publisher: NIH Public Access, S236.

[22] Geoffrey T. Gibney, Louis M. Weiner, and Michael B. Atkins. "Predictive biomarkers for checkpoint inhibitor-based immunotherapy". In: *The Lancet Oncology* 17.12 (Dec. 1, 2016). Publisher: Elsevier, e542–e551.

[23] Ying Yang et al. "Liquid biopsy on the horizon in immunotherapy of non-small cell lung cancer: current status, challenges, and perspectives". In: *Cell Death & Disease* 14.3 (Mar. 31, 2023). Publisher: Nature Publishing Group, pp. 1–15.

[24] Satyen H. Gohil et al. "Applying high-dimensional single-cell technologies to the analysis of cancer immunotherapy". In: *Nature Reviews Clinical Oncology* 18.4 (Apr. 2021). Publisher: Nature Publishing Group, pp. 244–256.

[25] Ilio Vitale et al. "Intratumoral heterogeneity in cancer progression and response to immunotherapy". In: *Nature Medicine* 27.2 (Feb. 2021). Publisher: Nature Publishing Group, pp. 212–224.

[26] "Imaging more of the body". In: *Nature Biomedical Engineering* 6.5 (May 2022). Number: 5 Publisher: Nature Publishing Group, pp. 495–496.

[27] Jeff W. Lichtman and José-Angel Conchello. "Fluorescence microscopy". In: *Nature Methods* 2.12 (Dec. 2005). Publisher: Nature Publishing Group, pp. 910–919.

[28] Eric A. Owens et al. "NIR fluorescent small molecules for intraoperative imaging". In: *WIREs Nanomedicine and Nanobiotechnology* 7.6 (2015), pp. 828–838.

[29] Maria Alieva et al. "Imaging windows for long-term intravital imaging". In: *IntraVital* 3.2 (Aug. 11, 2014), e29917.

[30] Andrius Masedunskas et al. "Intravital microscopy". In: *Bioarchitecture* 2.5 (Sept. 1, 2012), pp. 143–157.

[31] Yeon Woong Choo, Juhee Jeong, and Keehoon Jung. "Recent advances in intravital microscopy for investigation of dynamic cellular behavior in vivo". In: *BMB Reports* 53.7 (July 31, 2020), pp. 357–366.

[32] Ravikumar Vaghela et al. "Actually Seeing What Is Going on – Intravital Microscopy in Tissue Engineering". In: *Frontiers in Bioengineering and Biotechnology* 9 (2021).

[33] Efthymios P. Papageorgiou, Bernhard E. Boser, and Mekhail Anwar. "Chip-Scale Angle-Selective Imager for In Vivo Microscopic Cancer Detection". In: *IEEE Transactions on Biomedical Circuits and Systems* 14.1 (Feb. 2020). Conference Name: IEEE Transactions on Biomedical Circuits and Systems, pp. 91–103.

[34] Sajjad Moazeni et al. "A Mechanically Flexible, Implantable Neural Interface for Computational Imaging and Optogenetic Stimulation Over 5.4×5.4mm2 FoV". In: *IEEE Transactions on Biomedical Circuits and Systems* 15.6 (Dec. 2021). Conference Name: IEEE Transactions on Biomedical Circuits and Systems, pp. 1295–1305.

[35] Chengjie Zhu et al. "An Ingestible Pill With CMOS Fluorescence Sensor Array, Bi-Directional Wireless Interface and Packaged Optics for In-Vivo Bio-Molecular Sensing". In: *IEEE Transactions on Biomedical Circuits and Systems* (2023). Conference Name: IEEE Transactions on Biomedical Circuits and Systems, pp. 1–17.

[36] Fatemeh Aghlmand et al. "A 65-nm CMOS Fluorescence Sensor for Dynamic Monitoring of Living Cells". In: *IEEE Journal of Solid-State Circuits* 58.11 (Nov. 2023), pp. 3003–3019.

[37] Erus Rustami et al. "Needle-Type Imager Sensor With Band-Pass Composite Emission Filter and Parallel Fiber-Coupled Laser Excitation". In: *IEEE Transactions on Circuits and Systems I: Regular Papers* 67.4 (Apr. 2020). Conference Name: IEEE Transactions on Circuits and Systems I: Regular Papers, pp. 1082–1091.

[38] Takuma Kobayashi et al. ""Optical communication with brain cells by means of an implanted duplex micro-device with optogenetics and Ca2+ fluoroimaging"". In: *Scientific Reports* 6.1 (Feb. 16, 2016). Number: 1 Publisher: Nature Publishing Group, p. 21247.

[39] Eric H. Pollmann et al. *Subdural CMOS optical probe (SCOPe) for bidirectional neural interfacing*. preprint. Neuroscience, Feb. 8, 2023.

[40] Jaebin Choi et al. "Fully Integrated Time-Gated 3D Fluorescence Imager for Deep Neural Imaging". In: *IEEE Transactions on Biomedical Circuits and Systems* 14.4 (Aug. 2020). Conference Name: IEEE Transactions on Biomedical Circuits and Systems, pp. 636–645.

[41] Efthymios P. Papageorgiou et al. "Angle-insensitive amorphous silicon optical filter for fluorescence contact imaging". In: *Optics Letters* 43.3 (Feb. 1, 2018). Publisher: The Optical Society, p. 354.

[42] Ahmed Sawaby et al. "A Wireless Implantable Ultrasound Array Receiver for Thermoacoustic Imaging". In: *2018 IEEE Symposium on VLSI Circuits*. 2018 IEEE Symposium on VLSI Circuits. ISSN: 2158-5601. June 2018, pp. 189–190.

[43] Jiawen Li et al. "Perspective: Biomedical sensing and imaging with optical fibers-Innovation through convergence of science disciplines". In: *APL Photonics* 3.10 (Oct. 2018). Publisher: American Institute of Physics, p. 100902.

[44] Peiran Chen et al. "Acoustic characterization of tissue-mimicking materials for ultrasound perfusion imaging research". In: *Ultrasound in Medicine & Biology* 48.1 (Jan. 1, 2022), pp. 124–142.

[45] Amanda Singer and Jacob T. Robinson. "Wireless Power Delivery Techniques for Miniature Implantable Bioelectronics". In: *Advanced Healthcare Materials* 10.17 (2021), p. 2100664.

[46] Hamid Basaeri, David B Christensen, and Shad Roundy. "A review of acoustic power transfer for bio-medical implants". In: *Smart Materials and Structures* 25.12 (Dec. 1, 2016), p. 123001.

[47] Micah Roschelle et al. "Multicolor fluorescence microscopy for surgical guidance using a chip-scale imager with a low-NA fiber optic plate and a multi-bandpass interference filter". In: *Biomedical Optics Express* 15.3 (Mar. 1, 2024). Publisher: Optica Publishing Group, pp. 1761–1776.

[48] Rozhan Rabbani et al. "Towards an Implantable Fluorescence Image Sensor for Real-Time Monitoring of Immune Response in Cancer Therapy". In: *2021 43rd Annual International Conference of the IEEE Engineering in Medicine & Biology Society (EMBC)*. 2021 43rd Annual International Conference of the IEEE Engineering in Medicine & Biology Society (EMBC). ISSN: 2694-0604. Nov. 2021, pp. 7399–7403.

[49] Rozhan Rabbani et al. "A 36×40 Wireless Fluorescence Image Sensor for Real-Time Microscopy in Cancer Therapy". In: *2022 IEEE Custom Integrated Circuits Conference (CICC)*. 2022 IEEE Custom Integrated Circuits Conference (CICC). ISSN: 2152-3630. Apr. 2022, pp. 1–2.

[50] Rozhan Rabbani et al. "Towards A Wireless Image Sensor for Real-Time Fluorescence Microscopy in Cancer Therapy". In: *IEEE Transactions on Biomedical Circuits and Systems* (2024), pp. 1–15.

[51] Rozhan Rabbani et al. "17.3 A Fully Wireless, Miniaturized, Multicolor Fluorescence Image Sensor Implant for Real-Time Monitoring in Cancer Therapy". In: *2024 IEEE International Solid-State Circuits Conference (ISSCC)*. 2024 IEEE International Solid-State Circuits Conference (ISSCC). Vol. 67. ISSN: 2376-8606. Feb. 2024, pp. 318–320.

[52] Lingyu Hong et al. "Fully Integrated Fluorescence Biosensors On-Chip Employing Multi-Functional Nanoplasmonic Optical Structures in CMOS". In: *IEEE Journal of Solid-State Circuits* 52.9 (Sept. 1, 2017). Publisher: Institute of Electrical and Electronics Engineers Inc., pp. 2388–2406.

[53] Connor W. Barth and Summer L. Gibbs. "Fluorescence Image-Guided Surgery – a Perspective on Contrast Agent Development". In: *Proceedings of SPIE–the International Society for Optical Engineering* 11222 (Feb. 2020), 112220J.

[54] Jason M. Warram et al. "Antibody-based imaging strategies for cancer". In: *Cancer and Metastasis Reviews* 33.2 (Sept. 1, 2014), pp. 809–822.

[55] Jaebin Choi et al. "A 512-Pixel, 51-kHz-Frame-Rate, Dual-Shank, Lens-Less, Filter-Less Single-Photon Avalanche Diode CMOS Neural Imaging Probe". In: *IEEE Journal of Solid-State Circuits* 54.11 (Nov. 2019). Conference Name: IEEE Journal of Solid-State Circuits, pp. 2957–2968.

[56] Hossein Najafiaghdam et al. "Optics-Free Chip-Scale Intraoperative Imaging Using NIR-Excited Upconverting Nanoparticles". In: *IEEE Transactions on Biomedical Circuits and Systems* 16.2 (Apr. 1, 2022). Publisher: Institute of Electrical and Electronics Engineers Inc., pp. 312–323.

[57] Mikhail Y. Berezin and Samuel Achilefu. "Fluorescence Lifetime Measurements and Biological Imaging". In: *Chemical Reviews* 110.5 (May 12, 2010). Publisher: American Chemical Society, pp. 2641–2684.

[58] Richard P. Haugland and Karen D. Larison. *Handbook of fluorescent probes and research chemicals*. 5th ed., 1992-1994. Section: 421 pages : illustrations ; 28 cm. Eugene, OR, USA (4849 Pitchford Ave., Eugene 97402): Molecular Probes, 1992.

[59] Chunyan Li and Qiangbin Wang. "Challenges and Opportunities for Intravital Near-Infrared Fluorescence Imaging Technology in the Second Transparency Window". In: *ACS Nano* 12.10 (Oct. 23, 2018), pp. 9654–9659.

[60] A.C. Croce and G. Bottiroli. "Autofluorescence Spectroscopy and Imaging: A Tool for Biomedical Research and Diagnosis". In: *European Journal of Histochemistry : EJH* 58.4 (Dec. 12, 2014), p. 2461.

[61] Mohamad Izzat Azmer et al. "Miniaturized LED light source with an excitation filter for fluorescent imaging". In: *Japanese Journal of Applied Physics* 60 (SB Mar. 2021). Publisher: IOP Publishing, SBBG07.

[62] Wan Shen Hee et al. "Lens-free dual-color fluorescent CMOS image sensor for förster resonance energy transfer imaging". In: *Sensors and Materials* 31.3 (2019). Publisher: M Y U Scientific Publishing Division, pp. 2579–2594.

[63] Adriaan J. Taal et al. "Toward implantable devices for angle-sensitive, lens-less, multifluorescent, single-photon lifetime imaging in the brain using Fabry–Perot and absorptive color filters". In: *Light: Science and Applications* 11.1 (Dec. 1, 2022). Publisher: Springer Nature.

[64] Kiyotaka Sasagawa et al. "Front-light Structure for a Lensless Fluorescence Imaging Device with a Hybrid Emission Filter". In: *2023 IEEE Biomedical Circuits and Systems Conference (BioCAS)*. 2023 IEEE Biomedical Circuits and Systems Conference (BioCAS). ISSN: 2766-4465. Oct. 2023, pp. 1–5.

[65] John V Frangioni. "*In vivo* near-infrared fluorescence imaging". In: *Current Opinion in Chemical Biology* 7.5 (Oct. 1, 2003), pp. 626–634.

[66] Yuanyuan Ji et al. "Near-infrared fluorescence imaging in immunotherapy". In: (2020).

[67] Mohammad Meraj Ghanbari and Rikky Muller. "Optimizing Volumetric Efficiency and Backscatter Communication in Biosensing Ultrasonic Implants". In: *IEEE Transactions on Biomedical Circuits and Systems* 14.6 (Dec. 2020). Conference Name: IEEE Transactions on Biomedical Circuits and Systems, pp. 1381–1392.

[68] N. Gladwell et al. "Ultrasonic behavior of edible oils: Correlation with rheology". In: *Journal of the American Oil Chemists' Society* 62.8 (Aug. 1985), pp. 1231–1236.

[69] Soner Sonmezoglu et al. "A Method and Analysis to Enable Efficient Piezoelectric Transducer-Based Ultrasonic Power and Data Links for Miniaturized Implantable Medical Devices". In: *IEEE Transactions on Ultrasonics, Ferroelectrics, and Frequency Control* 68.11 (Nov. 1, 2021). Publisher: Institute of Electrical and Electronics Engineers Inc., pp. 3362–3370.

[70] Olavi Siiman and Alexander Burshteyn. "Cell surface receptor-antibody association constants and enumeration of receptor sites for monoclonal antibodies". In: *Cytometry* 40.4 (2000), pp. 316–326.

[71] Shaleen Vira et al. "Fluorescent-labeled antibodies: Balancing functionality and degree of labeling". In: *Analytical Biochemistry* 402.2 (July 15, 2010), pp. 146–150.

[72] Inc. AAT Bioquest. *Extinction Coefficient [Cy5.5 (Cyanine-5.5)]*. 2024.

[73] Loïc Dupré et al. "T Lymphocyte Migration: An Action Movie Starring the Actin and Associated Actors". In: *Frontiers in Immunology* 6 (Nov. 18, 2015), p. 586.

[74] Mark J. Miller et al. "Autonomous T cell trafficking examined in vivo with intravital two-photon microscopy". In: *Proceedings of the National Academy of Sciences* 100.5 (Mar. 4, 2003). Publisher: Proceedings of the National Academy of Sciences, pp. 2604–2609.

[75] Simon Cen. "DC Bias Characteristics of Ceramic Capacitors". In: ().

[76] Asmaysinh Gharia et al. "Signal to Noise Ratio as a Cross-Platform Metric for Intraoperative Fluorescence Imaging". In: *Molecular Imaging* 19 (2020), p. 1536012120913693.

[77] Rajan Kadel et al. "Opportunities and Challenges for Error Correction Scheme for Wireless Body Area Network—A Survey". In: *Journal of Sensor and Actuator Networks* 8.1 (Dec. 23, 2018), p. 1.

[78] Caroline Robert. "A decade of immune-checkpoint inhibitors in cancer therapy". In: *Nature Communications* 11.1 (July 30, 2020). Number: 1 Publisher: Nature Publishing Group, p. 3801.

[79] Antoni Ribas and Jedd D. Wolchok. "Cancer immunotherapy using checkpoint blockade". In: *Science* 359.6382 (Mar. 23, 2018). Publisher: American Association for the Advancement of Science, pp. 1350–1355.

[80] Z. KNITTL. *Optics of Thin Films: An Optical Multilayer Theory*. Google-Books-ID: UXi3PwAACAAJ. Books on Demand, 1976. 548 pp.

[81] Vivek Boominathan et al. "Recent advances in lensless imaging". In: *Optica* 9.1 (Jan. 20, 2022). Publisher: Optica Publishing Group, pp. 1–16.

[82] Ulkuhan Guler and Maysam Ghovanloo. "Power Management in Wireless Power-Sipping Devices: A Survey". In: *IEEE Circuits and Systems Magazine* 17.4 (2017). Conference Name: IEEE Circuits and Systems Magazine, pp. 64–82.

[83] Hyogeun Shin et al. "Miniaturized multicolor fluorescence imaging system integrated with a PDMS light-guide plate for biomedical investigation". In: *npj Flexible Electronics* 7.1 (Feb. 9, 2023). Number: 1 Publisher: Nature Publishing Group, pp. 1–10.

[84] "Marketing Clearance of Diagnostic Ultrasound Systems and Transducers - Guidance for Industry and Food and Drug Administration Staff". In: ().

[85] Zeinab Kashani and Mehdi Kiani. "A Study on Ultrasonic Wireless Power Transfer With Phased Array for Biomedical Implants". In: *IEEE Transactions on Biomedical Circuits and Systems* 17.4 (2023), pp. 713–724.

[86] Hans Raskov et al. "Cytotoxic CD8+ T cells in cancer and cancer immunotherapy". In: *British Journal of Cancer* 124.2 (Jan. 2021). Publisher: Nature Publishing Group, pp. 359–367.

[87] Matthew H. Spitzer et al. "Systemic Immunity Is Required for Effective Cancer Immunotherapy". In: *Cell* 168.3 (Jan. 2017), 487–502.e15.

[88] Julien Faget et al. "Neutrophils in the era of immune checkpoint blockade". In: *Journal for ImmunoTherapy of Cancer* 9.7 (July 1, 2021). Publisher: BMJ Specialist Journals Section: Review, e002242.

[89] Julia Kargl et al. "Neutrophil content predicts lymphocyte depletion and anti-PD1 treatment failure in NSCLC". In: *JCI Insight* 4.24 (Dec. 19, 2019). Publisher: American Society for Clinical Investigation.

[90] Nam Woo Cho et al. "T cell-instructed inflammation drives immune checkpoint inhibitor therapy resistance. 1". In: ().

[91] Susan L. Troyan et al. "The FLARE™ Intraoperative Near-Infrared Fluorescence Imaging System: A First-in-Human Clinical Trial in Breast Cancer Sentinel Lymph Node Mapping". In: *Annals of surgical oncology* 16.10 (Oct. 2009), pp. 2943–2952.

[92] Rutger M. Schols, Niels J. Connell, and Laurents P. S. Stassen. "Near-infrared fluorescence imaging for real-time intraoperative anatomical guidance in minimally invasive surgery: a systematic review of the literature". In: *World Journal of Surgery* 39.5 (May 2015), pp. 1069–1079.

[93] E. de Boer et al. "Optical innovations in surgery". In: *The British Journal of Surgery* 102.2 (Jan. 2015), e56–72.

[94] Sreya Ghosh and Chrysanthe Preza. "Fluorescence microscopy point spread function model accounting for aberrations due to refractive index variability within a specimen". In: *Journal of Biomedical Optics* 20.7 (July 2015), p. 75003.

[95] Chenzhong Yin et al. "Network science characteristics of brain-derived neuronal cultures deciphered from quantitative phase imaging data". In: *Scientific Reports* 10.1 (Sept. 15, 2020). Publisher: Nature Publishing Group, p. 15078.

[96] Claire Lifan Chen et al. "Deep Learning in Label-free Cell Classification". In: *Scientific Reports* 6.1 (Mar. 15, 2016). Publisher: Nature Publishing Group, p. 21471.

[97] Hongda Wang et al. "Deep learning enables cross-modality super-resolution in fluorescence microscopy". In: *Nature Methods* 16.1 (Jan. 2019). Publisher: Nature Publishing Group, pp. 103–110.

[98] Kaiming He et al. "Deep Residual Learning for Image Recognition". In: *2016 IEEE Conference on Computer Vision and Pattern Recognition (CVPR)*. 2016 IEEE Conference on Computer Vision and Pattern Recognition (CVPR). Las Vegas, NV, USA: IEEE, June 2016, pp. 770–778.

[99] Rikiya Yamashita et al. "Convolutional neural networks: an overview and application in radiology". In: *Insights into Imaging* 9.4 (Aug. 2018). Number: 4 Publisher: SpringerOpen, pp. 611–629.

[100] Hossein Najafiaghdam et al. "3D Reconstruction of cellular images from microfabricated imagers using fully-adaptive deep neural networks". In: *Scientific Reports* 12.1 (May 4, 2022), p. 7229.

[101] Ken Perlin. "An image synthesizer". In: *ACM SIGGRAPH Computer Graphics* 19.3 (July 1985), pp. 287–296.

[102] Andrei Tatarinov. "Perlin noise in Real-time Computer Graphics". In: ().

[103] Fang Huang et al. "Ultra-High Resolution 3D Imaging of Whole Cells". In: *Cell* 166.4 (Aug. 11, 2016), pp. 1028–1040.

[104] W. T. Mason. *Fluorescent and luminescent probes for biological activity: a practical guide to technology for quantitative real-time analysis*. 2nd ed. Biological techniques. San Diego, Calif: Academic Press, 1999.

[105] Sri Rama Prasanna Pavani et al. "Three-dimensional, single-molecule fluorescence imaging beyond the diffraction limit by using a double-helix point spread function". In: *Proceedings of the National Academy of Sciences* 106.9 (Mar. 3, 2009). Publisher: Proceedings of the National Academy of Sciences, pp. 2995–2999.

[106] Xiaobai Ma, Zhenglin Geng, and Zhi Bie. "Depth Estimation from Single Image Using CNN-Residual Network". In: 2017.

[107] Yogesh K. Ramadass and Anantha P. Chandrakasan. "An Efficient Piezoelectric Energy Harvesting Interface Circuit Using a Bias-Flip Rectifier and Shared Inductor". In: *IEEE Journal of Solid-State Circuits* 45.1 (2010), pp. 189–204.

[108] Sijun Du and Ashwin A. Seshia. "An Inductorless Bias-Flip Rectifier for Piezoelectric Energy Harvesting". In: *IEEE Journal of Solid-State Circuits* 52.10 (2017), pp. 2746–2757.

[109] Seung-Hee Ahn, Joonsoo Jeong, and Sung June Kim. "Emerging Encapsulation Technologies for Long-Term Reliability of Microfabricated Implantable Devices". In: *Micromachines* 10.8 (Aug. 2019). Number: 8 Publisher: Multidisciplinary Digital Publishing Institute, p. 508.

[110] Seonho Seok. "Polymer-Based Biocompatible Packaging for Implantable Devices: Packaging Method, Materials, and Reliability Simulation". In: *Micromachines* 12.9 (Aug. 27, 2021), p. 1020.

[111] Jiaxin Yin et al. "What is the optimal duration of immune checkpoint inhibitors in malignant tumors?" In: *Frontiers in Immunology* 13 (Sept. 26, 2022), p. 983581.

[112] Eve McGlynn et al. "The Future of Neuroscience: Flexible and Wireless Implantable Neural Electronics". In: *Advanced Science* 8.10 (2021), p. 2002693.

[113] David K. Piech et al. "A wireless millimetre-scale implantable neural stimulator with ultrasonically powered bidirectional communication". In: *Nature Biomedical Engineering* 4.2 (Feb. 2020). Number: 2 Publisher: Nature Publishing Group, pp. 207–222.

[114] Jeong Hoan Park et al. "Feasibility of LCP as an Encapsulating Material for Photodiode-Based Retinal Implants". In: *IEEE Photonics Technology Letters* 28.9 (May 2016). Conference Name: IEEE Photonics Technology Letters, pp. 1018–1021.

[115] James A. Guggenheim et al. "The visible and near-infrared optical absorption coefficient spectrum of Parylene C measured by transmitting light through thin films in liquid filled cuvettes". In: *Optical Materials Express* 11.11 (Nov. 1, 2021). Publisher: Optica Publishing Group, pp. 3854–3869.

[116] Omid Veiseh et al. "Size- and shape-dependent foreign body immune response to materials implanted in rodents and non-human primates". In: *Nature Materials* 14.6 (June 2015). Number: 6 Publisher: Nature Publishing Group, pp. 643–651.

[117] Alejandro Carnicer-Lombarte et al. "Foreign Body Reaction to Implanted Biomaterials and Its Impact in Nerve Neuroprosthetics". In: *Frontiers in Bioengineering and Biotechnology* 9 (2021).